國立臺灣大學理學院地質科學研究所

碩士論文

Department of Geosciences

College of Science

National Taiwan University

Master's Thesis

大屯火山群年代的不確定性

Evaluating the Inconsistencies in Geochronometric Data of the Tatun Volcano Group

楊雅閔

Ya-Min Yang

指導教授：宋聖榮 博士

Advisor: Sheng-Rong Song, Ph.D

中華民國 114 年 7 月

July 2025

doi:10.6342/NTU202503882

中文摘要

過去已有許多研究嘗試利用各種定年方法與定年材料求得大屯火山群最近一次噴發的年代。然而，各研究結果互不相容，最後一次噴發年齡仍未有定論。大多數研究於 20 世紀末期進行，與近期相關研究則相隔逾二十年。隨著時間推移，定年設備與技術持續進步，且對不同定年方法之機制及所涉元素與礦物特性之理解更為深入，因而有機會重新評估前人定年結果，並與近期研究成果比較，以判定何種方法最適合用於大屯火山群最近噴發年代的測定。

本研究於磺嘴山、七星山、紗帽山、烘爐山及竹子山等岩流露頭及岩芯樣本上，分別進行鈾釷定年與氬氬定年分析，並將結果與前人之鉀氬、氬氬、鈾鉛鋯石、鈾釷鐳及核飛跡等定年結果進行比較。

重複樣本在鈾釷與氬氬定年分析中呈現顯著差異，推測主因為樣本組成複雜。鈾釷分析中識別出兩組具有顯著不同同位素組成與年齡之角閃石。各別井孔中的岩芯樣本基質的氬氬結果年齡相近，暗示岩流可能連續快速噴發；而氬氬角閃石年齡則較其基質年代為早。與先前資料比較，氬氬基質與鈾釷鐳定年所測年代通常為研究區中最年輕，且與同類研究結果相當吻合；核飛跡年代則始終屬於最老群，而鉀氬及氬氬全岩年代分佈廣泛。大屯火山群岩體年齡過於年輕，不適合鈾鉛鋯石分析，日後或需考慮採用鈾釷鋯石定年。整體而言，由於岩石組成複雜可能導致測得年代偏舊，實際噴發年齡很可能較目前測得結果年輕。

關鍵詞：大屯火山群、火成岩定年、近期噴發年代定年、氬氬定年、鈾釷定年

doi:10.6342/NTU202503882

Abstract

Multiple studies in the past have attempted to obtain the most recent eruption age of the Tatun Volcanic Group (TVG) using various dating methods and dating materials available. Yet results among studies are incomparable, and the age of the last eruption remains inconclusive. Most studies were conducted at the end of the 20th century, with a two-decade gap before those done in the 21st century. With the passing of time, better equipments and techniques have been developed, and with a better understanding of the mechanics of different dating methods and the characteristics of the elements and minerals involved, it is now possible to re-evaluate previous dating results and compare them with more recent results to determine which method is most suitable for dating recent eruption ages in TVG.

In this study, U-Th and Ar-Ar dating analyses were conducted on groundmass and mineral separates from Huangzuei, Cising, Shamao, Honlu, and Chutze lava flow outcrops and boreholes, then compared with past K-Ar, Ar-Ar, U-Pb zircon, U-Th-Ra, and fission track results.

Duplicate samples produced divergent ages for both U-Th and Ar-Ar analyses. This is attributed to the samples being multiphase. Two amphibole populations of vastly different isotopic compositions and ages were identified in the U-Th analysis. Within each borehole, the Ar-Ar groundmass results show similar ages, suggesting that the lava flows erupted in quick succession. Ar-Ar hornblende ages predate their groundmass counterparts. But compared to previous data, Ar-Ar and U-Th-Ra results typically rank among the youngest ages in an area and compare well with similar studies. Fission track ages are consistently among the oldest, while K-Ar and Ar-Ar whole rock ages span across a broad range. The TVG rocks were too young for U-Pb zircon analysis, and U-Th zircon analysis may be needed. All bulk analyses may appear older due to multiphase, therefore, eruption age is likely younger than measured results.

Keywords: Tatun Volcanic Group, geochronology of igneous rocks, recent eruption age dating, Ar-Ar dating, U-Th dating

doi:10.6342/NTU202503882

CONTENTS

doi:10.6342/NTU202503882

doi:10.6342/NTU202503882

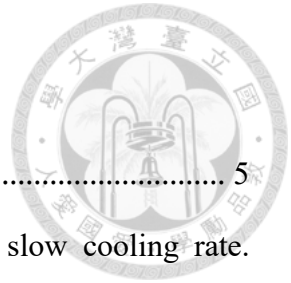

LIST OF FIGURES

doi:10.6342/NTU202503882

doi:10.6342/NTU202503882

doi:10.6342/NTU202503882

doi:10.6342/NTU202503882

doi:10.6342/NTU202503882

LIST OF TABLES

doi:10.6342/NTU202503882

doi:10.6342/NTU202503882

I. Introduction

The Tatun Volcano Group (TVG) defines the northern boundary of the Taipei Basin, which contains the Taipei metropolis—home to seven million people. With no documented eruptions, the TVG was long considered inactive until Song et al. (2000a) proposed that frequent volcanic seismicity and active hydrothermal systems could signal the presence of an underlying magma reservoir. Helium isotope data from fumaroles and hot springs point to a deep magmatic source, thus supporting this hypothesis (Yang et al., 1999). These findings raised public safety concerns for the city of Taipei and renewed interest in the TVG's volcanic history, especially the timing of its most recent eruption, since a Holocene eruption would classify the TVG as active (Szakacs, 1994).

Earlier studies of the TVG often assumed that radiometric dates on igneous rocks represented eruption ages, regardless of the dating method or material used. However, this assumption is not always valid. Many geochronological techniques yield either a weighted mean age of multiple grains, such as the bulk analysis method, or the sample material might not reflect the targeted event (eruption) and represent other magmatic events, such as magma reservoir processes. Therefore, additional evidence is needed to confirm that such dates can represent eruptive events.

Researchers have employed various dating methods to estimate eruption ages for

doi:10.6342/NTU202503882

TVG volcanoes, including fission track (Wang & Chen, 1990), K–Ar or Ar–Ar (Chang et al., 2024; Juang, 1993; Juang & Bellon, 1984; Juang & Chen, 1989; Lee, 1996; Song et al., 2011; Tsao, 1994), and U-series (Chu et al., 2018; Zellmer et al., 2015), and C–14 (Belousov et al., 2010). Yet, the results frequently contradict one another. For example, depending on the study, the age of the Shamao dome can range from 1,370 ya to 300 ka, even though sampling sites are within close proximity of each other (Tsao, 1994; Lee, 1996; Zellmer et al., 2015; Chu et al., 2018).

This study provides new U–Th internal isochron data and Ar–Ar groundmass and amphibole data. These two methods allow for individual measurements of groundmass and mineral separates, which may provide clues about the cause of age discrepancies. Groundmass is representative of erupted magma, whereas mineral grains may have existed prior to eruption. The new data are compared with previous TVG age data, and the previous data can then be reinterpreted. This research aims to determine which methods are best suited for establishing recent eruption ages in the TVG region, and constrain those ages.

II. Geological Background

Magmatism in the TVG has long been attributed to the westward propagation of the Ryukyu Arc, where the Philippine Sea Plate subducts beneath the Eurasian Plate (Chen, 1990; Chung et al., 1995; Juang, 1993; Teng, 1996). Other studies propose that late

doi:10.6342/NTU202503882

Pliocene lithospheric extension, triggered by orogenic collapse in northern Taiwan, drives this magmatism instead (Chung et al., 2001; Wang et al., 1999; 2004). The TVG overlies Miocene sandstones, which frequently appear as xenoliths in erupted lavas. Three major NE-striking faults traverse the area: the Chinshan and Kanchiao reverse faults, remnants of a Plio-Pleistocene collision orogeny, and the Shanchiao normal fault, a product of the present extensional regime (Chu et al., 1998; Song et al., 2007).

TVG volcanoes are composite volcanoes distributed along SW–NE and E–W volcanic ridges. Geomorphic and petrological traits define six subgroups: Kuanyin (觀音山), Tatun (大屯山), Chutze (竹子山), Cising (七星山), Huangzuei (磺嘴山), and Tinghuohsiu (丁火朽山) (Song et al., 2011). Volcanoes on the SW–NE ridge (e.g., Tatun, Chutze) feature sharp crests and steep slopes carved by subtropical rainfall. In contrast, the E–W ridge volcanoes (e.g., Cising, Shamao (紗帽山), Huangzuei, Honlu (烘爐山)) retain their primary crater-and-cone morphology and distinct lava flows, indicating younger formation than those on the SW–NE ridge (Liu et al., 2007; Yang et al., 2004). Volcanic deposits occur mainly as lava flows, the dominance of lava flows implies predominantly extrusive volcanism (Belousov et al., 2010; Chen & Wu, 1971; Song et al., 2000b).

TVG volcanoes predominantly consist of andesite, basaltic andesite, and, in some rare cases, basalt (Chen & Wu, 1971; Song et al., 2000b; Wang, 2004). All rocks exhibit

doi:10.6342/NTU202503882

porphyritic textures, with plagioclase, amphibole, pyroxene, and titaniferous magnetite phenocrysts; basalts also contain olivine (Chen, 1975; 1978; 1990). Groundmass and phenocrysts occupy nearly equal volumes. Plagioclase microlites occur abundantly in the groundmass. Almost all andesite plagioclase phenocrysts display oscillatory or simple zoning, normal and reverse (Figure 1e and 1f). In andesites, brown oxyhornblendes (basaltic hornblendes) often bear opacite rims (Figure 1a and 1g) formed by reheating common hornblende (Huang, 1954). Amphibole-rich nodules, known as cognate inclusions, occur in TVG rocks, especially at Shamao (Chen, 1978). These cumulates formed at the base of a magma reservoir during basaltic magma fractionation. In Shamao, the nodules lie within a chilled zone of host andesite, indicating hotter carrier magma. Unlike their host rock, these nodules lack significant zoning. Amphiboles enclose plagioclase and pyroxene poikilocrysts, and some developed opacite rims. Magnetites within these rims appear euhedral and exhibit ilmenite–hematite exsolution, signaling oxidation (Buddington and Lindsley, 1964).

doi:10.6342/NTU202503882

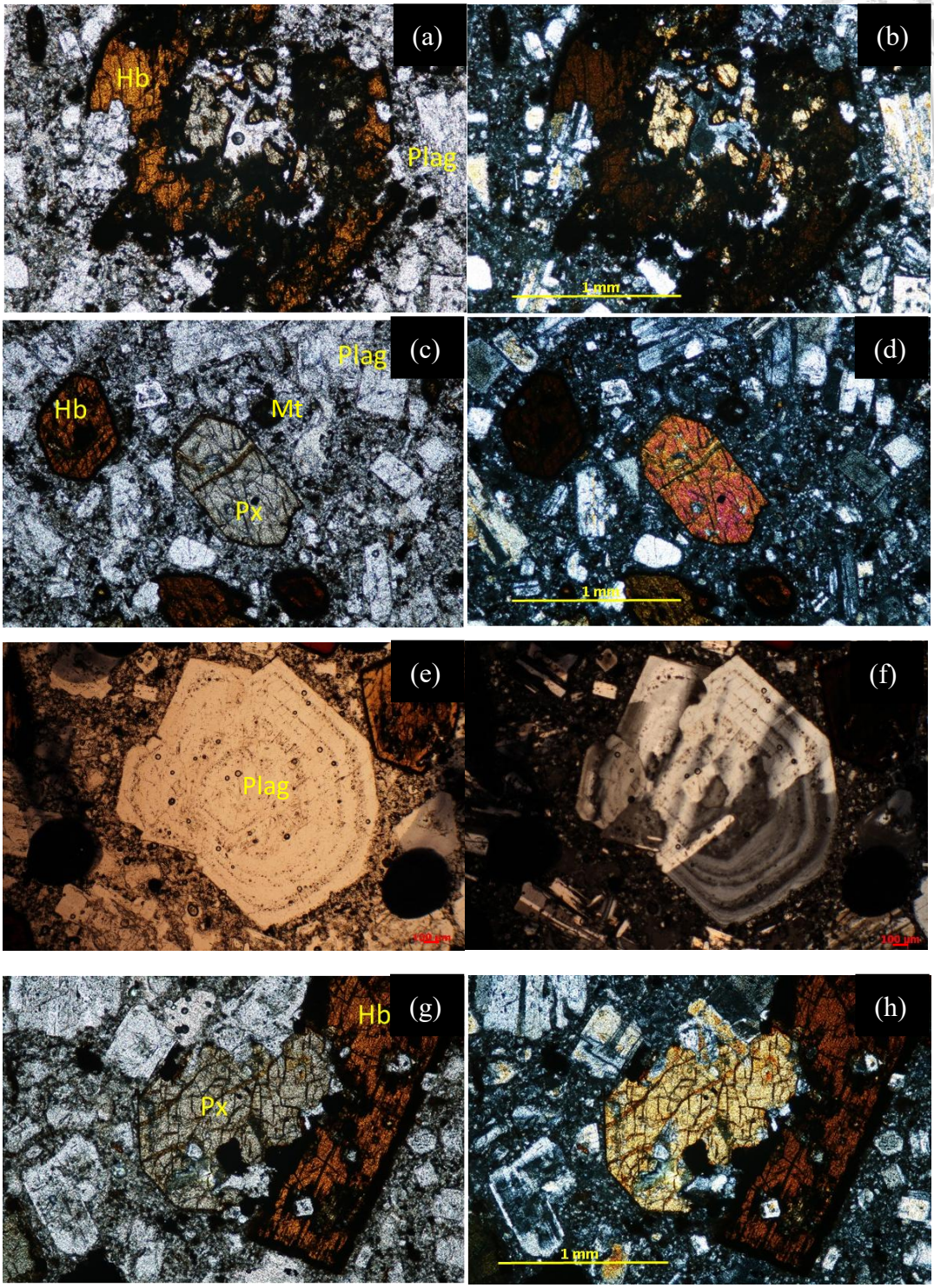

Figure 1: Petrographical images of analyzed samples from Shamao.
(a)(c)(e) plane-polarized light (PPL) and (b)(d)(f) cross-polarized light (XPL) images of sample Shamao 2. Note the two different sizes and occurrences of hornblendes. (g) PPL and (h) XPL images of sample Shamao 3. Px, pyroxene; Hb, hornblende; Mt, magnetite; Plag, plagioclase.

doi:10.6342/NTU202503882

Andesites classify into eight types based on mafic mineral assemblages: two-pyroxene andesite; olivine-bearing hornblende two-pyroxene andesite; hornblende two-pyroxene andesite; hornblende-bearing two-pyroxene andesite; two-pyroxene hornblende andesite; hypersthene hornblende andesite; augite hornblende andesite; and hornblende andesite (Chen & Wu, 1971; Huang & Liu, 1988). The SW–NE ridge consists mainly of two-pyroxene andesites with minimal hornblende, whereas the E–W ridge hosts abundant hornblende-rich andesites.

III. Previous Studies

As noted above, previous studies have applied various dating methods to TVG volcanoes and obtained conflicting results. These studies will be briefly summarized in this section and be used for age comparison in the Discussion section. In most studies, igneous samples came from lava flows; only Wang & Chen (1990) analyzed pyroclasts. This study will only make age comparisons with lava flow data since pyroclast age data is scarce.

A. K–Ar and Ar–Ar Age Reports

K–Ar dating has been favored in the TVG region because the equipment was widely available and sample processing required fewer steps.

Juang et al. (Juang and Bellon, 1984; Juang and Chen, 1989; Juang, 1993) dated whole-rock and amphibole separates from lava flows. Their ages range from 0.37 to 2.46

doi:10.6342/NTU202503882

Ma and cluster into three magmatic episodes at ~2.5, ~0.75, and ~0.5 Ma. They inferred a volcanic sequence: lower Cising lavas → Chutze subgroup → Huangzuei subgroup → upper Cising lavas.

Tsao (1994) conducted K–Ar analysis on TVG whole-rock samples and compared their findings with previous studies. Their ages proved slightly younger but carried large uncertainties from excess atmospheric argon in young samples.

Lee (1996) conducted Ar–Ar analysis on ten Cising flows and seven others, reporting plateau ages for 14 flows and total-gas ages for three samples between 0.22 and 1.5 Ma. Several samples showed excess argon.

Song et al. (2011) conducted Ar–Ar analysis on whole-rock samples from four Huangzuei and six Chutze flows; their ages span modern to 120 ka (Huangzuei) and modern to 130 ka (Chutze), with very large uncertainties that are sometimes twice the age.

Chang et al. (2024) conducted Ar–Ar analysis on groundmass from three flows: one each from Cising (0.081 ± 0.005 Ma), Tatun (0.28 ± 0.02 Ma), and Honlu (0.159 ± 0.017 Ma). Cising and Tatun results reported slight $^{40}Ar/^{36}Ar$ deviations from atmospheric values.

Amongst K–Ar and Ar–Ar TVG data, whole rock ages span across a broad range

doi:10.6342/NTU202503882

while groundmass ages are often the youngest.

B. U–Pb Zircon Age Report

Chu et al. (2018) conducted LA-ICP-MS and SIMS U–Pb analysis (with intial ^{230}Th disequilibrium correction) on TVG zircons. Most ages cluster at ~0.3 Ma. Four of the 20 yielded ages greater than 0.3 Ma and could be corrected with the results of a SIMS analysis for ^{230}Th disequilibrium. Inherited zircons were found in abundance in the TVG volcanoes, and detrital zircon ages indicate sources from Eocene-Oligocene strata. Combining inherited and magmatic populations, five magmatic episodes at ≤0.3, 0.35–0.8, 1.0–1.5, 2.0–2.5, and ~3 Ma were defined. Many samples can only be constrained to ≤0.3 Ma, ages younger than that would be in U–Th disequilibrium and would require ^{230}Th analyses.

C. U–Th–Ra Age Report

Zellmer et al. (2015) attempted internal U–Th isochrons and Ra–Th dating on young volcanoes (Cising, Shamao, and Huangzuei). Although multi-phase isochrons proved poorly defined, two-point isochrons. Magnetite displayed the largest amount of U–Th disequilibrium, meaning it's the farthest from returning to equilibrium, thus may represent erupted magma, and is used to pair with other minerals and for two-point isochron ages.

Cising did not yield any isochrons of meaningful age.

Shamao: U–Th pyroxene–whole-rock–magnetite at 33.2 ± 1.3 ka, amphibole–

doi:10.6342/NTU202503882

magnetite at 28.3 ± 1.5 ka, plagioclase–magnetite at 18.0 ± 1.3 ka; and a Ra–Th magnetite age of 1,367 ± 11 yr.

Huangzuei: U–Th plagioclase–groundmass at 72 ± 4 ka and magnetite–groundmass at 148 ± 10 ka.

These represent the youngest TVG ages to date but require verification via reproduction; messy isochrons reflect inherited or recycled crystals. Mineral–mineral pair ages represent crystallization ages for each mineral paired with magnetite if the crystals are related to the melt. U–Th ages of the same crystals are older than Th–Ra age, indicating at least two stages of crystal growth.

D. Fission Track Age Report

Wang & Chen (1990) performed fission-track analyses using the external detector method on lavas and pyroclasts, obtaining 25 apatite and 15 zircon ages that group into two episodes at 0.25–0.8 Ma and 0.25–0.28 Ma. These represent the oldest ages in each locality, likely because crystals retained tracks formed before eruption.

E. C–14 Age Reports

Belousov et al. (2010) dated volcaniclastic deposits along Mt. Shamao creeks at 23–13 ka and a Mt. Cising debris avalanche at ~6 ka. Because it is suspected that these are remobilized deposits (Hong et al., 2025), this study excludes ^{14}C ages from age comparison.

doi:10.6342/NTU202503882

IV. Overview of Igneous Rock Dating Methods Applied to the TVG Region

A. K–Ar and Ar–Ar Analysis

K can be found in abundance in many rocks, giving K–Ar a broad range of application. Two aspects make the K–Ar system unique: it is a branched decay system where ^{40}K decays to either ^{40}Ca or ^{40}Ar, and the parent and daughter isotopes are of different phases; ^{40}K is a solid while ^{40}Ar is a noble gas. As a noble gas, Ar ends up being trapped in crystal lattices instead of chemically binding to them. When temperatures are high enough, argon gas readily diffuses out of the erupting magma, so that after the lava cools, there is very little Ar left behind, and the K–Ar clock is then reset. Meaning, other than atmospheric Ar that is absorbed into the rock while the lava is still cooling and crystals are still forming, non-radiogenic Ar should ideally be non-existent. However, diffusion rate is exponentially related to temperature (Harrison et al., 1985), and if the rock and its minerals were not exposed to high enough temperatures for a long enough time, the K–Ar clock will only be partially reset. Diffusion rate increases with temperature and cooling rate, and, as a result, closure temperature, the temperature where radiogenic Ar loss and creation are of equal rate, is also dependent on cooling rate, meaning closure temperature increases with cooling rate (Dodson, 1973) (Figure 2). If it is suspected that the initial Ar value differs from atmospheric values, using measurements from Ar–Ar analysis, an inverse isochron plotting $^{36}Ar/^{40}Ar$ against $^{39}Ar/^{40}Ar$ solves for both age and

doi:10.6342/NTU202503882

initial $^{40}Ar/^{36}Ar$.

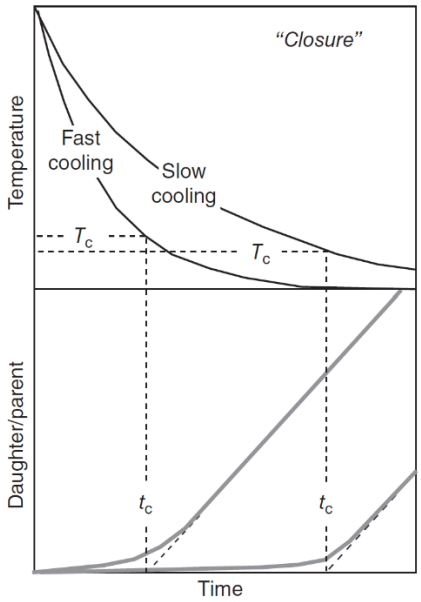

Figure 2: Conceptual graph of closure temperatures for fast and slow cooling rate. Cooling leads to decreasing daughter loss, and that leads to partial daughter retention (curve portion of line), and eventually ends with complete daughter retention (linear portion of line). Fast cooling corresponds to a higher closure temperature and an earlier closure time. T_c, closure temperature; t_c closure time. (Reiners et al. (2017))

In Ar–Ar analysis, instead of splitting a sample and measuring $^{40}K_{(solid)}$ and $^{40}Ar_{(gas)}$ separately, this method measures both $^{40}Ar_{(gas)}$ and $^{39}Ar_{(gas)}$ simultaneously, reducing the effects of sample heterogeneity on the measurements. ^{39}Ar does not occur naturally and has a half-life of 269 years. By irradiating a sample, ^{39}K is turned into ^{39}Ar, which can then be used to calculate ^{40}K since $^{40}K/^{39}K$ is assumed to be constant at any time. Combined with step-heating, components that are less retentive of their gas can be differentiated from those that are more retentive by increasing the temperature by increments.

In most K–Ar or Ar–Ar analyses on TVG igneous rocks, analytes were mostly whole

doi:10.6342/NTU202503882

rocks. This may be a major factor as to why attempts at duplicating those results are rarely successful, since mineral grains could have different origins. Due to the daughter isotope ^{40}Ar being a gas, assuming all argon trapped within the magma escapes during an eruption, the K–Ar system should be reset once the lava cools. Thus, the K–Ar and Ar–Ar dating methods are capable of providing cooling ages, making them ideal when it comes to dating eruption ages in volcanic rocks. Secondary processes can reopen the system, so selecting un-weathered mineral separates or groundmass with sufficient amount of potassium optimizes eruption-age determinations.

B. U–Pb Zircon Analysis

Both U and Th are incompatible elements and typically have a valence of +4. But under oxidizing conditions, U has a valence of +6, and may form UO_4^{2-}, which is soluble. U and Th are concentrated in accessory minerals such as zircon and monazite. Zircon, in particular, concentrates U and excludes Pb, resulting in high U/Pb ratios. It is also resistant to mechanical and chemical weathering, meaning it is likely to maintain a closed system.

The U–Th–Pb system involves three decay chains: ^{235}U–^{207}Pb, ^{238}U–^{206}Pb, and ^{232}Th–^{208}Pb (Figure 3). Intermediate daughter half-lives are much shorter and can be assumed to be in secular equilibrium, where the daughter's production and decay rates are in equilibrium, allowing for simplification of parent–daughter age equations to

doi:10.6342/NTU202503882

include only parent and final stable daughter:

$$\left(\frac{^{206}Pb}{^{204}Pb}\right) + \left(\frac{^{206}Pb}{^{204}Pb}\right)_0 = \left(\frac{^{238}U}{^{204}Pb}\right)\left(e^{\lambda 238t} - 1\right) \quad (1)$$

$$\left(\frac{^{207}Pb}{^{204}Pb}\right) + \left(\frac{^{207}Pb}{^{204}Pb}\right)_0 = \left(\frac{^{235}U}{^{204}Pb}\right)\left(e^{\lambda 235t} - 1\right) \quad (2)$$

$$\left(\frac{^{208}Pb}{^{204}Pb}\right) + \left(\frac{^{208}Pb}{^{204}Pb}\right)_0 = \left(\frac{^{232}Th}{^{204}Pb}\right)\left(e^{\lambda 232t} - 1\right) \quad (3)$$

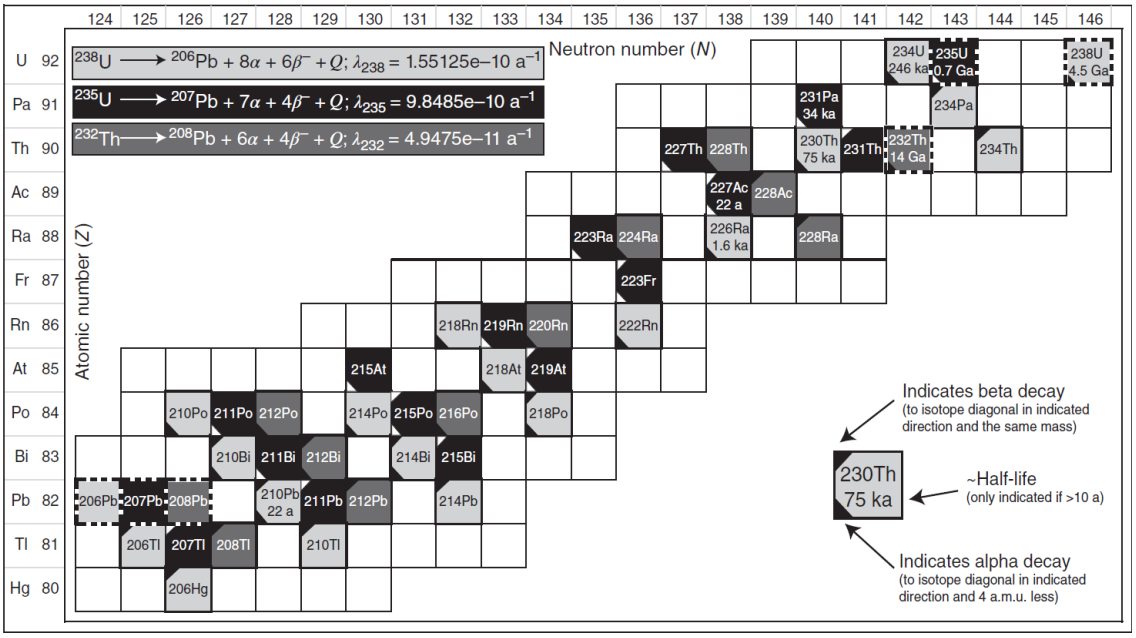

Figure 3: U–Th–Pb decay chain. Q, energy released during decay. (Reiners et al. (2017))

An additional Pb–Pb method assumes $^{238}U/^{235}U$ is constant in nature, permitting the division of the first two equations:

$$\left(\frac{^{235}U}{^{238}U}\right) * \frac{e^{\lambda 235t} - 1}{e^{\lambda 238t} - 1} = \left(\frac{^{207}Pb}{^{206}Pb}\right)^* \quad (4)$$

$(^{207}Pb/^{206}Pb)^*$ is the radiogenic isotope ratios. Equations 1~4 assume that the reservoir from which a mineral crystallizes from is in secular equilibrium and that there is no elemental fractionation of intermediate daughters during crystallization. Preferential partitioning of a daughter will result in excess radiogenic age and an overestimated age.

doi:10.6342/NTU202503882

If the daughter is preferentially excluded, the result will be an underestimated age. Conveniently, only intermediate daughters with long enough half-lives will have a noticeable effect on the resulting age, such as ^{230}Th and ^{234}U from the ^{238}U chain, and ^{231}Pa from the ^{235}U chain. In high temperatures, ^{234}U will not be significantly fractionated from ^{238}U. Initial ^{230}Th disequilibrium can be corrected using the equation 5 (McLean et al., 2011), by assuming a value for f using available partitioning data or using estimates for $Th/U_{mineral}$ and Th/U_{melt}. $Th/U_{mineral}$ can be measured and Th/U_{melt} can be estimated using Th/U of the rock the mineral came from.

$$t_{excess} = (\frac{1}{\lambda 238}) \ln[\, 1 + (f - 1)(\ \frac{\lambda 238}{\lambda 230})] \ , \ f = [\frac{(Th/U)mineral}{(Th/U)liquid}] \qquad (5)$$

U–Pb zircon analysis is one of the most well-developed age dating methods in geology. It's also a single crystal analysis method, making it capable of identifying individual crystal populations. However, it does have its limitations. As an accessory mineral, zircon growth is not guaranteed during each and every thermal event. Zircon formation is mainly dependent on temperature and melt composition, particularly Zr concentration (Boehnke et al., 2013; Gervasoni et al., 2016; Watson & Harrison, 1983), and crystallization conditions are much harder to meet in less felsic magmas (e.g., Dickinson and Hess, 1982; Borisov and Aranovich, 2019; Shao et al., 2019; Bea et al., 2022). TVG lavas range from andesitic to basaltic, and thus cannot reliably produce a sufficient amount of magmatic zircon crystals. Furthermore, there is no guarantee that

doi:10.6342/NTU202503882

zircon saturation can be achieved to induce zircon precipitation during each and every eruption event in this area. Zircons extracted from these lavas could also be inherited from a completely different thermal event that precedented the eruption.

C. U–Th–Ra Analysis

The U–Th–Ra dating method uses a combination of the U–Th and Ra–Th systems. The ^{238}U–^{230}Th system is suitable for dating materials between 10,000 and 350,000 years old, while the ^{226}Ra–^{230}Th system is appropriate for materials aged between 100 and 8,000 years.

Uranium, thorium, radium, and barium are distributed throughout magma. When minerals begin to crystallize, each mineral incorporates different amounts of U, Th, Ra, and Ba, resulting in disequilibrium among these elements. As time passes, daughter isotope concentrations increase in proportion to how much parent isotope concentrations decrease, while simultaneously decaying. With enough time, the system will return to secular equilibrium.

By analyzing the isotopic concentrations of U and Th in the groundmass and various minerals in a rock sample, and using ^{232}Th (an isotope of thorium with a very long half-life of billions of years) for normalization, one can construct isochron diagrams with ^{238}U and ^{230}Th. This is an internal isochron dating method. Using the equation 6, the slope of the line between the groundmass and minerals gives the age of disequilibrium without

doi:10.6342/NTU202503882

requiring knowledge of the initial elemental concentrations. This line is the isochron. The initial ($^{230}Th/^{232}Th$) and ($^{238}U/^{232}Th$) is given by the intersection of the isochron with the equiline (where $^{230}Th/^{238}U = 1$), called an equipoint. A similar isochron can be constructed for ^{230}Th and ^{226}Ra. Because there are no stable radium isotopes, barium, which is chemically similar to radium, is used for normalization, instead (cf. Rubin & Zellmer, 2009).

$$(\frac{^{230}Th}{^{232}Th}) = (\frac{^{230}Th}{^{232}Th})_0 e^{-\lambda 230 t} + (\frac{^{238}U}{^{232}Th})(1 - e^{-\lambda 230 t}), \text{ slope} = 1 - e^{-\lambda 230 t} \quad (6)$$

^{226}Ra incorporation into magnetite is extremely limited (Blundy & Wood, 2003). Thus, any ^{226}Ra detected in magnetite is considered to result from the decay of ^{230}Th (Rubin & Zellmer, 2009). Accordingly, ^{226}Ra in magnetite can be assumed to have an initial value of zero, allowing for ^{226}Ra ingrowth age calculations:

$$t = \frac{\ln(1-(^{226}Ra/^{230}Th))}{-\lambda 226} \quad (7)$$

If the groundmass and minerals plot along an isochron, a crystallization age can be determined, and the mineral can be confirmed to have crystallized from the same magma. If not, the minerals are likely unrelated to the magma. In such cases, an isochron among the mineral–mineral or groundmass–mineral pairs may still yield an age. This age may represent a mix of old and new crystals. To further constrain the age of newly formed minerals, the Ra–Th system, a more suitable system for younger timescales, can be employed. Older crystals would have reached Ra–Th equilibrium, whereas younger

doi:10.6342/NTU202503882

crystals may still be out of equilibrium, allowing for age determination for events of different timelines using a single analyte.

In summary, the U–Th–Ra dating method has the benefit of being capable of analyzing various types of minerals separately, providing crystallization ages for each mineral group and giving some insight to the crystallization sequence of the magma. By incorporating two isotope systems, U–Th and Ra–Th, magmatic events that crystallized older or inherited crystals between 10 and 35 ka, and Holocene magmatic events that formed newer crystals between 100 to 8,000 years ago can both be dated using the same analyte. Unfortunately, this method is time-consuming and not readily accessible. It is also a bulk analysis method and represent weighted-mean averages of all mineral grains (Turner et al., 2003). Consequently, it is not completely exempt from the influence of xenocrysts, antecrysts, or xenoliths and requires fresh and unaltered rock samples.

D. Fission Track Analysis

Unlike the previous methods, fission track analysis is a radiation-damage method. Spontaneous fission of ^{238}U can release up to 100 times more energy than alpha decay. This energy is split between two nuclei that recoil from each other, creating a large linear damage zone called a fission track. Fission tracks appear as amorphous, sometimes porous, channels in a crystal that are metastable and will fade with time. They are a daughter of ^{238}U by spontaneous fission, and like other radioisotopic systems, a measured

doi:10.6342/NTU202503882

ratio of the tracks and ^{238}U can be used for geochronology. An abundance of tracks are needed to permit statistically reliable ages. This requires analytes with sufficient amount of U concentration, such as zircon and apatite. Although, the high U concentration in zircon may cause complications for dating older samples due to track densities too high to count. Fission track methods fall into two categories: grain population method, where tracks and U concentrations are measured on separate grains, and grain-by-grain method, where they're measured on the same grain. In the latter, two methods are commonly used to measure U concentrations: the external detector method and laser-ablation inductively couple plasma mass spectrometry (LA-ICP-MS). All methods require increasing size and contrast of latent fission tracks with the surrounding crystal via chemical etching, followed by a means of counting the tracks.

The population method involves measuring tracks in one aliquot by polishing and etching the tracks on the surface of a crystal then counting them. Under the assumption that U concentrations are identical, U is then measured in a separate aliquot by subjecting the sample to high temperatures for a sufficient amount of time to anneal all tracks. The aliquot is then irradiated to induce fission of ^{235}U. These induced fission tracks can then be counted just like the natural ones. U concentration can then be counted from the known natural $^{238}U/^{235}U$ ratio. The external detector method can measure track densities and U concentrations in a much smaller length scale. Like the population method, the crystal is

doi:10.6342/NTU202503882

polished and etched to reveal tracks. An external detector is then attached to the polished surface and irradiated. Induced fission tracks are then registered in the external detector by fission particles recoiling from the grain into the detector. The grain and detector are then separated, spontaneous tracks are counted in the sample, and induced tracks are counted in the detector. The ratio of the two is then used to calculate age. LA-ICP-MS has gained popularity in recent years as it does not require irradiation of the sample.

In theory, fission track dating is a great method for dating eruption age, since, ideally, the fission tracks in zircons and apatites are erased upon contact with high enough temperatures, and will only begin to form again once the magma has reached the surface and cooled. However, high cooling rates combined a short duration of heating lead to higher closure temperatures (Wagner, 1972, 1979). Zircon closure temperature of can range from 450°C within 10^4–10^6 minutes to 200°C within 10^6–10^9 years (Haack, 1977; Sharma et al., 1980). Speedy transportation from high temperatures to low temperatures, combined with a high cooling rate may not provide enough time for zircons and apatites to fully anneal upon eruption and lead to overestimated ages as explained in Wang and Chen (1990).

V. Methods

In the previous section, how each dating method and sample material might introduce age discrepancies was evaluated, and this study chose U–Th–Ra internal

doi:10.6342/NTU202503882

isochron analysis on groundmass, plagioclase, amphibole, pyroxene, and magnetite and Ar–Ar incremental-heating analysis on groundmass and amphiboles to analyze recent TVG lava flows.

U–Th–Ra analysis of the Shamao dome was to be conducted as a means to verify the validity of the results in Zellmer et al. (2015) by attempting to reproduce their Shamao ages, especially the Ra–Th magnetite age of 1,370 ya, the youngest age to ever be dated in the TVG region. However, Ra measurements were never completed, thus, only U–Th analysis was conducted. Ra sample preparation and planned analysis method will still be depicted in this section.

As a gas, the ^{40}Ar daughter isotope diffuses out of magma at high temperatures, the K–Ar system resets upon eruption and closes as lava cools. Provided no post-eruption alteration occurred, Ar–Ar groundmass analysis should yield eruption time. Crystals may retain Ar and are used to gauge mineral crystallization ages. Incremental heating can provide insight into the thermal history of a sample by separating components of varying Ar retentivity into different steps (Belluso et al., 2000). Additionally, applying the isochron technique to the results of stepped heating eliminates the need to assume initial atmospheric argon and reduces the impact of excess argon in samples.

doi:10.6342/NTU202503882

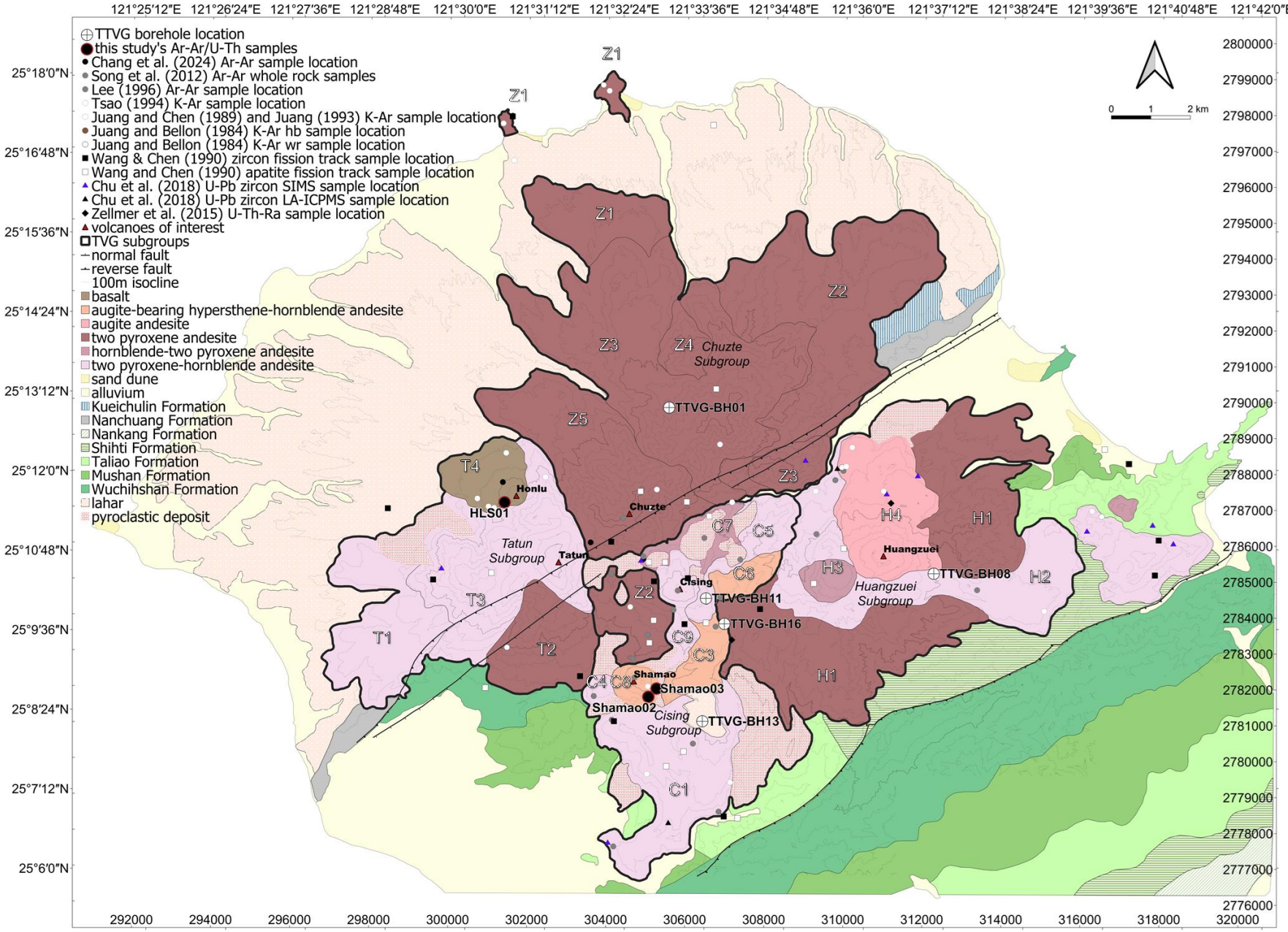

doi:10.6342/NTU202503882

Figure 4: Map of volcanic sequence proposed by Song et. al（2012）and sampling sites from this study.

Table 1: U–Th and Ar–Ar sample list and coordinates.

Sample Type	Subgroup	Borehole	Location	U–Th	Ar–Ar
Outcrop	Cising (Shamao)		121°32’46”E, 25°08’35”N	Shamao 2 (A & B)	Shamao 2-A
			121°32’53”E, 25°08’43”N	Shamao 3 (A & B)	Shamao 3-B
	Tatun (Honlu)		121°30’36”E, 25°11’31”N		HLS01
Core	Cising	TTVG-BH11	121°33’38”E, 25°10’04”N		TTVG-BH11-2931
					TTVG-BH11-5759
					TTVG-BH11-8183
		TTVG-BH13	121°33’35”E, 25°08’13”N		TTVG-BH13-3537
					TTVG-BH13-7880
		TTVG-BH16	121°33’54”E, 25°9’41”N		TTVG-BH16-138139
					TTVG-BH16-185186
	Chutze	TTVG-BH01	121°33’05”E, 25°12’57”N		TTVG-BH01-7071
					TTVG-BH01-9697
	Huangzuei	TTVG-BH08	121°37’04”E, 25°10’26”N		TTVG-BH08-1820
					TTVG-BH08-5355
					TTVG-BH08-8284

A. U–Th–Ra Analysis

Two whole rock samples were collected from Shamao: Shamao 2 and Shamao 3 (Figure 4). The samples are then split into two aliquots, A and B, to act as duplicates, making a total of four samples (e.g., Shamao 2A, Shamao 2B, Shamao 3A, and Shamao

doi:10.6342/NTU202503882

3B). U–Th–Ra analysis were carried out at the University of Hawaii at Manoa, USA.

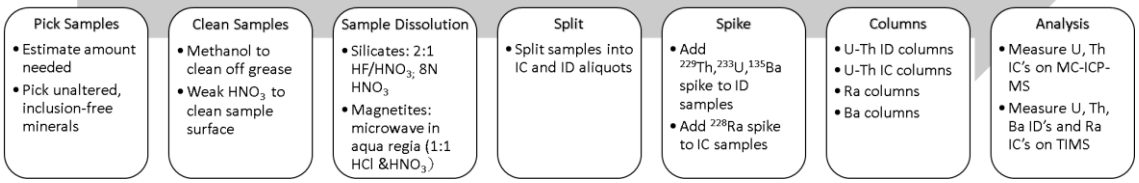

Figure 5: U–Th–Ra analysis flowchart.

Sample Preparation

Whole rocks are crushed then sieved. Particle sizes between 140 μm and 2 mm are handpicked under an optical microscope and grains with minimal crystals are selected as groundmass samples. Powder size particles should be avoided as they can become electrostatically attracted to the container. Particles too large in size should also be avoided, as they require longer digestion times. Plagioclase, amphibole, pyroxene, and magnetite samples were extracted from rock samples that were checked for alterations and put through mineral separation via magnetic separation and heavy liquid methods. After the mineral separation process, two distinctly different populations of amphibole crystals were observed from outcrop: one appearing fresher, and the other reddish, dull and strongly altered. Here it was decided instead of duplicate amphibole samples, A and B, altered and unaltered amphibole samples would be analyzed separately instead. The unaltered crystals were less abundant; hence, the same types of crystals were combined

doi:10.6342/NTU202503882

from duplicate A and B samples and were subsequently processed as two separate amphibole samples, I (unaltered crystals) and II (altered crystals), making a total of four amphibole samples (Shamao 2-I, Shamao 2-II, Shamao 3-I, Shamao 3-II). Magnetite analysis were also not duplicated due to insufficient amount of resources to process the samples.

Sample Cleaning and Leaching

All wet chemical procedures were conducted in a clean room with ultra-pure reagents prepared in-house at the University of Hawaii at Manoa. Hydrochloric acid and nitric acid were quartz-distilled, while hydrofluoric acid was purified with a two-bottle Teflon still.

Methanol was added to the sample to remove any oil residues. After ultrasonicating for 5 minutes, the methanol was pipetted out, and the samples were rinsed twice with ultrapure water. The samples were then subjected to a leaching step by adding 0.05–0.1 N nitric acid and left in an ultrasonic bath for 5 minutes. Then the acid was immediately pipetted out and ultrapure water was added to prevent further digestion. The leaching step was repeated once more, followed by rinsing twice in ultrapure water to remove residual acid. The sample was then left to dry under an infrared light in a fume hood. Magnetite grains retained some surface oxidation, which was removed using dilute hydrochloric acid prior to weighing and dissolution, followed by ultrasonic agitation until the rinse

doi:10.6342/NTU202503882

water ran clear.

Sample Dissolution

A 2:1 mixture of HF/HNO_3 was added to groundmass, plagioclase, amphibole, and pyroxene samples for dissolution. The samples were then sealed and heated under an infrared light until fully dissolved. Once fully dissolved, the samples were uncapped and left under an infrared light to dry. After they were dried, 8N nitric acid was added to begin the conversion to a nitric acid solution.

Magnetite samples were dissolved by means of microwave digestion. Aqua regia made from a 1:1 ratio of nitric acid and hydrochloric acid was added to magnetite samples inside a Teflon bomb. The bomb was then tightly sealed and microwaved for 30 seconds. After 30 seconds, the bomb was transferred to a sonic bath for 1 minute too cool. The microwave digestion process was repeated until the samples were fully dissolved.

After the samples were completely dissolved, the samples were dried, and the nitric acid conversion step was repeated twice more to remove any remaining hydrofluoric acid. 0.2 milliliters of 8N nitric acid was once again added to the sample, and the samples were sealed and heated under an infrared light until there was no residue left. The solution was then transferred into a centrifuge tube and centrifuged at maximum speed for six minutes. If there was no residue left after centrifugation, then we'd proceed to the next step. If there was undissolved material, the samples were returned to their original beaker and the

doi:10.6342/NTU202503882

dissolution steps were repeated. This step was repeated until the solution was fully transparent.

Split

The samples were then divided into two aliquots: an ID (isotope dilution) sample for determining isotope concentrations and IC (isotope composition) sample for measuring isotope ratios.

Spike

In ID samples, isotopes ^{229}U and ^{233}Th were added as a standard for naturally occurring U and Th. ^{135}Ba was added as a standard for Ra. For IC samples, ^{228}Ra was added.

Dry sample mass in the ID and IC bottles were calculated based on the weight proportions of solution distributed between the two. The following equations were used:

$$\text{ID sample dry mass} = \frac{\text{ID solution mass}}{\text{ID solution mass} + \text{IC solution mass}} \times \text{initial dry sample mass}$$

$$\text{IC sample dry mass} = \frac{\text{IC solution mass}}{\text{ID solution mass} + \text{IC solution mass}} \times \text{initial dry sample mass}$$

Spike amount was calculated by putting measured concentrations from Zellmer (2015) into the equations below:

$^{135}Ba\ (g) = Ba\ (\mu g/g) \times \text{sample mass}\ (g)$

$^{229}Th\ (g) = 0.08 \times [(Th\ (ng/g) \times \text{sample mass}\ (g)) / 7]$

$^{233}U\ (g) = 0.3 \times [(U\ (ng/g) \times \text{sample mass}\ (g)) / 10.4]$

doi:10.6342/NTU202503882

For ^{228}Ra spike in IC samples, the following condition was to be met after decay correction (due to its short half-life):

$$2 < \frac{[226\text{Ra}]\text{rock}+[226\text{Ra}]\text{spike}}{[228\text{Ra}]\text{rock}+[228\text{Ra}]\text{spike}} < 3$$

Both sample bottles (ID and IC) were placed uncapped into sealed containers near a balance to equilibrate with the environment around the balance. After placing the sample bottle on the balance, once it stabilizes, the spike was pipetted and the weight of the sample bottle before spike addition was recorded. After the spike solution was added, and the weight is recorded again after 45 seconds and once more after another 45 seconds. Evaporation was accounted for by adding the weight difference between the two post-addition readings to the first.

The spiked samples were placed under an IR lamp for slow, low-temperature drying. As ID sample volumes are extremely small, static charge must be avoided to prevent particle dispersion. Each sample must be dried in a separate Teflon drying unit, even if from the same outcrop. Once dry, 100 μL of 8N HNO_3 was added to ID samples and 1 mL of 8N HNO_3 to IC samples. The samples were dried down once more. After this, the samples were ready for column chromatography.

Column Chromatography

U, Th, Ra, and Ba were purified using anion-exchange methods described in Rubin et al. (2005) and Rubin & Zellmer (2009). ID samples were put through ID columns two

doi:10.6342/NTU202503882

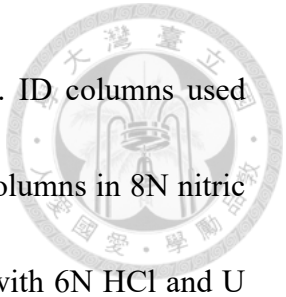

times (the second time is a clean-up column) to extract U and Th. ID columns used AG1X8 200–400 mesh resin (Eichron). Samples were loaded onto columns in 8N nitric acid. Cations were washed out using 8N nitric acid. Th was eluted with 6N HCl and U was eluted with 1N HBr. The wash was then put through a Ba primary column to extract Ba. IC samples were put through an IC column followed by an ID cleanup column to extract U and Th. IC columns used AG1X8 100–200 mesh resin (Eichron). Cations were washed out using 8N nitric acid. Th was eluted with 6N HCl and U was eluted with 1N HBr. The wash was then put through three different columns to extract Ra: the first is a radium primary column to extract Ra and Ba, the second is a Ra/Ba separation clean-up column to remove Ba, and the last was a hydrocarbon clean-up column that removes residual organic material.

Analysis of U and Th Concentrations (ID) and Isotopic Composition (IC)

U and Th concentrations were measured by loading U and Th samples onto colloidal graphite on Re filaments and analyzing them with a thermal ionization mass spectrometer (TIMS) using a Sector 54-WARP at the University of Hawaii at Manoa (Rubin et al., 2005). U and Th IC analysis was conducted on a Nu Plasma HR multicollector inductively coupled plasma mass spectrometer (MC-ICP-MS) at the University of Hawaii at Manoa using analytic procedures described in Rubin et al. (2005) and Zellmer et al. (2015). The results were then used to calculate internal isochron ages using IsoplotR (Vermeesch,

doi:10.6342/NTU202503882

2018).

Analysis of Ra and Ba Concentrations

Due to unforeseen circumstances, Ra and Ba samples were never analyzed. Otherwise, they would have been analyzed on a TIMS using analytic procedures described in Rubin et al. (2005) and Rubin & Zellmer (2009).

B. Ar–Ar Analysis

A Total of 17 lava flow rock samples were collected from the morphologically younger volcanoes of TVG, Shamao, Cising, Huangzuei, and Honlu, and an older volcano, Chutze, for Ar–Ar dating (Figure 4). Three of them were outcrop samples from Shamao and Honlu, the rest were core samples. Shamao outcrop samples were the same rock samples used in U–Th–Ra analysis (Shamao 2-A and Shamao 3-B). All rock samples were checked for alterations and put through mineral separation via magnetic separation and heavy liquid methods to extract groundmass and crystals: plagioclase, amphibole, pyroxene, magnetite, zircon, and apatite. Groundmass and amphibole samples were then sent to the AGES (Argon Geochronology for the Earth Sciences) laboratory at the Lamont-Doherty Earth Observatory of Columbia University to conduct Ar–Ar step-heating analyses. Analytic procedures are as described in Chang et al. (2012, 2014). Irradiated samples were analyzed using a VG-5400 noble gas mass spectrometer.

Groundmass Ar–Ar age analysis was performed on all 17 rock samples, and a second

doi:10.6342/NTU202503882

aliquot was analyzed for 2 Mt. Shamao outcrop samples, 5 Mt. Cising core samples, and 1 Mt. Honlu outcrop sample, making it a total of 25 groundmass analyses. Hornblende Ar–Ar ages were analyzed for 3 Mt. Cising samples; 9 plagioclase analyses were done on Mt. Shamao outcrop samples, Mt. Cising samples, Mt. Honlu samples, and Mt. Chutze.

Plateaus were defined as described in Fleck et al. (1977): contiguous steps in an age spectrum that represent more than 50% of the total ^{39}Ar released and for which no difference in age exists between any two steps at the 95% confidence level. Plateau ages corrected with trapped initial argon calculated from the isochron was preferred when possible, but an assumed initial atmosphere value of $^{40}Ar/^{36}Ar = 298.56$ (Lee et al., 2006) was used if the trapped initial value was not well-defined. When no plateau age could be determined, an isochron age was obtained from an inverse isochron diagram ($^{36}Ar/^{40}Ar$ versus $^{39}Ar/^{40}Ar$).

VI. Results

A. U–Th–Ra Results

The U and Th ID and IC data can be found in Table 2 and 3 and plotted on the U–Th equiline diagrams in (Figure 6). As stated before, Ra and Ba samples were not analyzed. Blanks were also not analyzed. Nonetheless, ^{238}U–^{230}Th results can be compared with the Shamao data in Zellmer et al. (2015) to confirm the validity of the ages in that study.

Two of the groundmass samples, Shamao 2-B and Shamao 3-B, were later found to

doi:10.6342/NTU202503882

be only partially dissolved during processing. Hence, their thorium concentrations were lower than those of their duplicates (Shamao 2-A and Shamao 3-A, respectively). Therefore, Shamao 2-B's and Shamao 3-B's groundmass results will not be used for further discussion. Shamao 3-B's plagioclase Th IC sample was never analyzed due to unforeseen circumstances, and Shamao 3-A's plagioclase results were used in its place for internal isochron calculations.

doi:10.6342/NTU202503882

Table 2: U and Th compositions of Shamao 2 groundmass and mineral separates.

	Sample		Th (ppm)	+/-2s	U (ppm)	+/-2s	(^{238}U/^{232}Th)	+/-2σ	(^{230}Th/^{232}Th)	+/-2σ
Shamao 2	Shamao 2-A	gm	4.429	0.005	1.410	0.002	0.966	0.002	0.890	0.008
		gm-Th IC rerun							*0.894*	*0.025*
		plag	0.404	0.001	0.124	0.001	0.930	0.005	0.903	0.014
		plag-Th IC rerun							*0.888*	*0.014*
		px	0.263	0.000	0.105	0.000	1.215	0.003	0.921	0.006
	Shamao 2-B	gm	~~*3.927*~~	~~*0.004*~~	~~*1.456*~~	~~*0.001*~~	~~*1.125*~~	~~*0.002*~~	~~*0.884*~~	~~*0.025*~~
		plag	0.385	0.001	0.118	0.000	0.930	0.003	0.955	0.019
		px	0.279	0.000	0.090	0.000	0.975	0.003	0.935	0.006
	Amph (I)		0.609	0.002	0.170	0.000	0.848	0.003	0.961	0.019
	Amph (II)		0.639	0.001	0.408	0.001	1.938	0.006	0.975	0.019
	mt		0.402	0.000	0.303	0.000	2.287	0.004	1.241	0.008

doi:10.6342/NTU202503882

Table 3: U and Th compositions of Shamao 3 groundmass and mineral separates.

	Sample		Th (ppm)	+/-2s	U (ppm)	+/-2s	(^{238}U/^{232}Th)	+/-2σ	(^{230}Th/^{232}Th)	+/-2σ
Shamao 3	Shamao 3-A	gm	5.458	0.006	1.599	0.001	0.889	0.001	0.889	0.008
		gm-Th IC rerun							*0.894*	*0.025*
		plag	0.726	0.001	0.120	0.000	0.502	0.002	0.951	0.015
		px	0.311	0.000	0.145	0.000	1.416	0.005	1.001	0.007
	Shamao 3-B	gm	~~*4.026*~~	~~*0.004*~~	~~*1.644*~~	~~*0.002*~~	~~*1.239*~~	~~*0.002*~~	~~*0.882*~~	~~*0.017*~~
		plag	0.603	0.001	0.128	0.000	0.644	0.002	N/A	N/A
		px	0.260	0.000	0.039	0.0001	0.456	0.002	0.939	0.006
	Amph (I)		0.676	0.002	0.153	0.000	0.687	0.002	1.007	0.020
	Amph (II)		0.700	0.001	0.472	0.001	2.044	0.005	1.005	0.020
	mt		0.537	0.001	0.359	0.000	2.032	0.004	1.419	0.010

doi:10.6342/NTU202503882

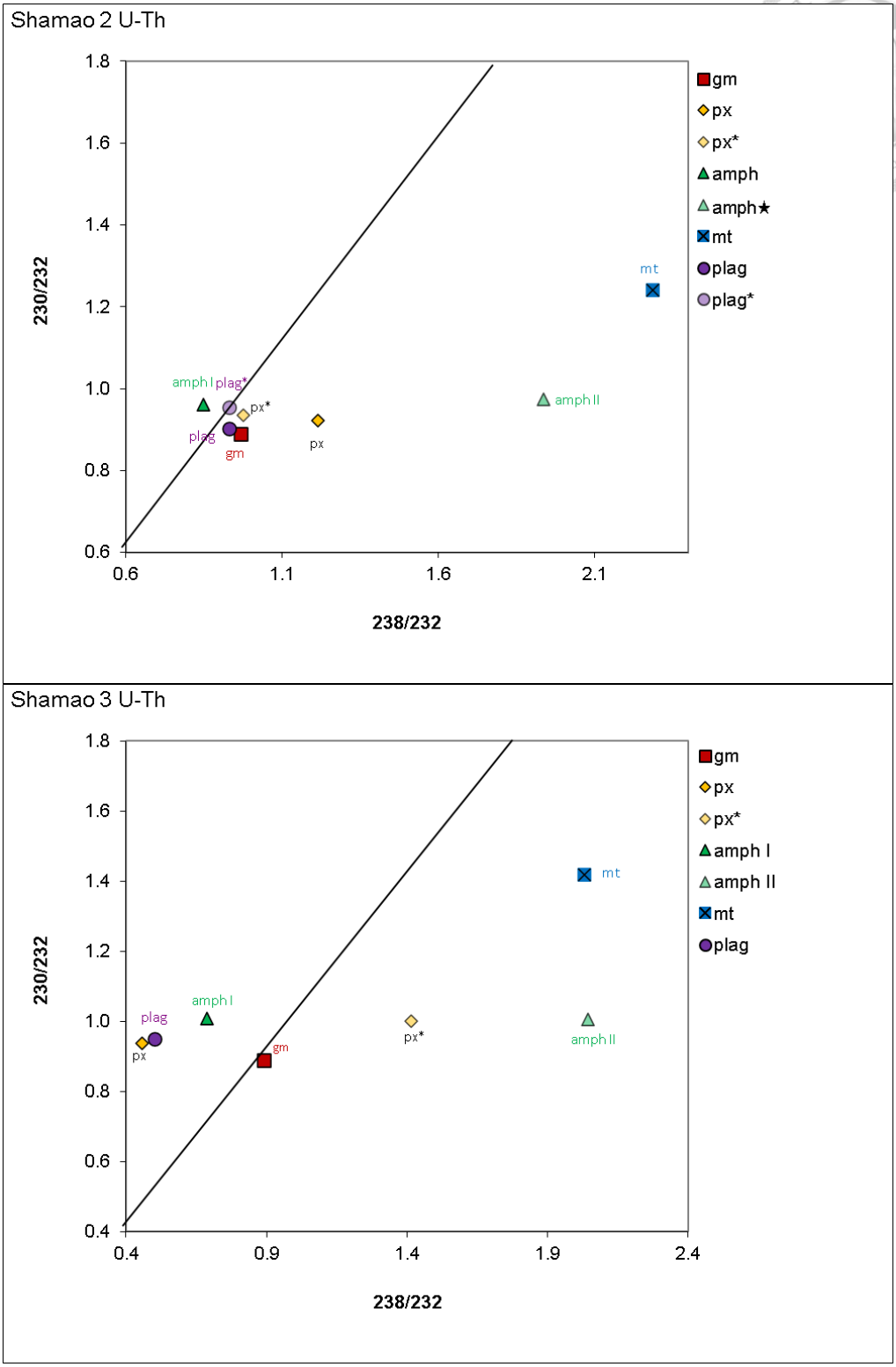

Figure 6: U–Th equiline diagrams of Shamao separates.
The equiline is the line in the diagram where ($^{238}U/^{232}Th$) = ($^{230}Th/^{232}Th$). Analytical uncertainties are smaller than the symbol size. gm, groundmass; px, pyroxene; amph, amphibole; mt, magnetite; plag, plagioclase.

doi:10.6342/NTU202503882

All groundmass samples plot close to the equiline, signifying ^{238}U–^{230}Th equilibrium. Shamao 2-A's groundmass has a slight amount of U excess. Shamao 2 plagioclase separates plot close to the equiline. 2-A plagioclase separates have U excess, while 2-B and 3-A have Th excesses, with 3-A's excess being particularly large. Shamao 2 plagioclase duplicates have similar concentrations (ID's), whereas 3-A has a higher Th concentration than 3-B. The pyroxene separates from 2-B are nearly in ^{238}U-^{230}Th equilibrium, while 2-A and 3-A pyroxene separates have U excesses and 3-B pyroxenes have Th excess. Shamao 2 pyroxene duplicates have identical ID's, whereas 3-A pyroxene separates have a slightly higher Th concentration than 3-B and a much higher U concentration. All amphibole separates demonstrate U–Th disequilibria: Shamao 2-I and Shamao 3-I have Th excesses while Shamao 2-II and Shamao 3-II have large U excesses. Although, 2-I amphiboles only have a small amount of Th excess and plots close to the equiline. Amphiboles from the same sample have similar Th concentrations, but II's have much higher U concentrations than I's. both Shamao 2 and 3 magnetite separates exhibit large U excesses.

In general, with the exception of 3-B's pyroxene separates, Shamao 3 groundmass and mineral separates have higher Th concentrations than their Shamao 2 counterparts. And, with the exception of all plagioclase separates and 3-B's pyroxene separates, Shamao 3 groundmass and mineral separates have higher U concentrations than their

doi:10.6342/NTU202503882

Shamao 2 counterparts. All duplicates exhibit ID and IC results that differ from those of their counterparts. They are inconsistent.

Much like the Shamao results from Zellmer et al. (2015), Shamao 2 and 3 did not yield robust internal isochrons when using groundmass and all mineral phases. Despite that, internal U-Th ages can be estimated using the mineral–mineral pairs listed in (Zellmer et al., 2015).

Shamao 2 did not yield robust groundmass–pyroxene–magnetite ages like in (Zellmer et al., 2015). Groundmass–magnetite and pyroxene–magnetite two-point isochron ages were calculated, instead. A groundmass–magnetite isochron yielded an age of 33.7 ± 1.3 ka (2σ). Pyroxene–magnetite isochrons yielded ages 38.7 ± 1.5 ka (2σ) using 2-A pyroxenes and 29.0 ± 1.1 ka (2σ) using 2-B pyroxenes. A plagioclase–magnetite age of 31.2 ± 1.7 ka (2σ) can be estimated using 2-A plagioclase separates, and an age of 25.8 ± 2.1 ka (2σ) can be estimated using 2-B plagioclase separates. An amphibole–magnetite age of 23.6 ± 1.9 ka (2σ) can be estimated using 2-I amphiboles, and an age of 157 ± 28 ka (2σ) can be estimated using 2-II amphiboles. Excluding the amphibole–magnetite age calculated with 2-II amphiboles, Shamao 2 ages fall between 21 and 40 ka.

doi:10.6342/NTU202503882

Table 4: U–Th isochron ages.

Sample	Isochron Pair	U–Th Age (ka, 2σ)
Shamao 2	groundmass–magnetite	33.7 ± 1.3
	pyroxene–magnetite	38.7 ± 1.5, 29.0 ± 1.1
	plagioclase–magnetite	31.2 ± 1.7, 25.8 ± 2.1
	amphibole I–magnetite	23.6 ± 1.9
	amphibole II–magnetite	157 ± 28
Shamao 3	groundmass–magnetite	67.9 ± 2.3
	pyroxene–magnetite	123.8 ± 7.1, 39.6 ± 1.2
	plagioclase–magnetite	39.8 ± 1.9
	amphibole I–magnetite	39.9 ± 2.6
	amphibole II–magnetite	negative age

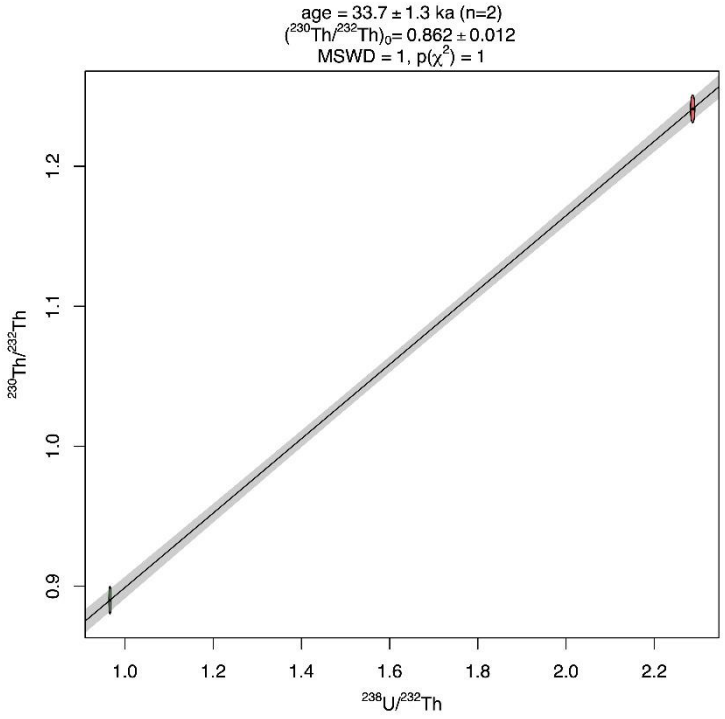

Figure 7: Shamao 2 groundmass–magnetite isochron.

doi:10.6342/NTU202503882

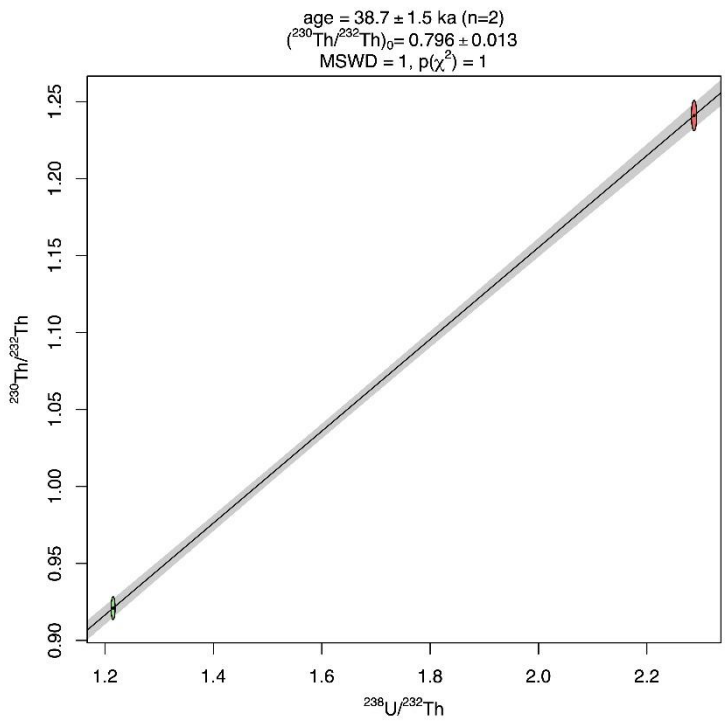

Figure 8: Shamao 2 pyroxene–magnetite isochron using 2A pyroxene.

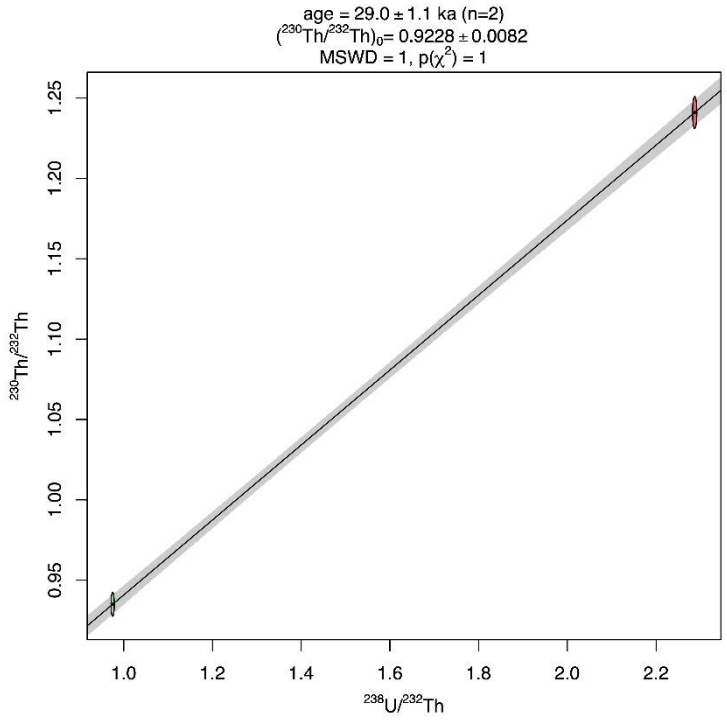

Figure 9: Shamao 2 pyroxene–magnetite isochron using 2B pyroxene.

doi:10.6342/NTU202503882

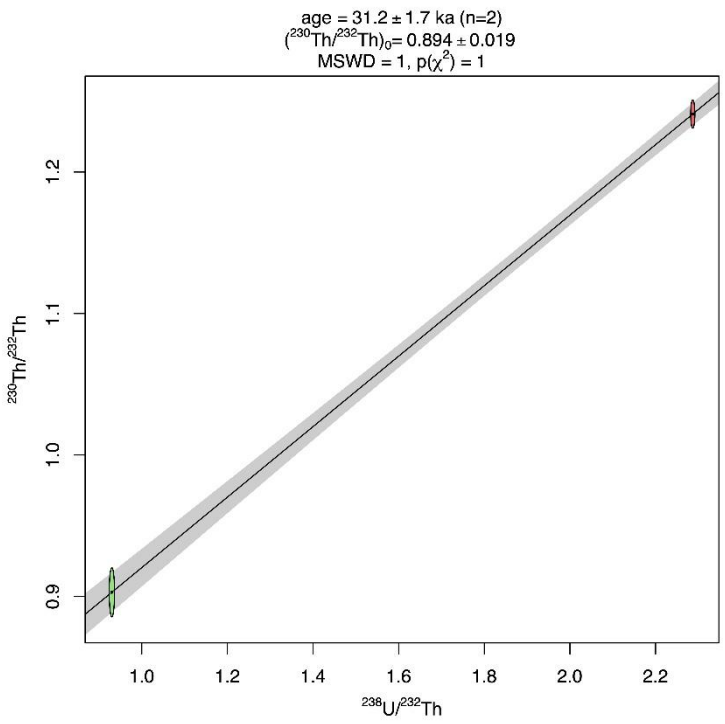

Figure 10: Shamao 2 plagioclase–magnetite isochron using 2A plagioclase.

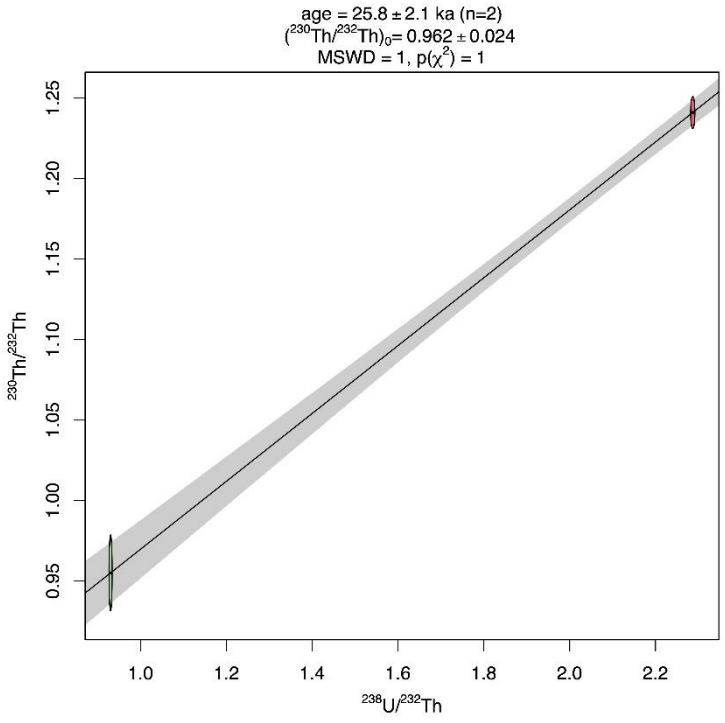

Figure 11 Shamao 2 plagioclase–magnetite isochron using 2B plagioclase.

doi:10.6342/NTU202503882

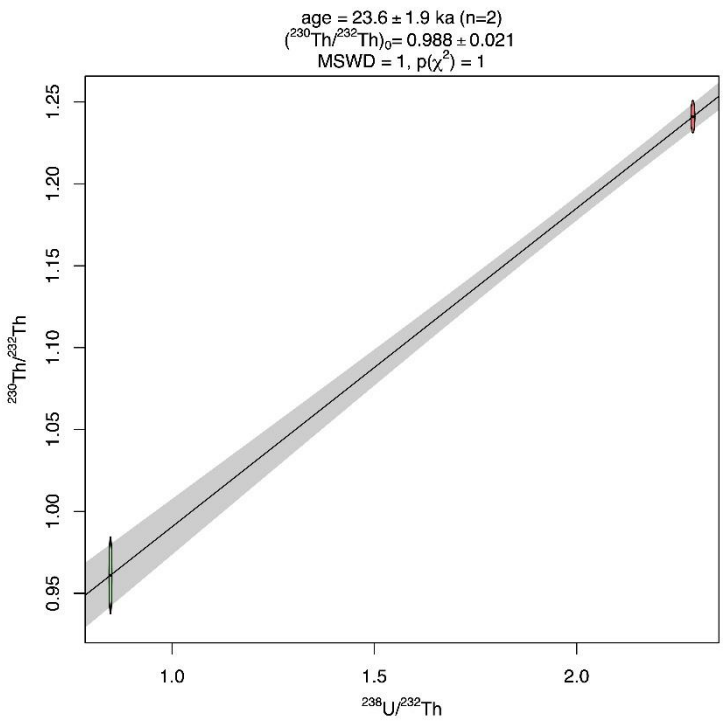

Figure 12 Shamao 2 amphibole–magnetite isochron using 2I amphibole.

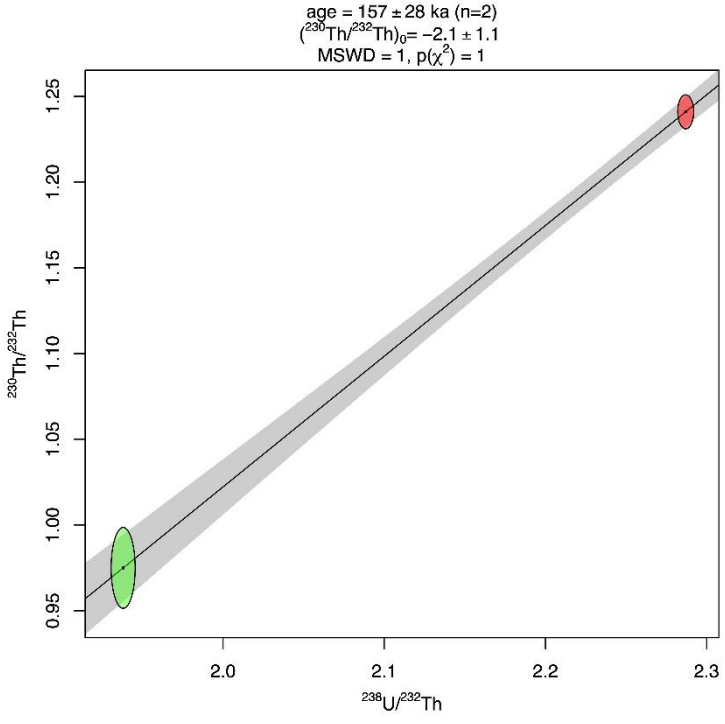

Figure 13: Shamao 2 amphibole–magnetite isochron using 2II amphibole.

Shamao 3 also did not yield a robust groundmass–pyroxene–magnetite isochron. A

doi:10.6342/NTU202503882

groundmass–magnetite isochron yielded an age of 67.9 ± 2.3 ka (2σ). Pyroxene–magnetite isochrons yielded ages 123.8 ± 7.1 ka (2σ) using 3-A pyroxenes and 39.6 ± 1.2 ka (2σ) using 3-B pyroxenes. A plagioclase–magnetite age of 39.8 ± 1.9 ka (2σ) can be estimated using 3-A plagioclase separates. An amphibole–magnetite age of 39.9 ± 2.6 ka (2σ) can be estimated using 3-I amphiboles. 3-II amphiboles would give an amphibole–magnetite isochron a negative age which would be improbable. Shamao 3 ages fall between 38 and 130 ka.

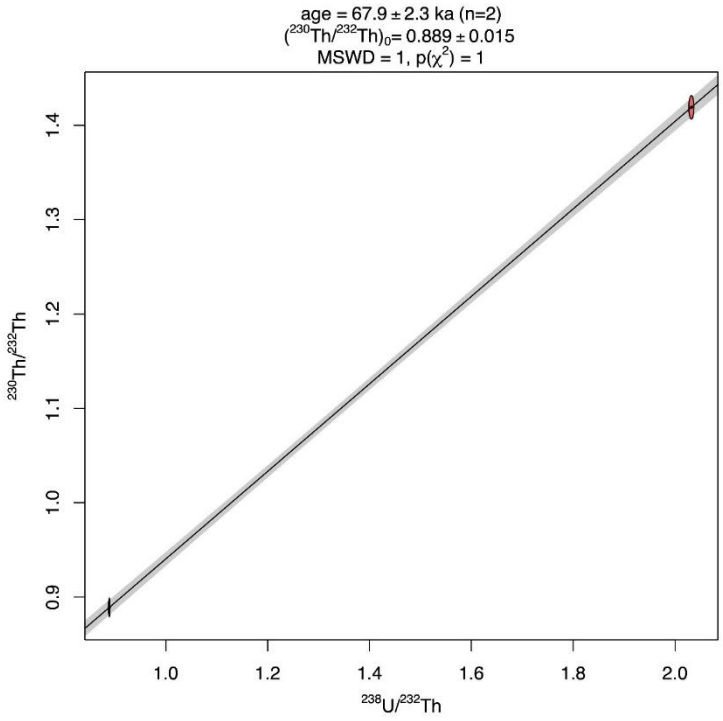

Figure 14: Shamao 3 groundmass–magnetite isochron.

doi:10.6342/NTU202503882

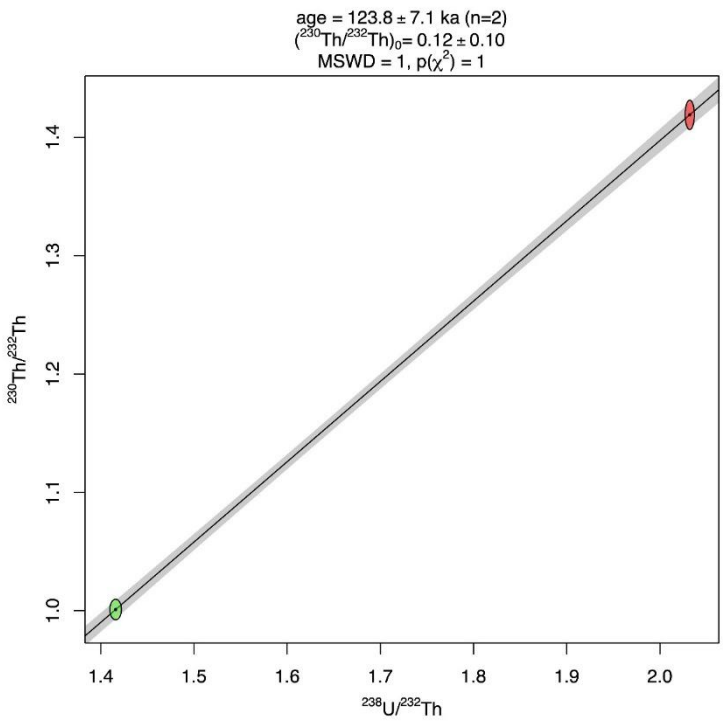

Figure 15: Shamao 3 pyroxene–magnetite isochron using 3A pyroxene.

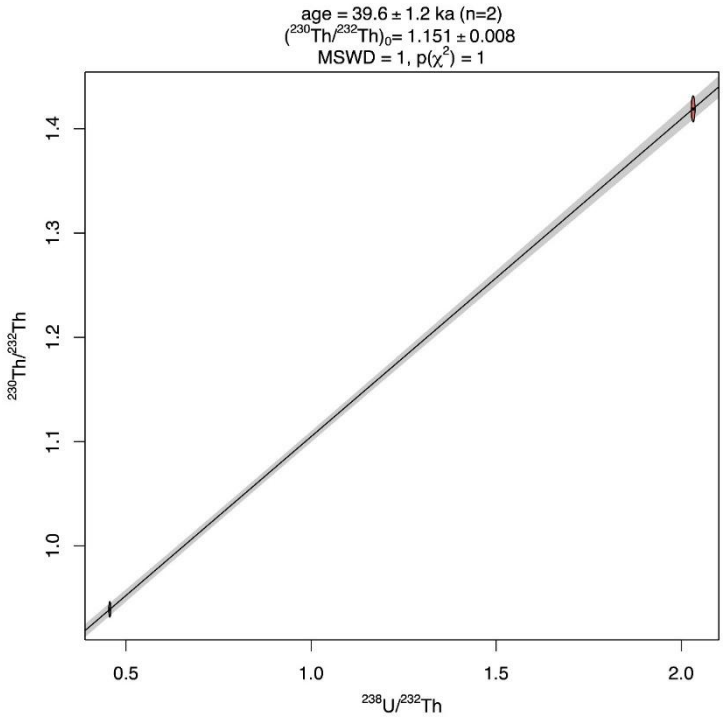

Figure 16: Shamao 3 pyroxene–magnetite isochron using 3B pyroxene.

doi:10.6342/NTU202503882

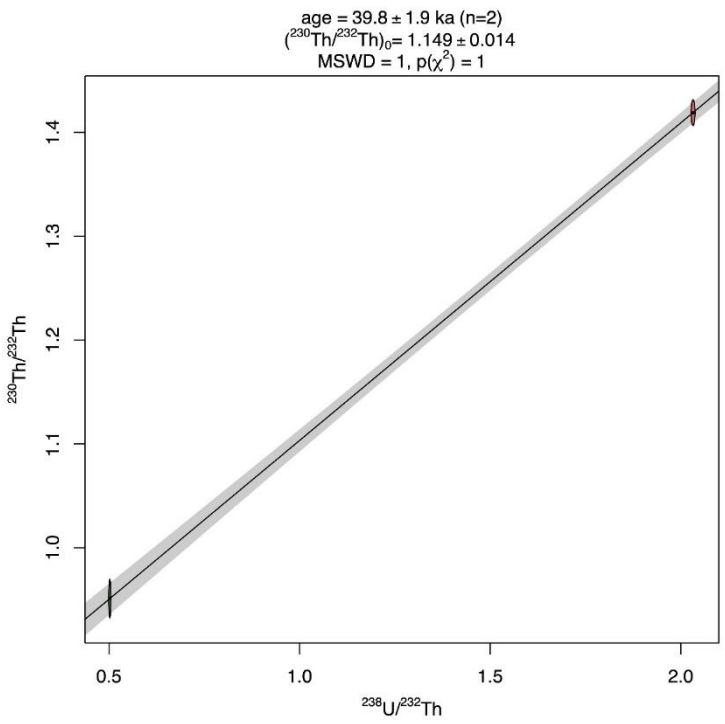

Figure 17: Shamao 3 plagioclase–magnetite isochron using 3A plagioclase.

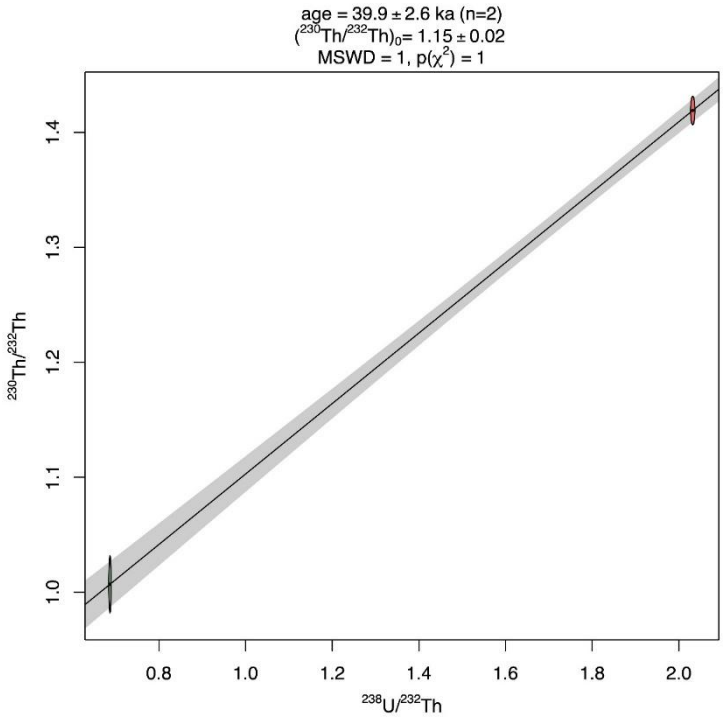

Figure 18: Shamao 3 amphibole–magnetite isochron using 3A amphibole.

B. Ar–Ar Results

From the 17 rock samples in TVG collected and a total of 22 Ar–Ar ages and 2

doi:10.6342/NTU202503882

estimates were obtained, including 21 groundmass ages and 3 hornblende ages. These are reported in Table 5~11, and their corresponding age spectrums and isochron diagrams can be found in the Appendix. Errors are all reported as 1σ. Four groundmass analyses, one aliquot each from 2 Mt. Shamao outcrop samples and 2 Mt. Cising core samples, were unsuccessful due to low radiogenic Ar content and unidentifiable plateau or isochron ages. Groundmass initial Ar is slightly higher than atmospheric Ar for all but 2 samples from Mt. Chutze and Mt. Huangzuei, which were composed of mixed components. No single population could be cleanly isolated for these 2 samples. All hornblende samples have higher initial Ar (< 1%) than atmospheric values and measured older than their groundmass counterparts. Most samples are of low radiogenic argon, mixed phases, and contain non-radiogenic argon, resulting in messy isochrons and not very well-defined initial compositions, all of which lead to dubious results.

1. Outcrop Results

a. Honlu Outcrop Results

In the first aliquot of the Honlu outcrop groundmass sample, large uncertainties on the age spectrum and corresponding variable $^{39}Ar_K/^{37}Ar_{Ca}$ ratios can be observed in low temperature steps. These steps can be identified as a different component on the inverse isochron diagram and were therefore excluded from further calculations. The initial $^{40}Ar/^{36}Ar$, 289.5 ± 9.5, was poorly constrained; thus, an atmospheric initial value was used

doi:10.6342/NTU202503882

to calculate a plateau age of 122.5 ± 7.3 ka. This age is slightly younger than the isochron age of 148.9 ± 18.2 ka.

In the second aliquot, no plateau was observed, the isochron was poorly defined, and the initial $^{40}Ar/^{36}Ar$ value of 289.2 ± 0.7 was lower than atmospheric values. However, an isochron age of 123.8 ± 10.5 ka agrees well with the plateau age of the first aliquot. Therefore, the preferred age for the Honlu outcrop groundmass sample is the plateau age from the first aliquot: 122.5 ± 7.3 ka.

Table 5: Honlu Outcrop Ar–Ar Results

Sample	Best Age (ka)	+/-	Initial $^{40/36}Ar$	+/-	Age Type
HLS-01 (1)	122.5	7.3	289.5	9.5	plateau age (trapped initial)
HLS-01 (2)	123.8	10.5	289.2	0.7	isochron age

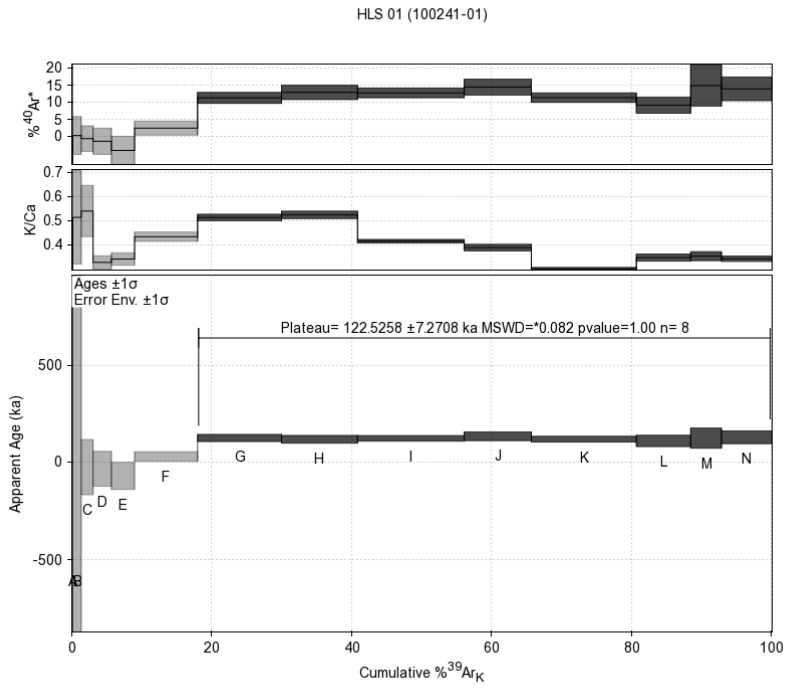

Figure 19: HLS-01 groundmass aliquot 1 age spectrum (air initial).

doi:10.6342/NTU202503882

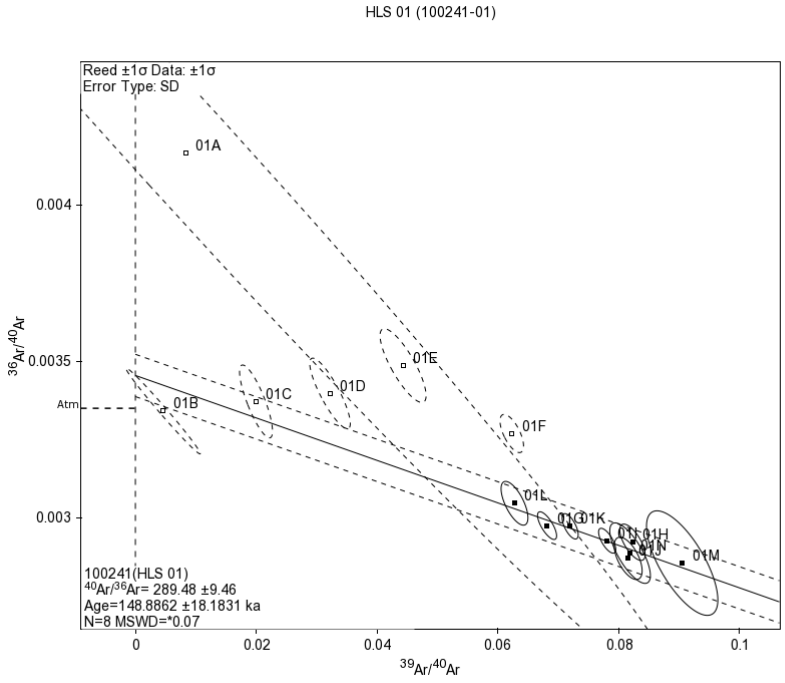

Figure 20: HLS-01 groundmass aliquot 1 isochron (plateau only steps).

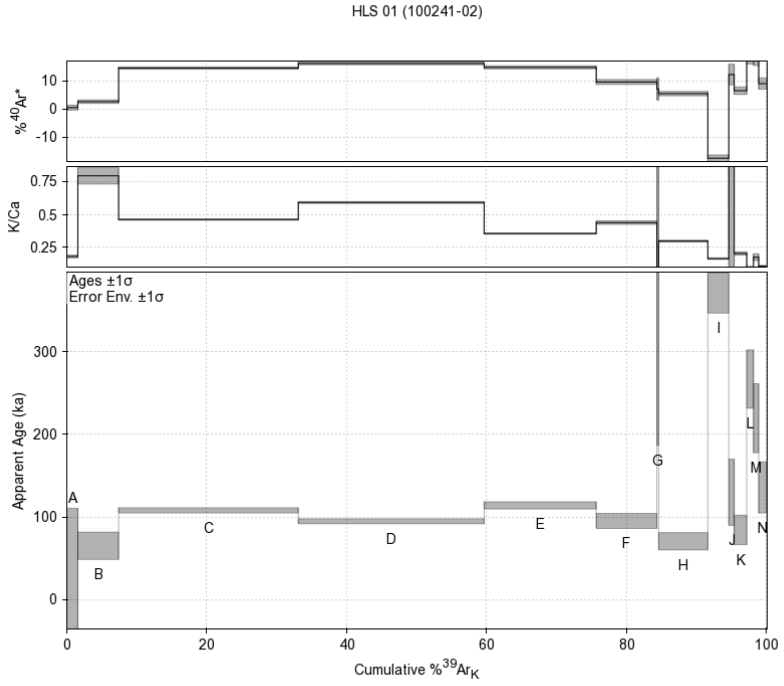

Figure 21: HLS-01 groundmass aliquot 2 age spectrum (air initial).

doi:10.6342/NTU202503882

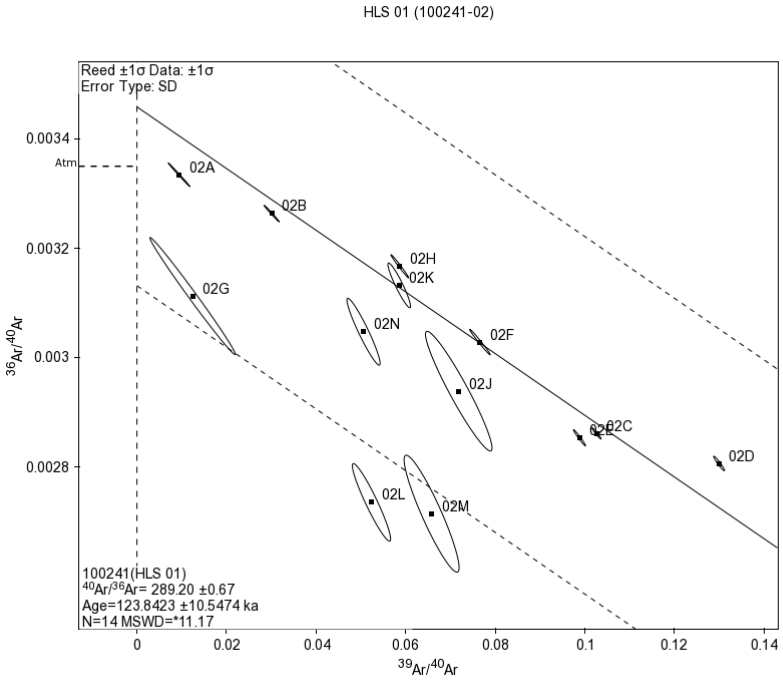

Figure 22: HLS-01 groundmass aliquot 2 isochron.

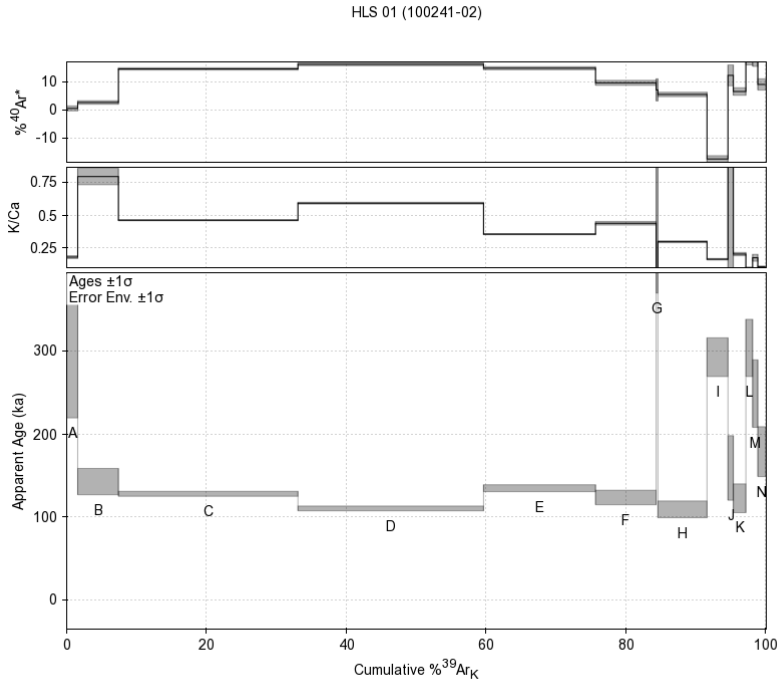

Figure 23: HLS-01 groundmass aliquot 2 age spectrum (trapped initial)

doi:10.6342/NTU202503882

b. Shamao Outcrop Results

Each of the two Shamao outcrop groundmass samples yielded one successful run from which plateau ages were obtained. The initial $^{40}Ar/^{36}Ar$ values were similar to atmospheric composition, and the plateau and isochron ages agree well. Aliquot 1 of Shamao 2-A did not produce usable results. In aliquot 2, several low ^{39}Ar steps that were removed from the isochron calculation. The initial $^{40}Ar/^{36}Ar$ was calculated to be 298.0 ± 0.2. A plateau age of 76.1 ± 4.4 ka was obtained, which is in good agreement with the isochron age of 74.3 ± 9.6 ka.

Aliquot 1 of Shamao 3-B was also unsuccessful due to low gas content. Aliquot 2 produced an age spectrum on very low argon yields, resulting in large uncertainties and a highly scattered distribution on the isochron diagram. The initial $^{40}Ar/^{36}Ar$ was calculated as 299.8 ± 0.3, and the plateau age was 120.1 ± 19.9 ka, which coincides with the isochron age of 148.9 ± 18.2 ka. Due to the low radiogenic argon content, the correction for atmospheric contamination is too large to yield a reliable age. As such, the actual uncertainty is likely much greater than reported.

The preferred age for Shamao 2-A is 76.1 ± 4.4 ka, and for Shamao 3-B is 120.1 ± 19.9 ka.

doi:10.6342/NTU202503882

Table 6: Shamao Outcrop Ar–Ar Results

Sample	Best Age (ka)	+/- 1σ	Initial $^{40/36}$Ar	+/- 1σ	Age Type
Shamao 2-A (1)	Not datable		289.3	15.4	
Shamao 2-A (2)	76.1	4.4	298.0	0.2	plateau age (trapped initial)
Shamao 3-B (1)	Not datable		304.5	0.5	
Shamao 3-B (2)	120.1	19.9	299.8	0.3	plateau age (trapped initial)

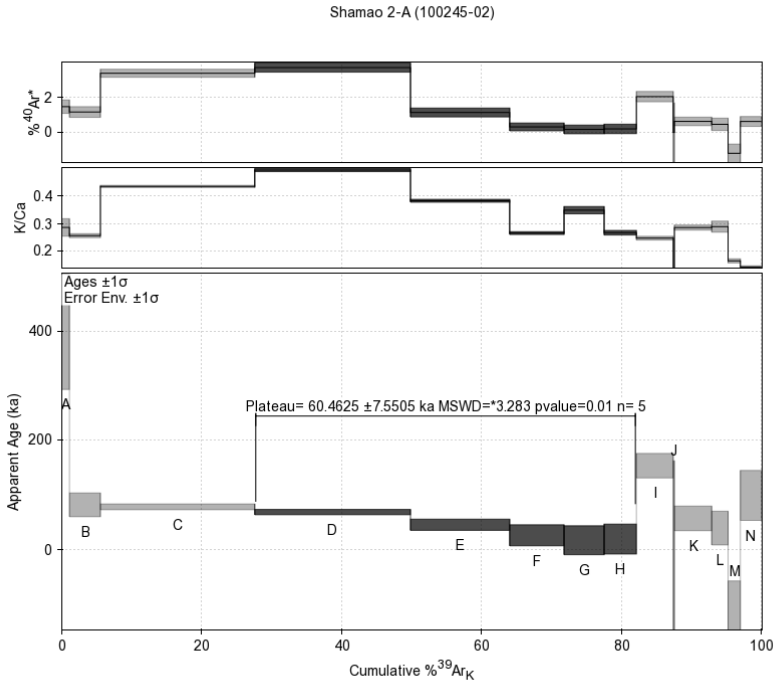

Figure 24: Shamao 2-A groundmass aliquot 2 age spectrum (air initial).

doi:10.6342/NTU202503882

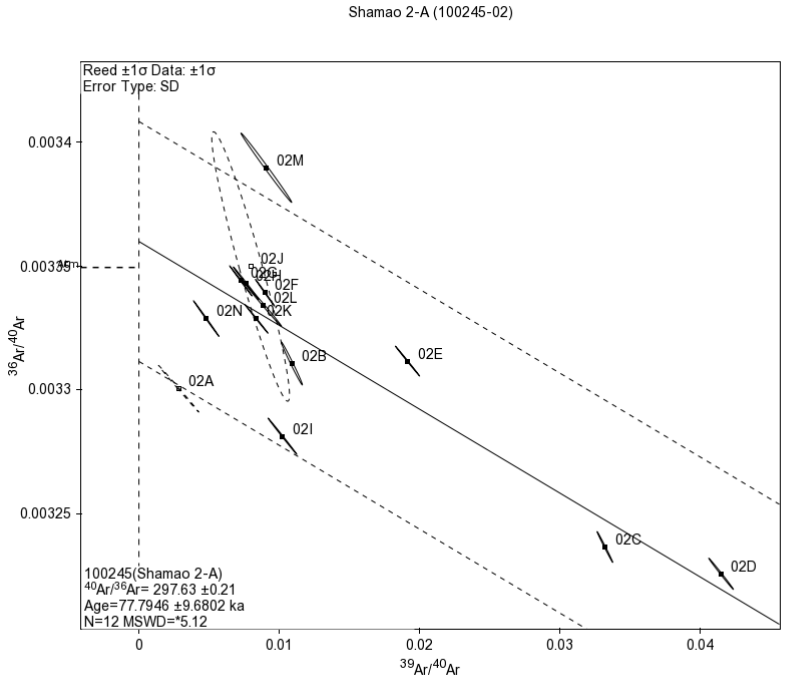

Figure 25: Shamao 2-A groundmass aliquot 2 isochron (discarding low ^{39}Ar steps).

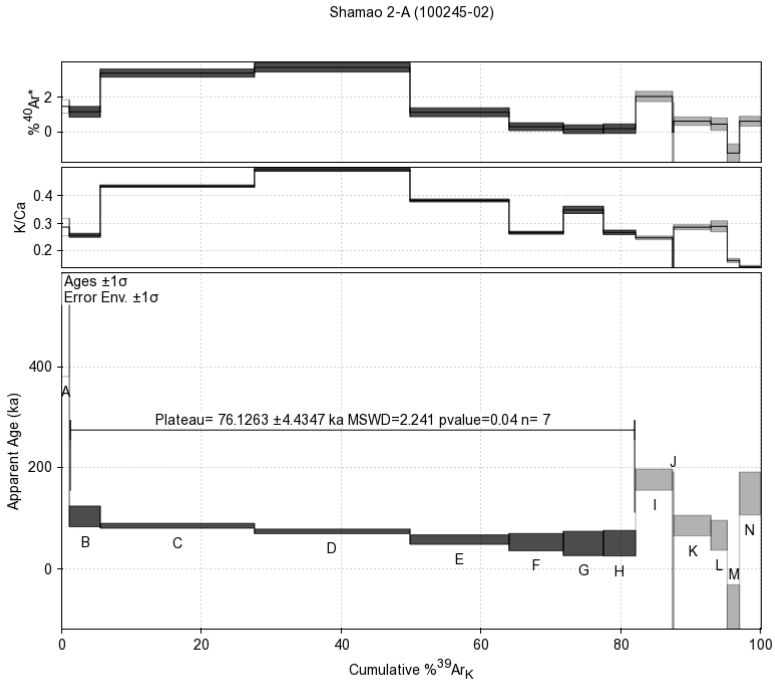

Figure 26: Shamao 2-A groundmass aliquot 2 age spectrum (trapped initial).

doi:10.6342/NTU202503882

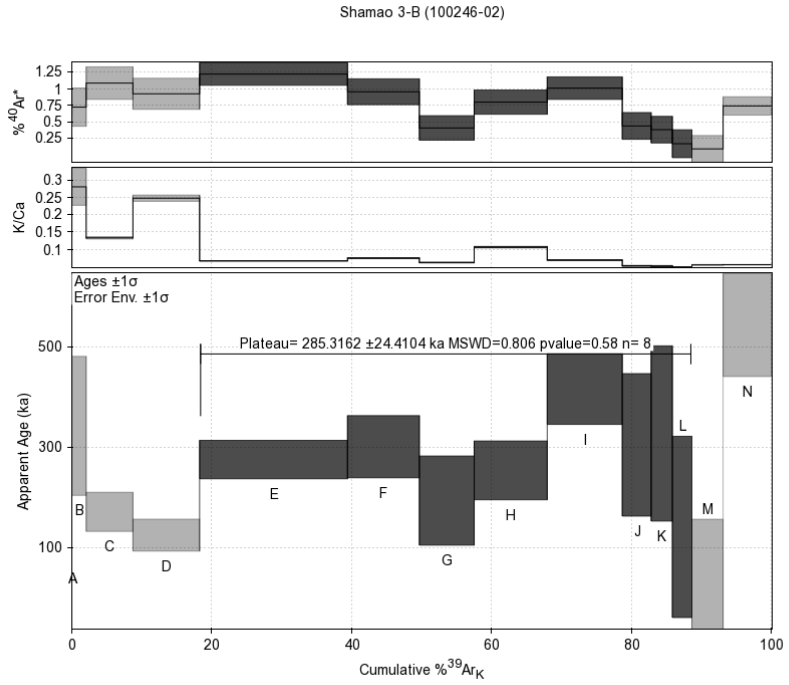

Figure 27: Shamao 3-B groundmass aliquot 2 age spectrum (air initial).

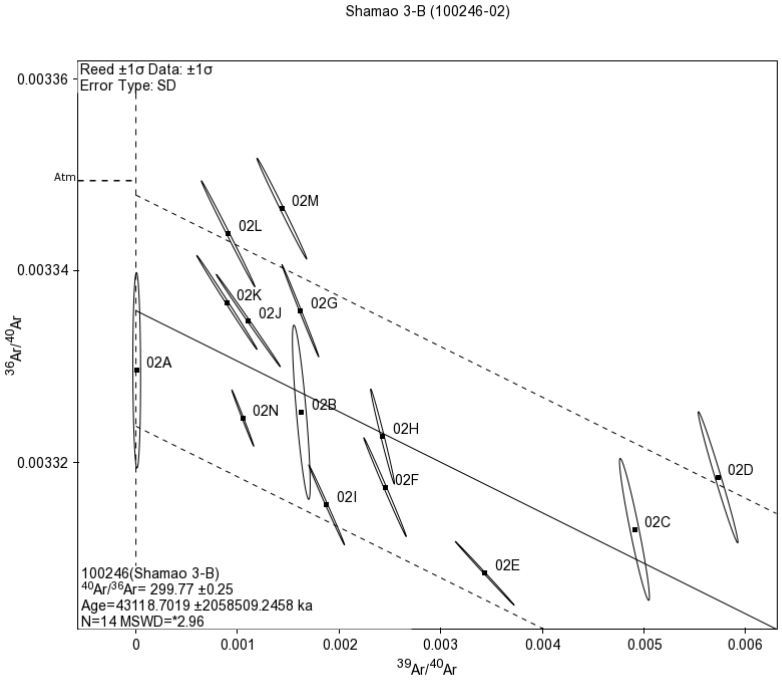

Figure 28: Shamao 3-B groundmass aliquot 2 isochron.

doi:10.6342/NTU202503882

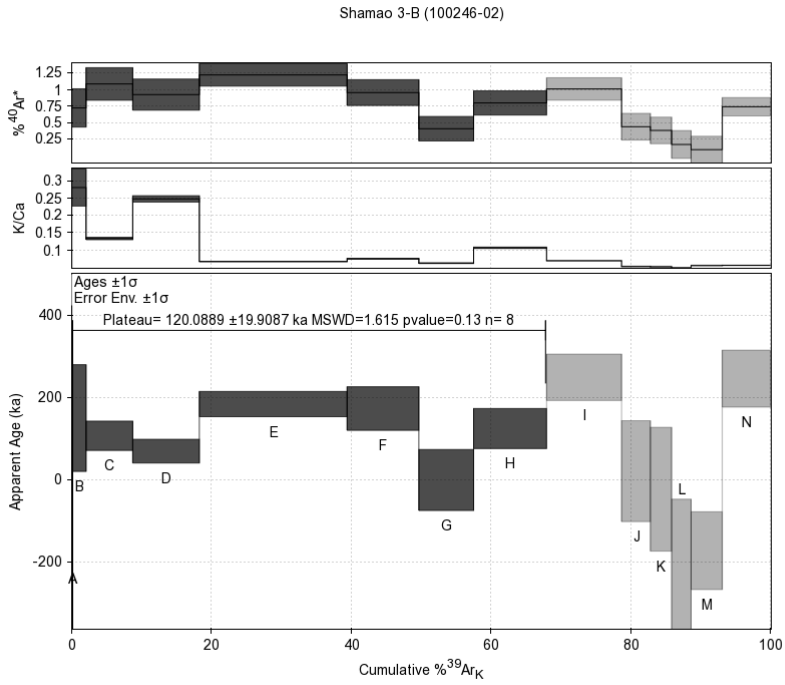

Figure 29: Shamao 3-B groundmass aliquot 2 age spectrum (trapped initial).

2. Borehole Sample Results

a. TTVG-BH16 Results

The TTVG-BH16 borehole groundmass samples yielded relatively well-behaved isochrons, with initial $^{40}Ar/^{36}Ar$ values consistent with atmospheric composition. All samples exhibited large uncertainties in apparent ages at low-temperature steps, associated with low radiogenic argon content.

The TTVG-BH16-138139 groundmass sample produced an initial $^{40}Ar/^{36}Ar$ value of 297.3 ± 0.2. Its isochron age, 212.2 ± 3.1 ka, is slightly younger than the plateau age, 223.8 ± 4.7 ka.

The TTVG-BH16-185186 groundmass sample produced an initial $^{40}Ar/^{36}Ar$ value

doi:10.6342/NTU202503882

of 298.2 ± 1.7. The isochron age of 207.1 ± 3.0 is in agreement with its plateau age of 207.5 ± 3.8 ka, derived from a plateau encompassing all steps. The preferred ages are the plateau ages: 223.8 ± 4.7 ka for TTVG-BH16-138139 and 207.5 ± 3.8 ka for TTVG-BH16-185186.

Both samples are from the same lava flow above a lahar at the bottom of the 200-meter-deep borehole and should be similar in age (Figure 87). Given the consistency between plateau and isochron ages for TTVG-BH16-185186, and the agreement of TTVG-BH16-138139's isochron age with those results, the plateau age of 207.5 ± 3.8 ka from TTVG-BH16-185186 is considered the best estimate for this lava flow.

Table 7: TTVG-BH16 Ar–Ar Results

Sample	**Best Age (ka)**	**+/- 1σ**	**Initial$^{40/36}$Ar**	**+/- 1σ**	**Age Type**
TTVG-BH16-138139	223.8	4.7	297.3	0.2	plateau age (trapped initial)
TTVG-BH16-185186	207.5	3.8	298.2	1.7	plateau age (trapped initial)

doi:10.6342/NTU202503882

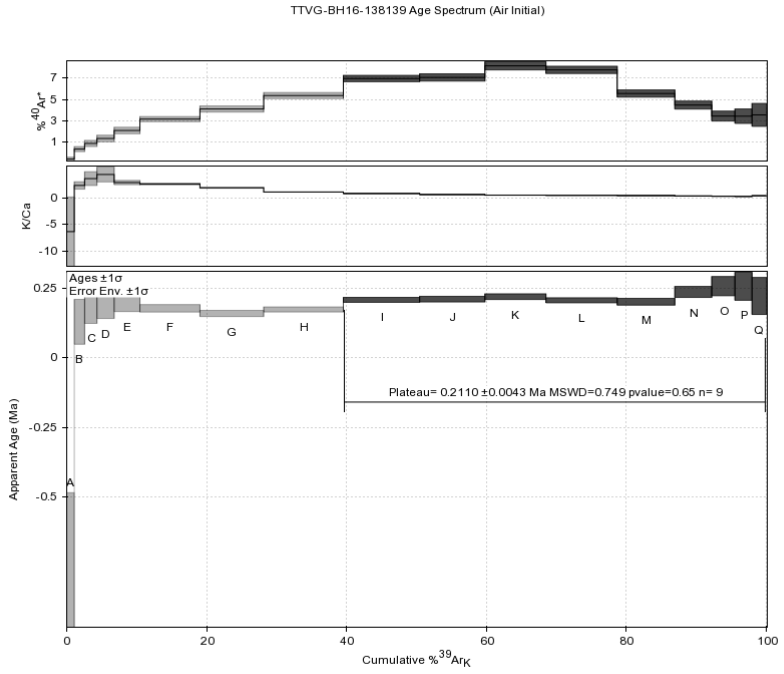

Figure 30: TTVG-BH16-138139 groundmass age spectrum (air initial).

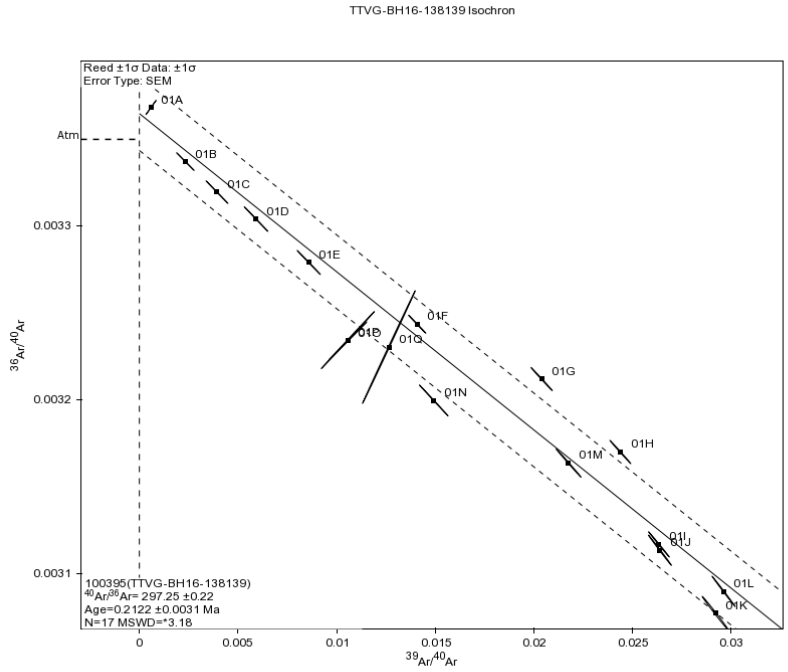

Figure 31: TTVG-BH16-138139 groundmass isochron.

doi:10.6342/NTU202503882

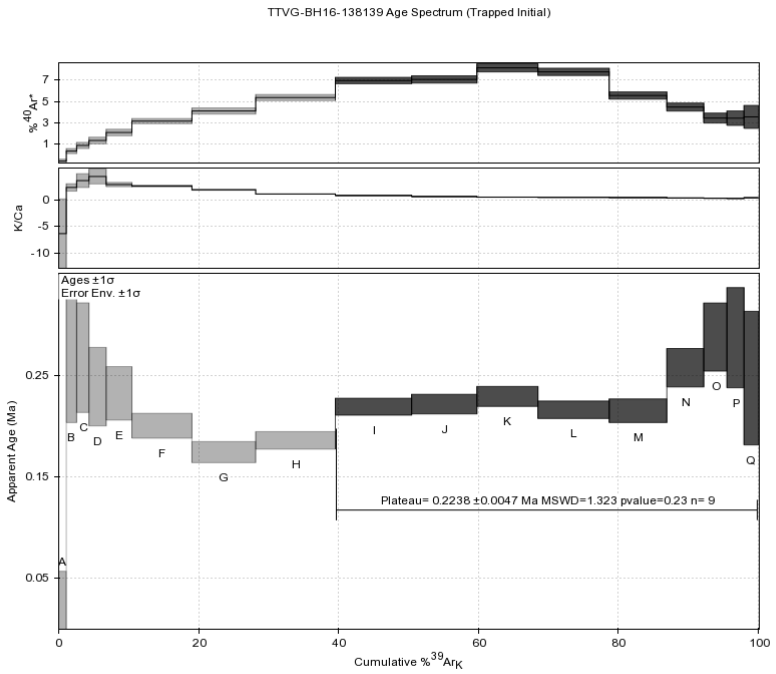

Figure 32: TTVG-BH16-138139 groundmass age spectrum (trapped initial).

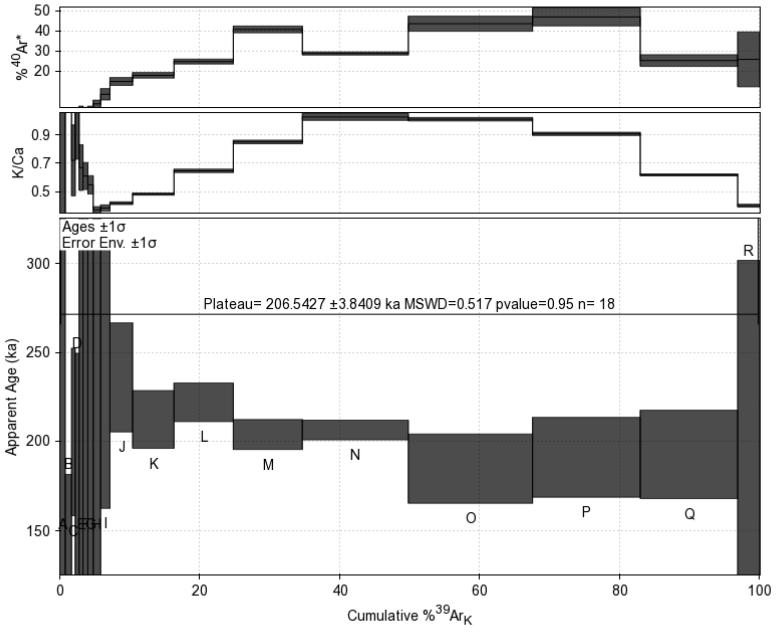

Figure 33: TTVG-BH16-185186 groundmass age spectrum (initial air).

doi:10.6342/NTU202503882

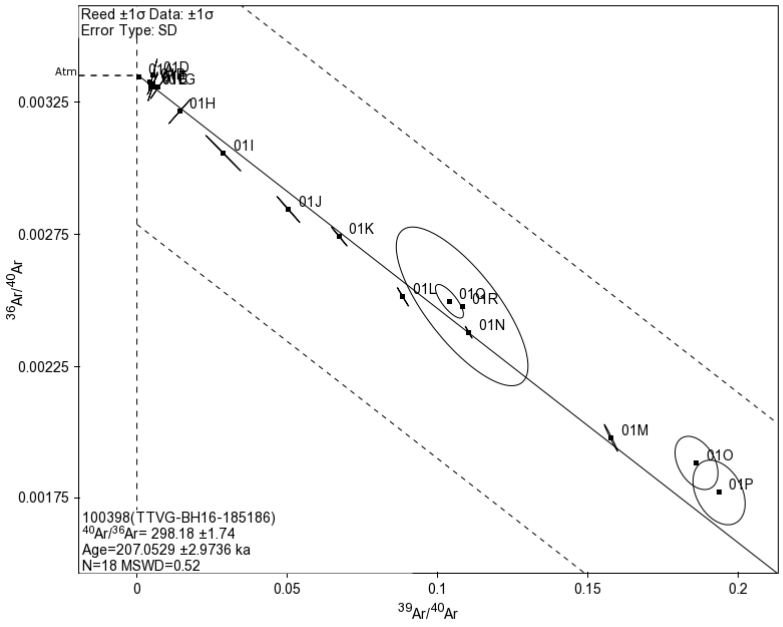

Figure 34: TTVG-BH16-185186 groundmass isochron.

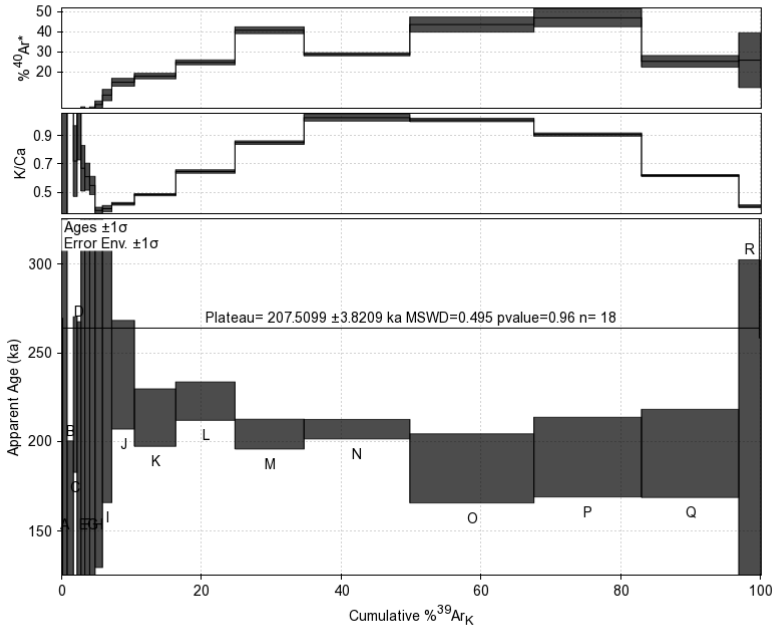

Figure 35: TTVG-BH16-185186 groundmass age spectrum (trapped initial).

b. TTVG-BH11 Results

Borehole TVG-BH11 groundmass samples produced the youngest ages in this study

doi:10.6342/NTU202503882

while an amphibole sample yielded a much older age. Initial $^{40}Ar/^{36}Ar$ values are poorly constrained, resulting in large uncertainties in plateau ages. Samples with determinable trapped initial components show excess argon.

TTVG-BH11-2931 groundmass aliquot 1 produced a slightly saddle-shaped age spectrum. Some studies found this pattern is a result of excess argon originating from melt or fluid inclusions in the beginning steps, and melt, fluid, or solid inclusions in the final steps (Boven et al., 2001; Esser et al., 1997; Kelley, 2002). However, the beginning steps have extremely large uncertainties, along with variable $^{39}Ar_K/^{37}Ar_{Ca}$ ratios and a highly scattered distribution on the isochron plot, it may instead be an indication of minor alterations. Excluding these steps from the isochron yielded an initial $^{40}Ar/^{36}Ar$ of 300.8 ± 0.5 and an isochron age of 26.8 ± 6.6 ka. The corresponding plateau age, 25.8 ± 4.6 ka, is consistent with the isochron age. Aliquot 2 did not produce results.

The amphibole fromTTVG-BH11-2931 showed $^{39}Ar_K/^{37}Ar_{Ca}$ variability in early steps on the age spectrum, likely due to alterations and a scattered isochron gave an age of 148.9 ± 18.2 ka with an initial $^{40}Ar/^{36}Ar$ of 312.0 ± 0.8 that was poorly constrained. An assumed atmospheric initial value was used to calculate a plateau age of 461.2 ± 13.1 ka. The plateau age is not in agreement with the isochron age and the plateau age, 461.2 ± 13.1 ka, is preferred.

Two runs were conducted for the TTVG-BH11-5759 groundmass sample. Aliquot 1

doi:10.6342/NTU202503882

showed large uncertainties in the beginning steps, likely due to alteration, and no usable isochron could be generated. A plateau age of 17.2 ± 6.1 ka was calculated using the assumed atmospheric initial value. Aliquot 2 similarly had low-temperature uncertainties and a scattered isochron, with a plateau age of 30.0 ± 1.7 ka.

TTVG-BH11-8183 groundmass aliquot 1 also lacked a robust isochron; an assumed atmospheric initial yielded a plateau age of 23.9 ± 5.8 ka. Aliquot 2 did not provide results.

Preferred plateau ages are 25.8 ± 4.6 ka for TTVG-BH11-2931 and 23.9 ± 5.8 ka for TTVG-BH11-8183. The TTVG-BH11-5759 groundmass sample duplicates produced two vastly different ages. Aliquot 2, a plateau-only isochron yields an initial $^{40}Ar/^{36}Ar$ similar to atmospheric values and an isochron age that agrees with the plateau age, making the aliquot 2 plateau age, 30.0 ± 1.7 ka, our preferred estimate for the TTVG-BH11-5759 groundmass sample. This result is also in agreement with the TTVG-BH11-2931 groundmass sample from the lava flow above, and the TTVG-BH11-8183 groundmass sample from the same flow. All groundmass ages being of similar age imply that andesites in this core may have erupted in quick succession between 20 to 30 ka (Figure 87). The significantly older amphibole age from TTVG-BH11-2931 suggests those crystals are unrelated to the erupted magma.

doi:10.6342/NTU202503882

Table 8: TTVG-BH11 Ar–Ar Results

Sample	Best Age (ka)	+/- 1σ	Initial $^{40/36}$Ar	+/- 1σ	Age Type
TTVG-BH11-2931 (1)	25.8	4.6	300.8	0.5	plateau age (trapped initial)
TTVG-BH11-2931 (2)	Not datable		300.2	0.3	
TTVG-BH11-2931 (Amphibole)	461.2	13.1	312.0	0.8	plateau age (assumed initial)
TTVG-BH11-5759 (1)	17.2	6.1	294.9	2.4	plateau age (assumed initial)
TTVG-BH11-5759 (2)	30.0	1.7	300.3	1.0	plateau age (assumed initial)
TTVG-BH11-8183 (1)	23.9	5.8	302.6	4.7	plateau age (assumed initial)
TTVG-BH11-8183 (2)	Not datable		297.0	1.2	

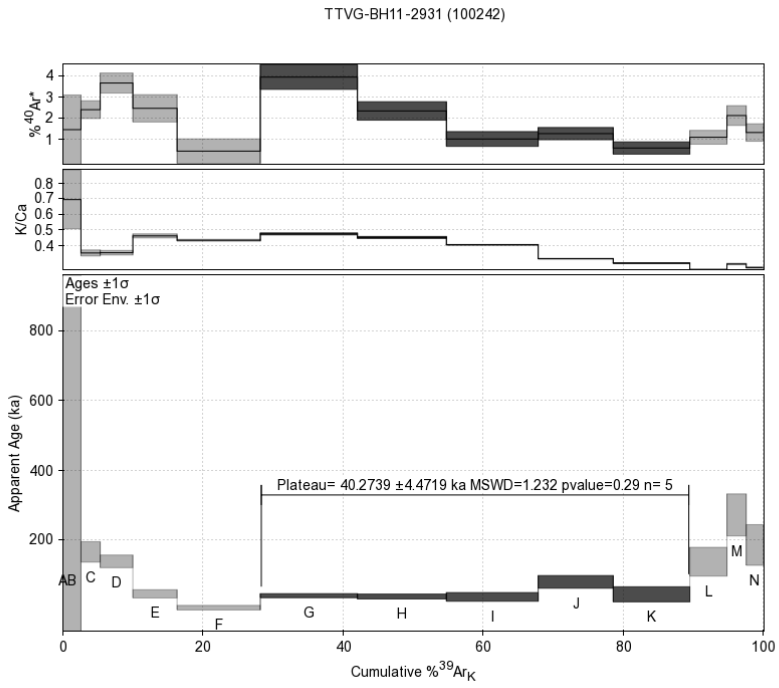

Figure 36: TTVG-BH11-2931 groundmass aliquot 1 age spectrum (initial air).

doi:10.6342/NTU202503882

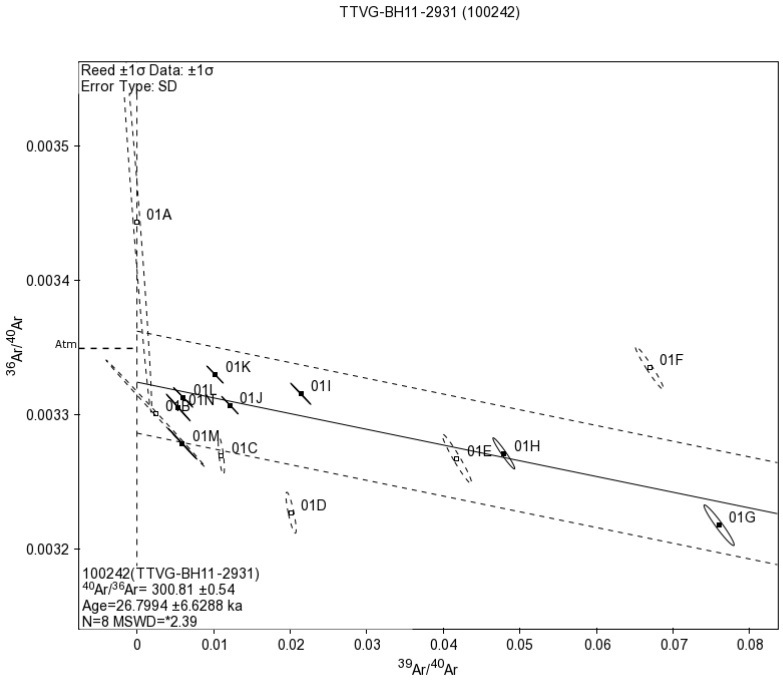

Figure 37: TTVG-BH11-2931 groundmass aliquot 1 isochron (using final steps only).

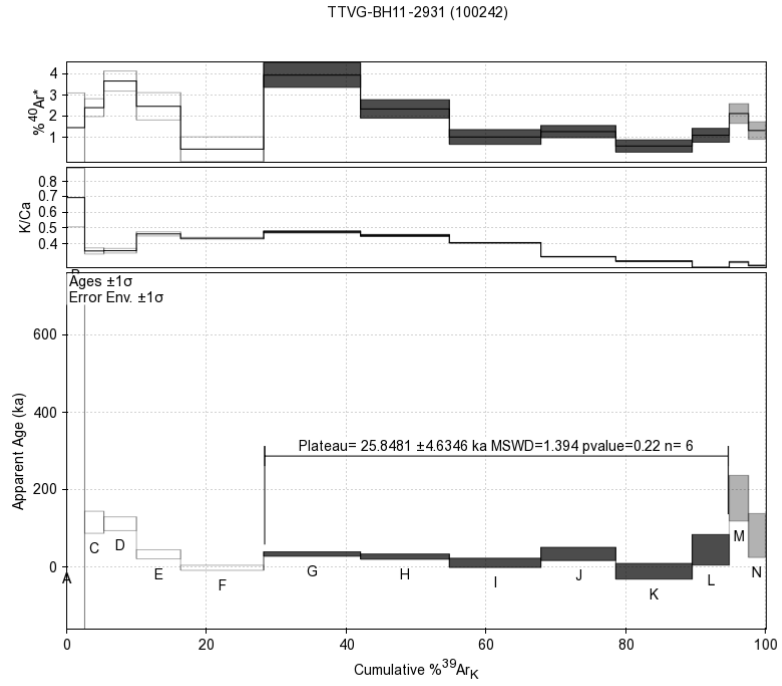

Figure 38: TTVG-BH11-2931 groundmass aliquot 1 age spectrum (trapped initial calculated using final steps only).

doi:10.6342/NTU202503882

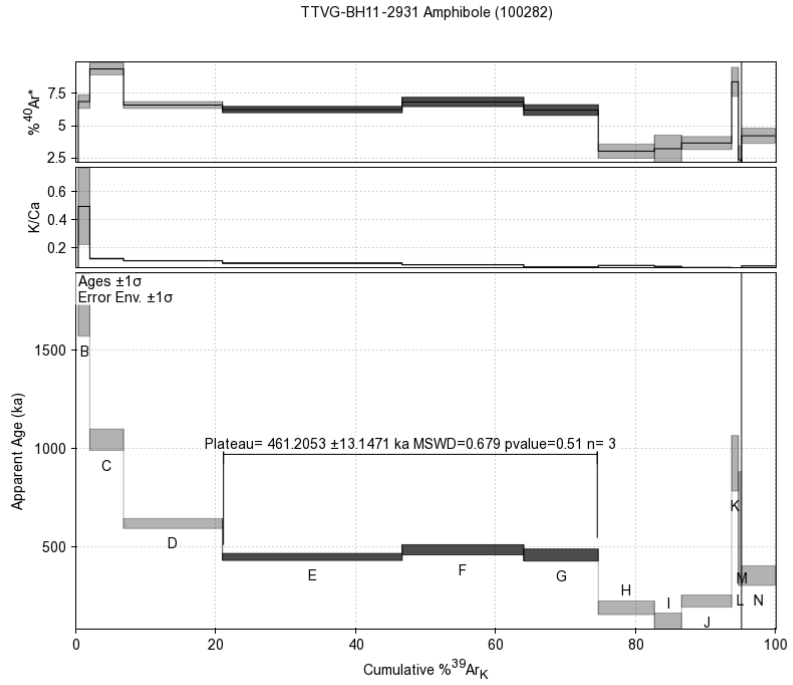

Figure 39: TTVG-BH11-2931 amphibole age spectrum (initial air).

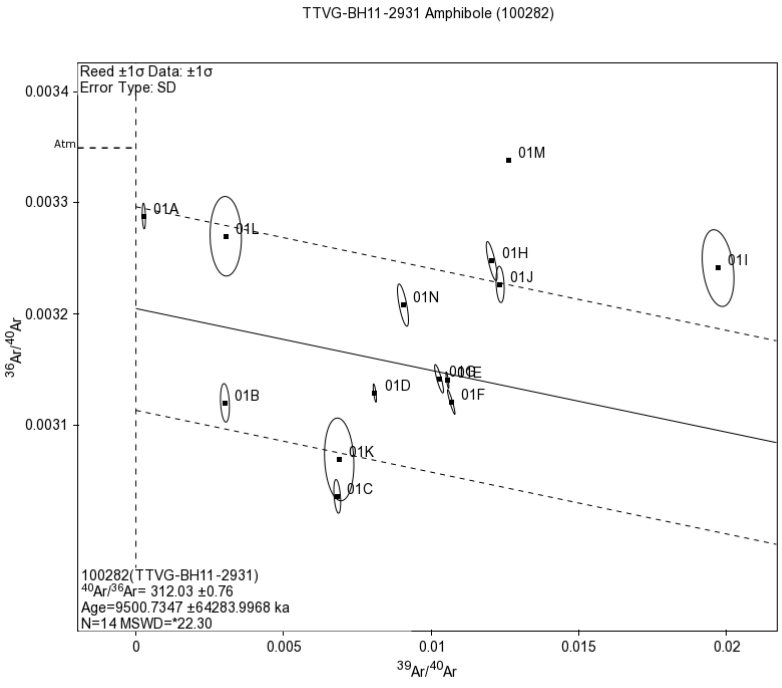

Figure 40: TTVG-BH11-2931 amphibole isochron.

doi:10.6342/NTU202503882

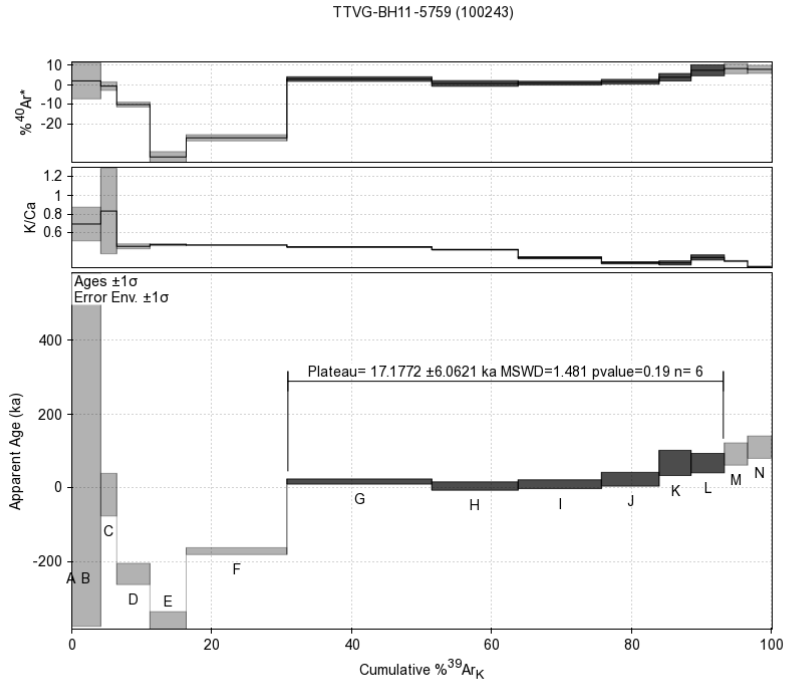

Figure 41: TTVG-BH11-5759 groundmass aliquot 1 age spectrum (initial air).

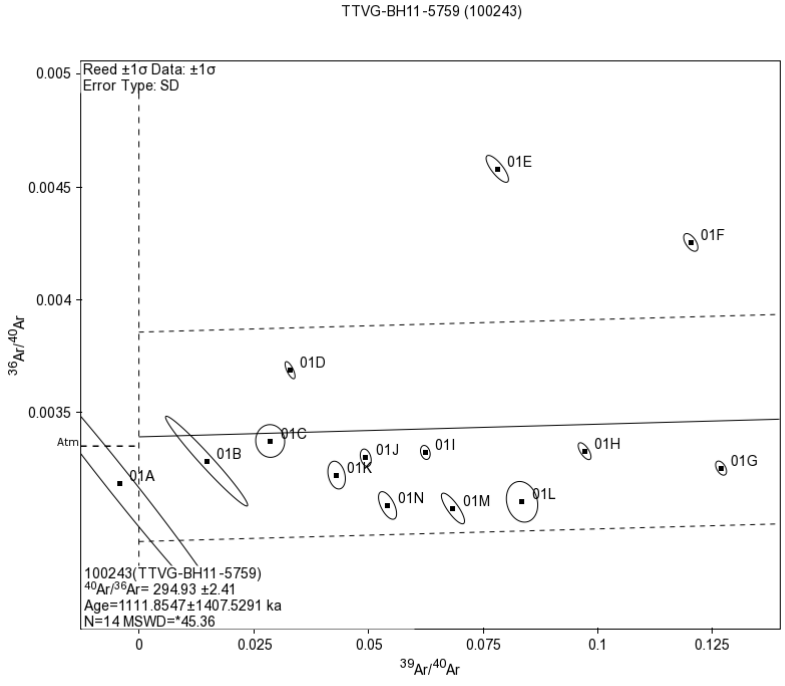

Figure 42: TTVG-BH11-5759 groundmass aliquot 1 isochron.

doi:10.6342/NTU202503882

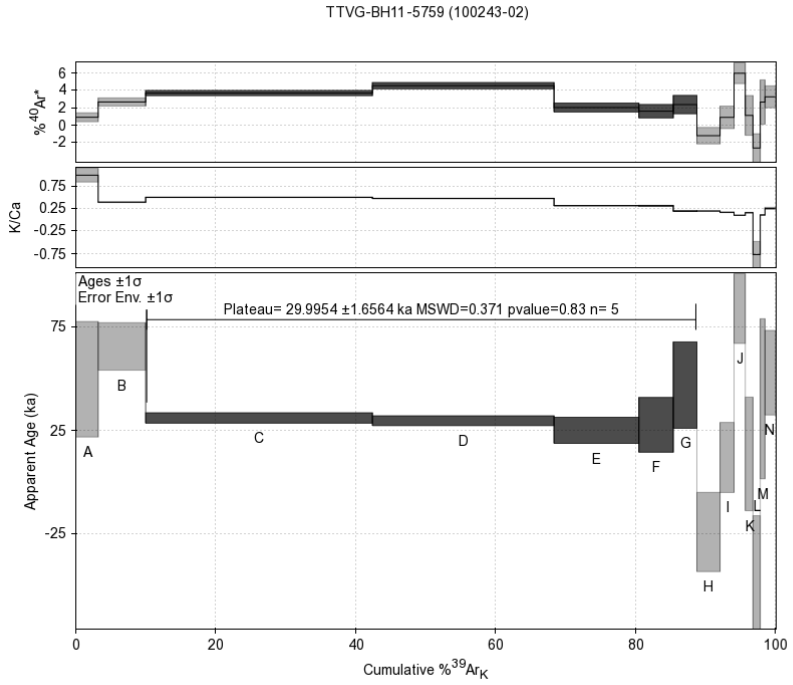

Figure 43: TTVG-BH11-5759 groundmass aliquot 2 age spectrum (initial air).

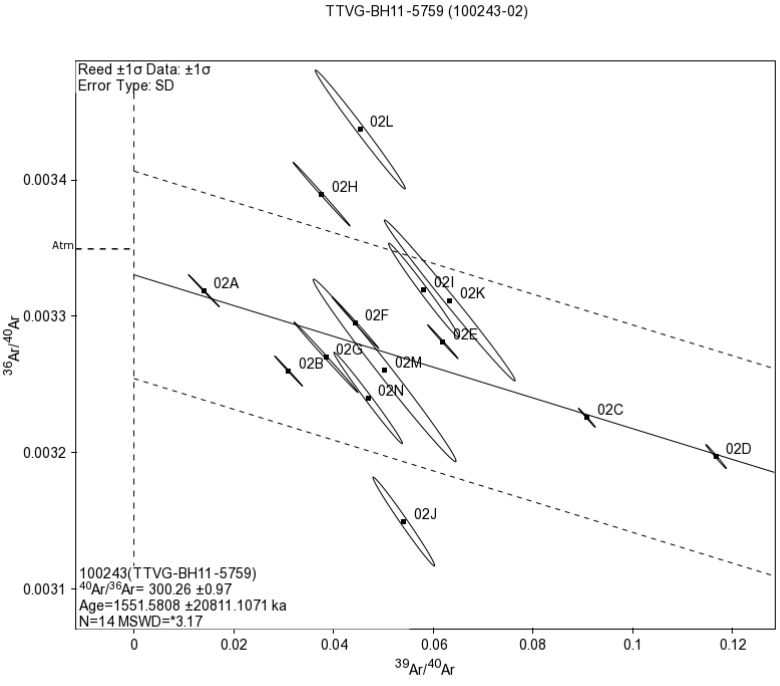

Figure 44: TTVG-BH11-5759 groundmass aliquot 2 isochron.

doi:10.6342/NTU202503882

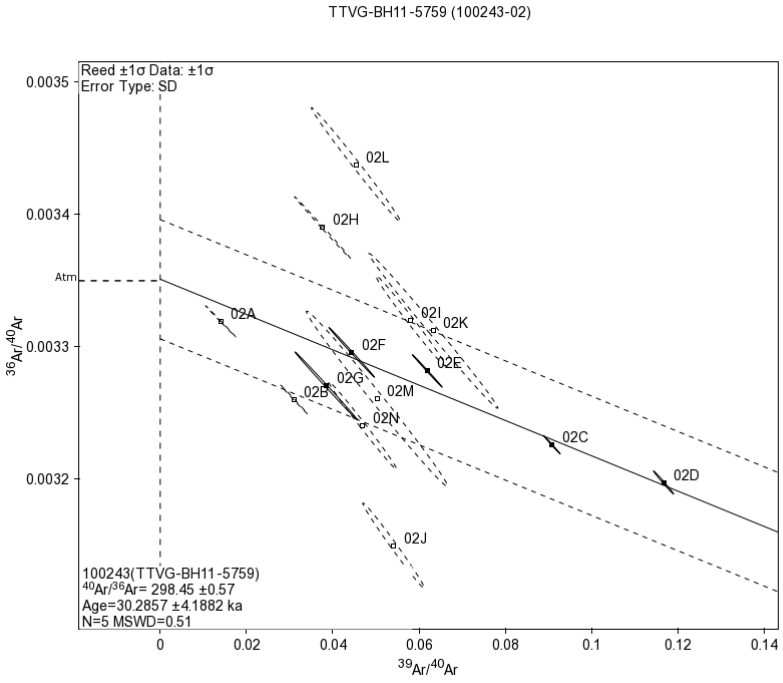

Figure 45: TTVG-BH11-5759 groundmass aliquot 2 isochron (plateau steps only).

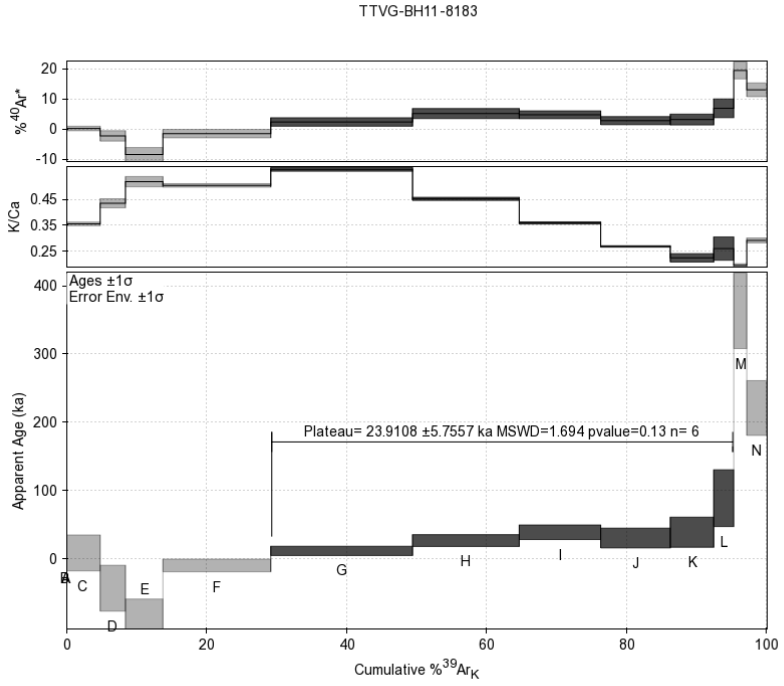

Figure 46: TTVG-BH11-8183 groundmass age spectrum (initial air).

doi:10.6342/NTU202503882

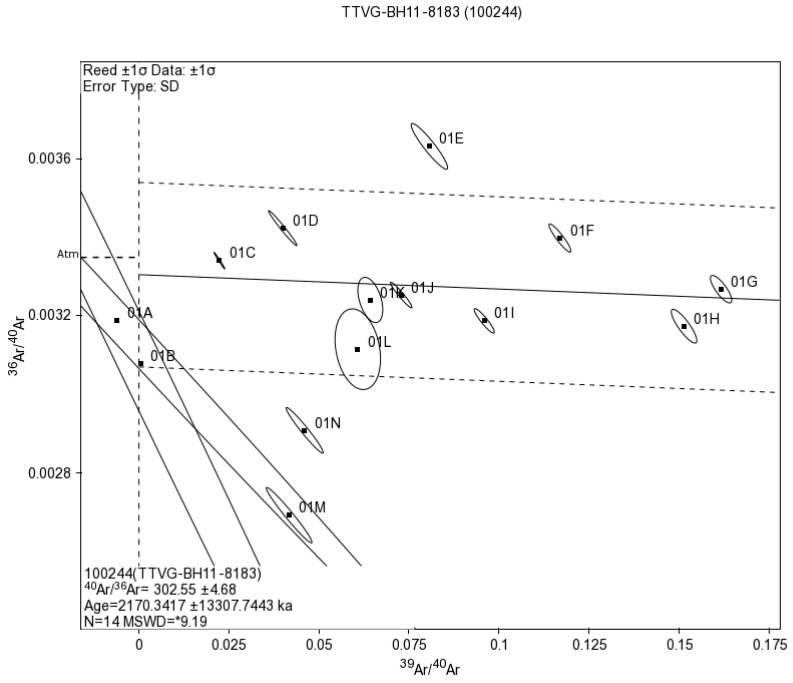

Figure 47: TTVG-BH11-8183 groundmass isochron.

c. TTVG-BH13 Results

All groundmass analyses from borehole TTVG-BH13 were duplicated. While all aliquots yielded results, none produced plateaus when assumed atmospheric initial argon values were applied. Using trapped initial argon values did produce plateaus for both aliquots of TTVG-BH13-3537. Amphibole samples were also analyzed with their groundmass counterpart. With the exception of samples containing multiple components, all samples showed excess argon, except for one aliquot of the TTVG-BH13-7880.

TTVG-BH13-3537 groundmass aliquot 1 exhibited large uncertainties in early steps, with varying $^{39}Ar_K/^{37}Ar_{Ca}$ ratios likely due to minor alteration. The isochron plot, although slightly scattered, yielded an initial $^{40}Ar/^{36}Ar$ of 300.0 ± 0.5 and an isochron age

doi:10.6342/NTU202503882

of 232.7 ± 10.1 ka. A plateau age of 227.8 ± 8.6 ka calculated with the trapped initial value agrees with the isochron age. Aliquot 2 did not yield a plateau with assumed atmospheric values. The beginning and final steps appear to represent different phases, as reflected in the isochron plot. A questionable isochron age of 274.1 ± 5.0 ka and a trapped initial value of 296.1 ± 0.2 were calculated, and a corresponding plateau age of 273.4 ± 1.7 ka was determined. Although, the plateau age and isochron age are in agreement, due to aliquot 2's multiphase nature, the preferred age for the TVG-BH13-3537 is the plateau age of aliquot 1: 227.8 ± 8.6 ka.

The amphibole sample exhibited large uncertainties in the early steps with variable $^{39}Ar_K/^{37}Ar_{Ca}$ ratios attributed to alteration. Despite scatter in the isochron plot, an isochron age of 260.5 ± 35.4 ka and an initial value of 302.9 ± 0.5 were calculated. A plateau age of 289.4 ± 14.6 ka calculated with the inferred initial value is in agreement with the isochron age.

TTVG-BH13-7880 groundmass samples did not yield plateaus, although poorly defined isochron ages and initial value were calculated. Aliquot 1 exhibited large uncertainties in early steps, producing an isochron age of 250.0 ± 9.0 ka and an initial $^{40}Ar/^{36}Ar$ of 298.4 ± 0.7. Aliquot 2 showed uncertainty in both early and final steps, due to low potassium and argon content. An isochron age of 280.1 ± 7.1 ka and an initial value of 293.3 ± 0.2 were calculated. No plateaus could be produced with the calculated initial

doi:10.6342/NTU202503882

value for both aliquots. Due to aliquot 2's multiphase nature, the preferred estimate for TTVG-BH13-7880 groundmass sample is the aliquot 1 isochron age: 250.0 ± 9.0 ka.

The amphibole sample yielded a plateau despite large initial uncertainties. An isochron of limited robustness produced an initial $^{40}Ar/^{36}Ar$ of 304.8 ± 0.9, and a plateau age of 326.5 ± 16.5 ka was calculated using that value.

Based on groundmass results, the sampled lava flows appear to have erupted in quick succession (Figure 87). The maximum of the preferred TVG-BH13-3537 groundmass age, 227.8 ± 8.6 ka, falls within ten thousand years of the minimum of the preferred TTVG-BH13-7880 groundmass age, 250.0 ± 9.0 ka. Amphibole are also closely clustered and are not only older than their groundmass counterparts, but also resemble the ages of groundmass samples with multiple components. This suggests that some components in the multiphase groundmass are derived from the same source as the amphiboles, resulting in weighted mean ages that fall between the groundmass and amphibole values.

doi:10.6342/NTU202503882

Table 9: TTVG-BH13 Ar–Ar Results

Sample	Best Age (ka)	+/- 1σ	Initial $^{40/36}$Ar	+/- 1σ	Age Type
TTVG-BH13-3537 (1)	227.8	8.6	300.0	0.5	plateau age (trapped initial)
TTVG-BH13-3537 (2)	273.4	1.7	296.1	0.2	plateau age (trapped initial)
TTVG-BH13-3537 (Amphibole)	289.4	14.6	302.9	0.5	plateau age (trapped initial)
TTVG-BH13-7880 (1)	250.0	9.0	298.4	0.7	isochron age
TTVG-BH13-7880 (2)	280.1	7.1	293.3	0.2	isochron age
TTVG-BH13-7880 (Amphibole)	326.5	16.5	304.8	0.9	plateau age (trapped initial)

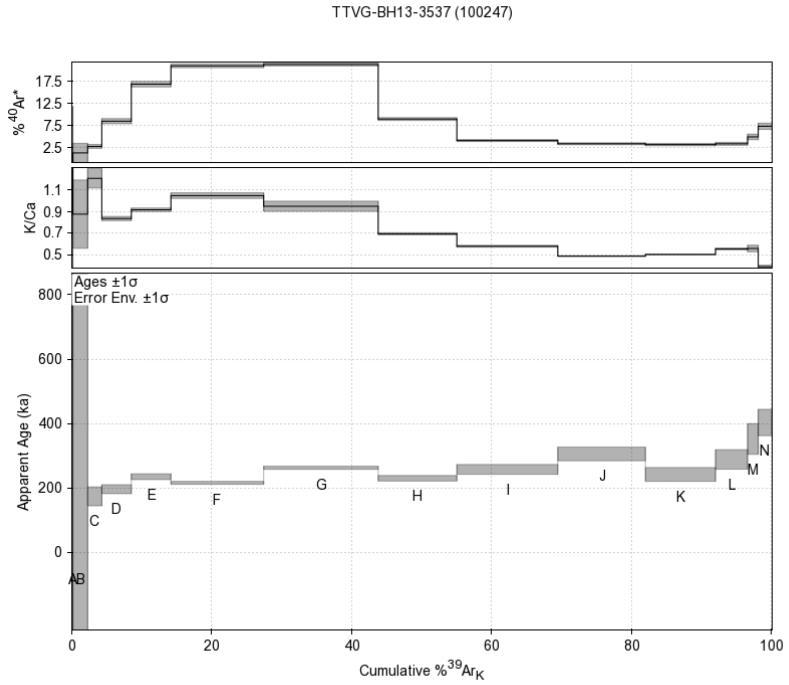

Figure 48: TTVG-BH13-3537 groundmass aliquot 1 age spectrum (initial air).

doi:10.6342/NTU202503882

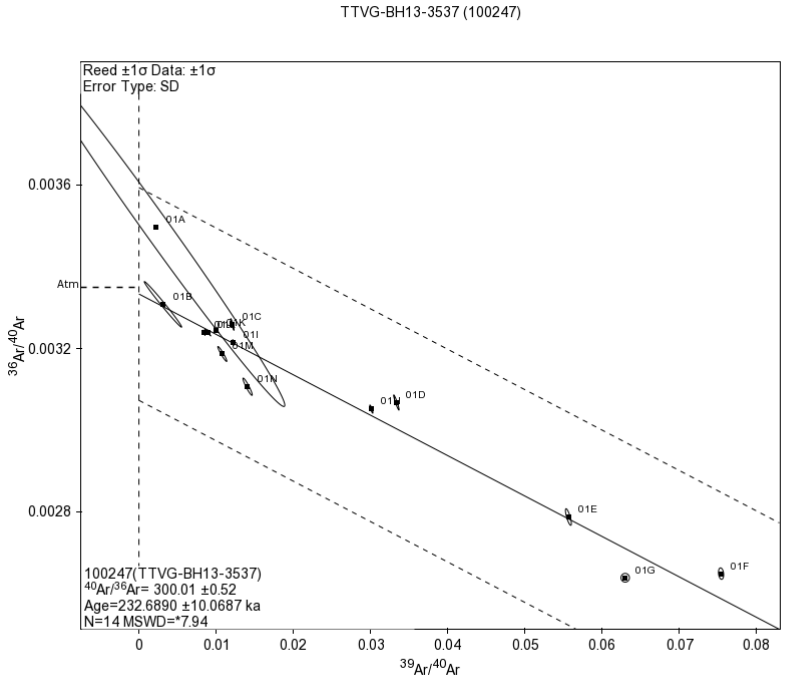

Figure 49: TTVG- BH13-3537 groundmass aliquot 1 isochron.

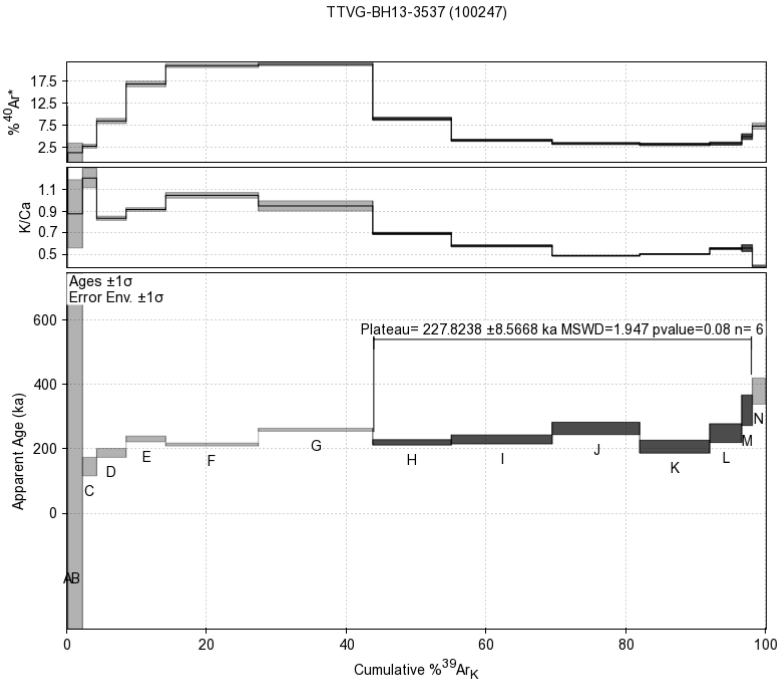

Figure 50: TTVG- BH13-3537 groundmass aliquot 1 age spectrum (trapped initial).

doi:10.6342/NTU202503882

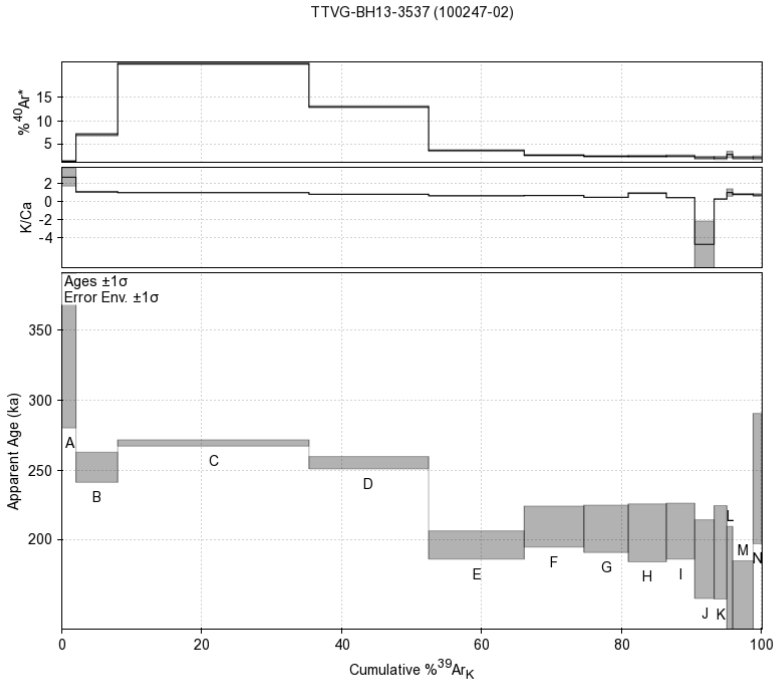

Figure 51: TTVG-BH13-3537 groundmass aliquot 2 age spectrum (initial air).

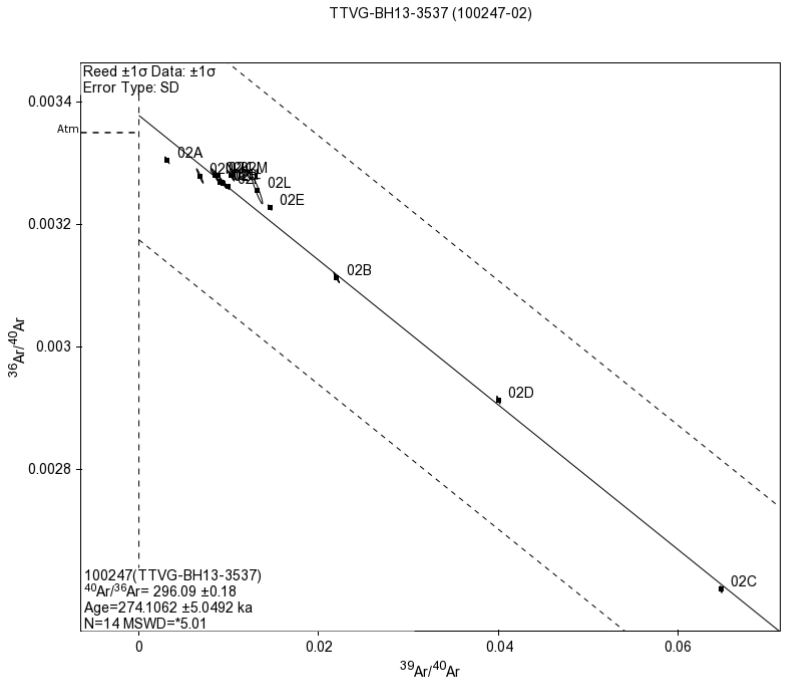

Figure 52: TTVG- BH13-3537 groundmass aliquot 2 isochron.

doi:10.6342/NTU202503882

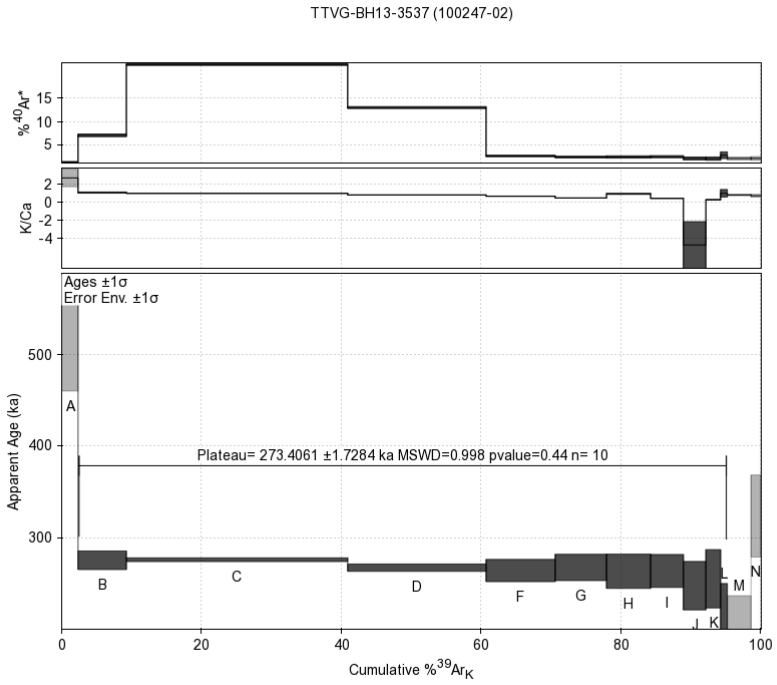

Figure 53: TTVG- BH13-3537 groundmass aliquot 2 age spectrum (trapped initial and with anomalous E step removed).

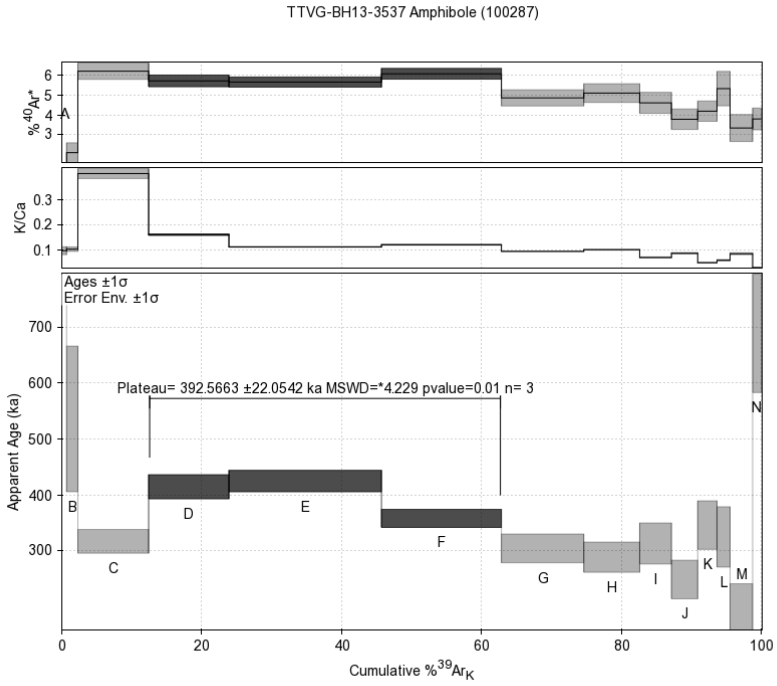

Figure 54: TTVG-BH13-3537 amphibole age spectrum (initial air).

doi:10.6342/NTU202503882

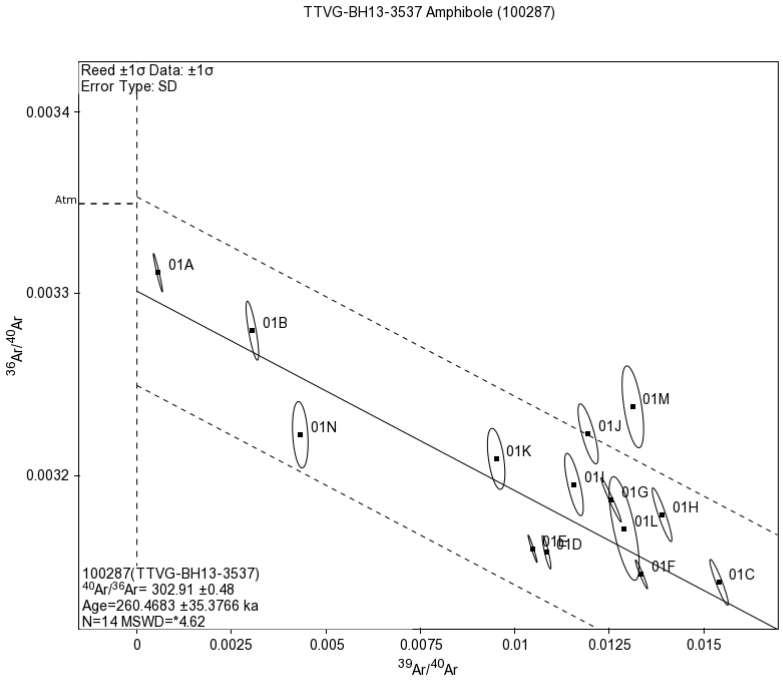

Figure 55: TTVG- BH13-3537 amphibole isochron.

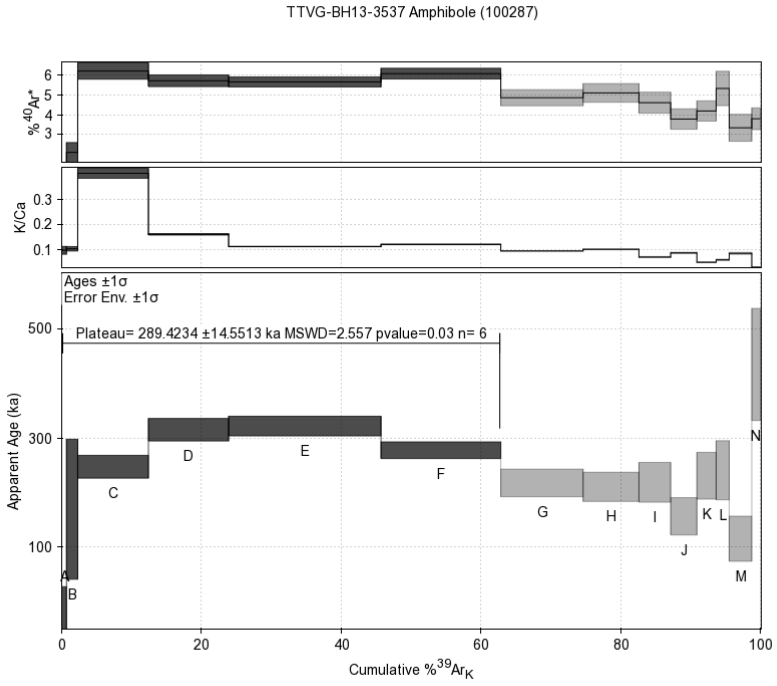

Figure 56: TTVG- BH13-3537 amphibole age spectrum (trapped initial).

doi:10.6342/NTU202503882

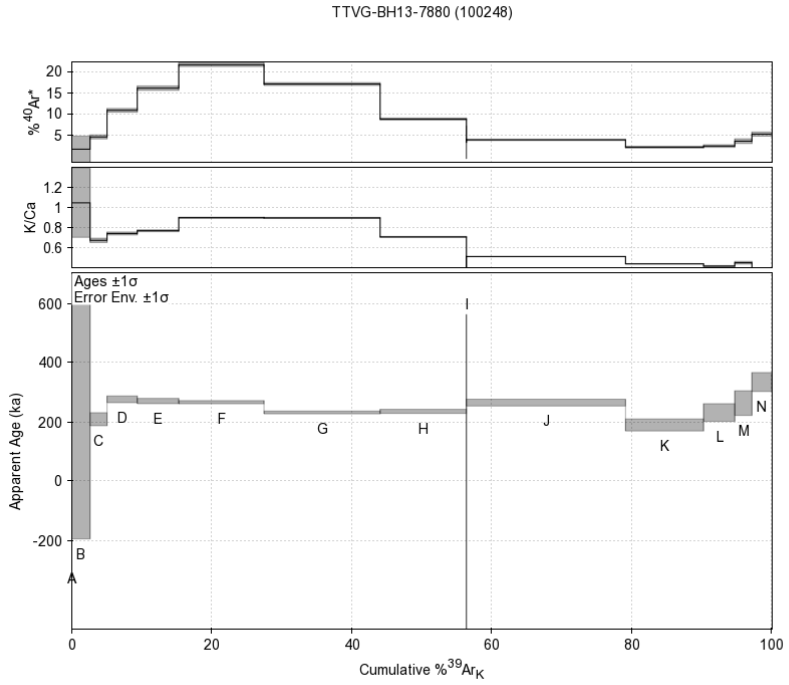

Figure 57: TTVG-BH13-7880 groundmass aliquot 1 age spectrum (initial air).

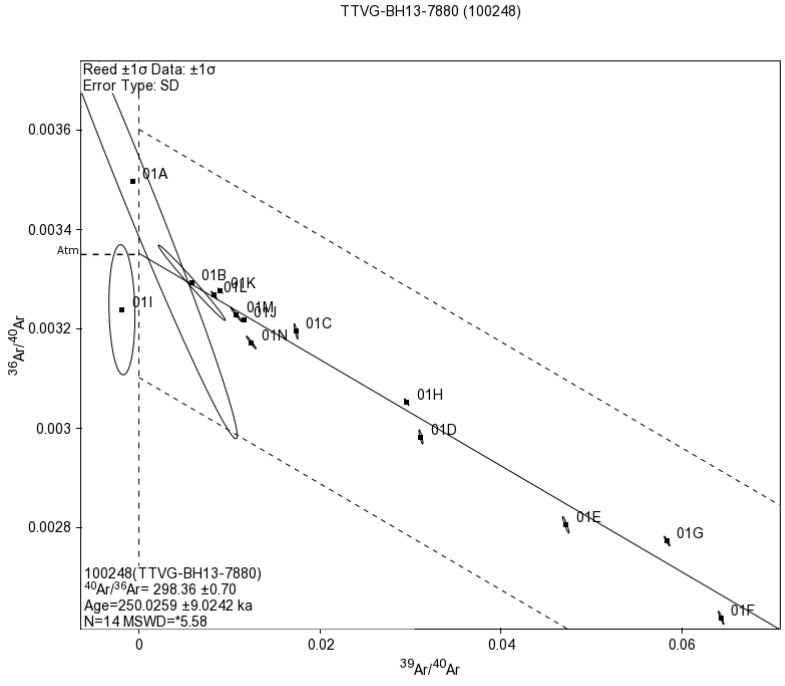

Figure 58: TTVG- BH13-7880 groundmass aliquot 1 isochron.

doi:10.6342/NTU202503882

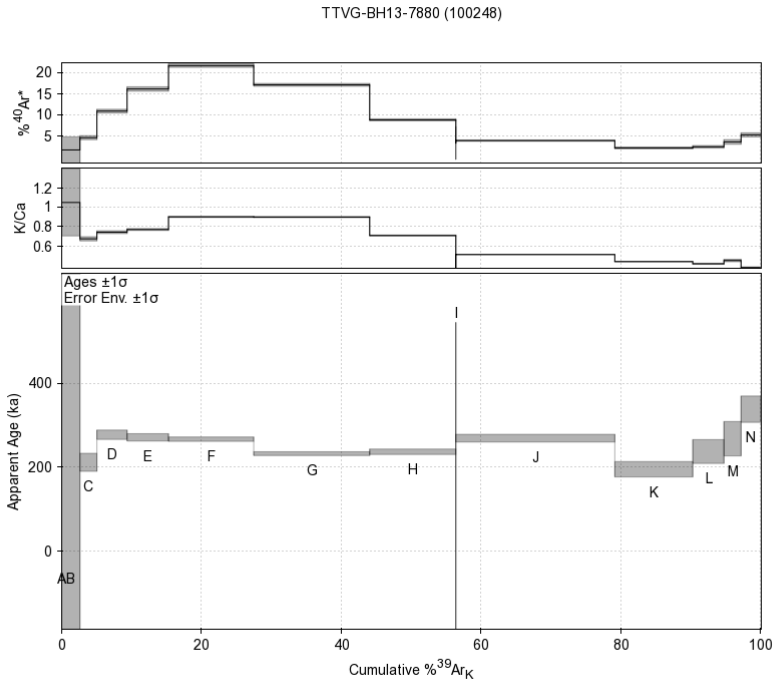

Figure 59: TTVG-BH13-7880 groundmass aliquot 1 age spectrum (trapped initial).

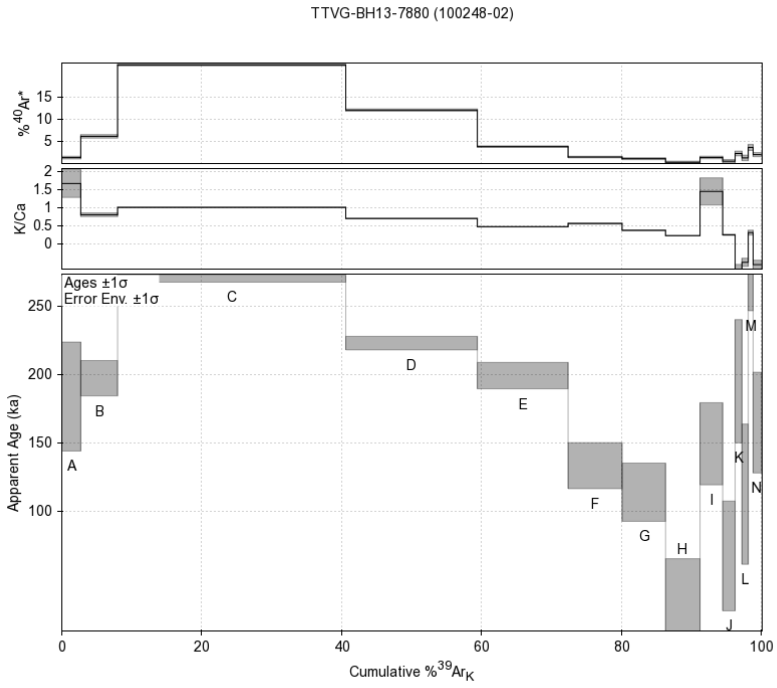

Figure 60: TTVG-BH13-7880 groundmass aliquot 2 age spectrum (initial air).

doi:10.6342/NTU202503882

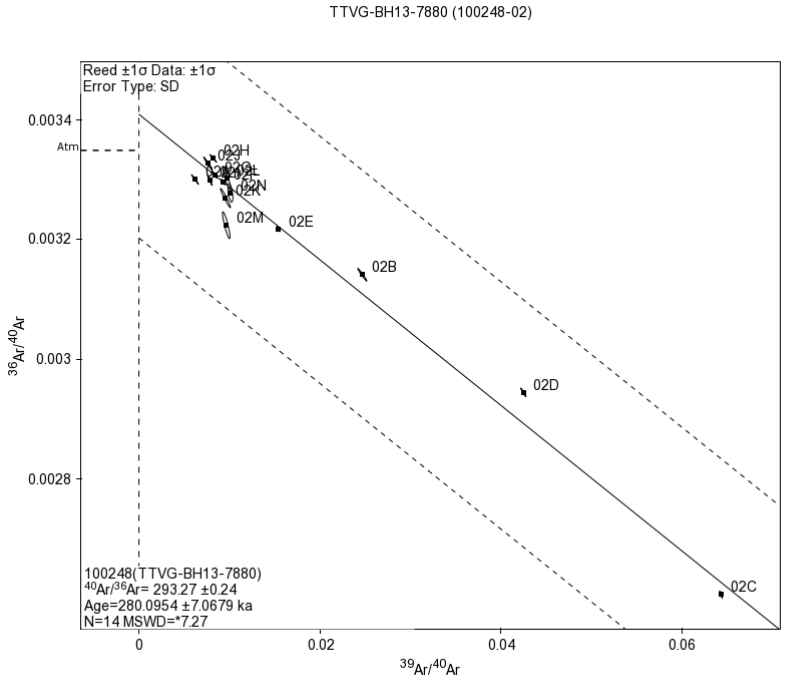

Figure 61: TTVG- BH13-7880 groundmass aliquot 2 isochron.

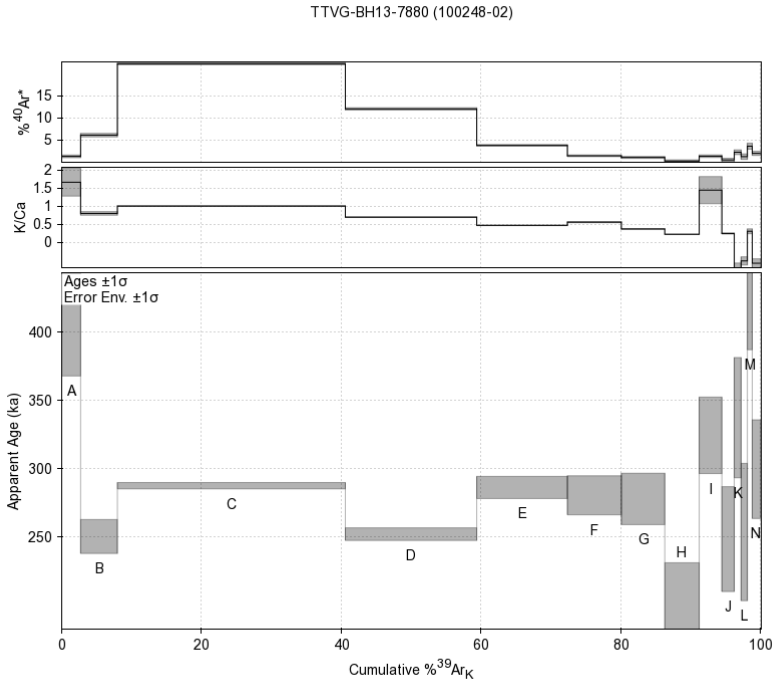

Figure 62: TTVG-BH13-7880 groundmass aliquot 2 age spectrum (trapped initial).

doi:10.6342/NTU202503882

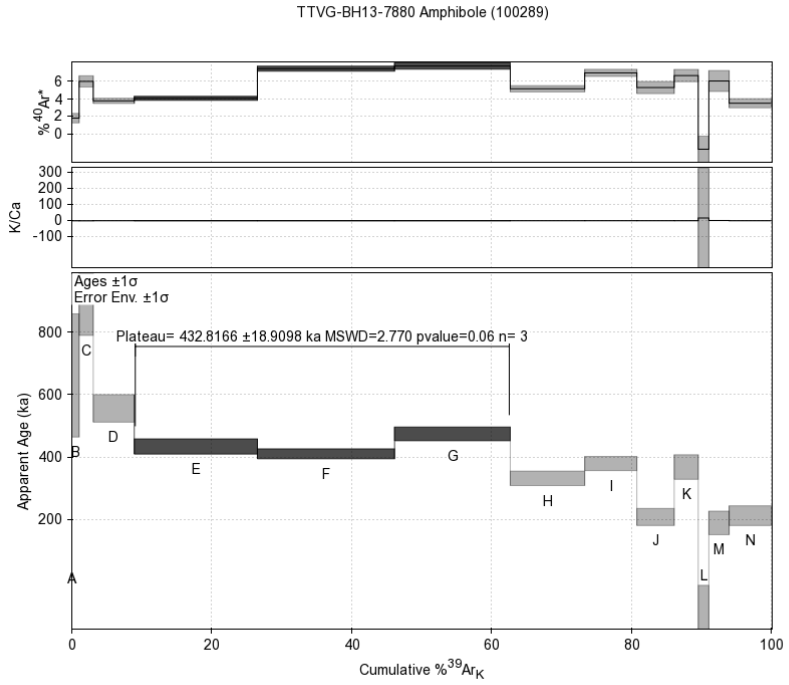

Figure 63: TTVG-BH13-7880 amphibole age spectrum (initial air).

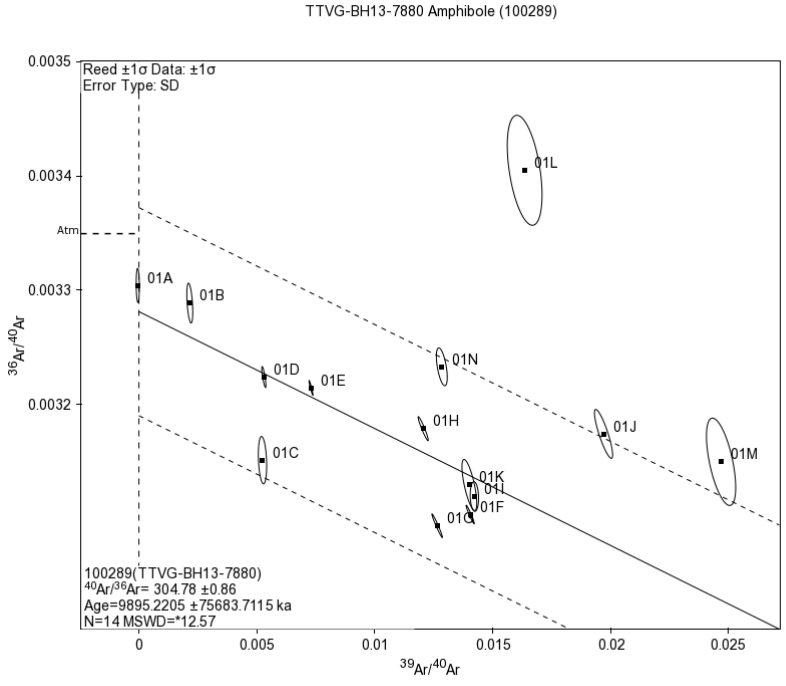

Figure 64: TTVG- BH13-7880 amphibole isochron.

doi:10.6342/NTU202503882

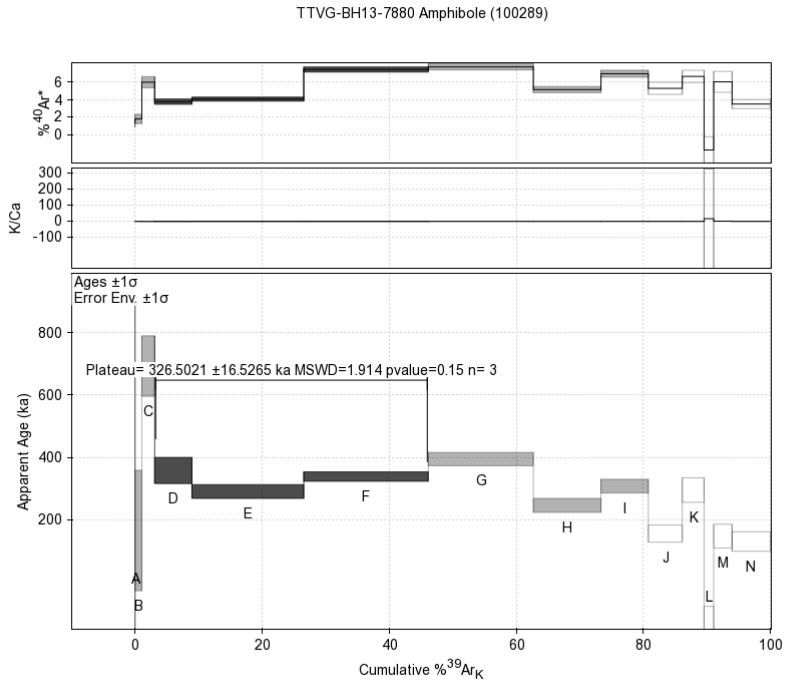

Figure 65: TTVG-BH13-7880 amphibole age spectrum (trapped air and without low argon steps).

d. TTVG-BH08 Results

All TTVG-BH08 groundmass samples showed large uncertainties at low temperature steps, associated with elevated $^{39}Ar_K/^{37}Ar_{Ca}$ ratios attributed to minor alterations. Apparent ages decreased with increasing temperature for unclear reasons. Aside from a sample with multiple components, the isochrons were well-behaved and consistent with plateau ages calculated using trapped initial values, most of which are near atmospheric values. Thus, plateau ages are the preferred estimates.

TTVG-BH08-1820 groundmass produced a plateau encompassing all steps, despite uncertainties at low-temperature steps. A robust isochron yielded an age of 165.4 ± 1.8 ka and an initial $^{40}Ar/^{36}Ar$ value of 296.5 ± 0.3. A plateau age of 165.4 ± 3.7 ka was calculated.

doi:10.6342/NTU202503882

TTVG-BH08-5355 groundmass showed large uncertainties in the beginning steps with varying $^{39}Ar_K/^{37}Ar_{Ca}$ ratios attributed to minor alterations, but produced a reliable isochron age of 153.1 ± 1.7 ka and an initial value of 295.4 ± 0.4. A plateau age of 151.8 ± 2.5 ka was calculated.

TTVG-BH08-8284 groundmass clearly exhibited multiple components with different ages and initial compositions. An initial value of 294.5 ± 1.4 was derived from the isochron, and was then used for trapped initial argon correction on a plateau defined by 40% of the gas (instead of the typically required 50%) to gain an estimated age of 333 -5/+50 ka.

All three samples come from different lava flows separated by breccia or abrupt lithological changes (Figure 87). TTVG-BH08-1820 and TTVG-BH08-5355 groundmass ages do not follow stratigraphic order, possibly due to uncertain initial value determination. At this age range, assumed initial values significantly affect age estimates. As seen in the results of TTVG-BH08-1820, using assumed initial value of 298.56 instead of the trapped initial value of 296.5 ± 0.3 shifts the age by several thousand years (see Appendix). The TTVG-BH08-1820 sample also incorporates low temperature steps associated with minor alterations that have greater apparent age. Despite these issues, the similar ages suggest rapid emplacement of andesites around 0.16 Ma, following a highly

doi:10.6342/NTU202503882

altered lava flow unsuitable for Ar – Ar dating. TTVG-BH08-8284, from the borehole's base, represents an earlier eruptive event.

Table 10: TTVG-BH08 Ar–Ar Results

Sample	**Best Age (ka)**	+/- 1σ	**Initial$^{40/36}$Ar**	+/- 1σ	**Age Type**
TTVG-BH08-1820	165.4	3.7	296.5	0.3	plateau age (trapped initial)
TTVG-BH08-5355	151.8	2.5	295.4	0.4	plateau age (trapped initial)
TTVG-BH08-8284	*333.0*	*-5/+50*	*294.5*	*1.4*	

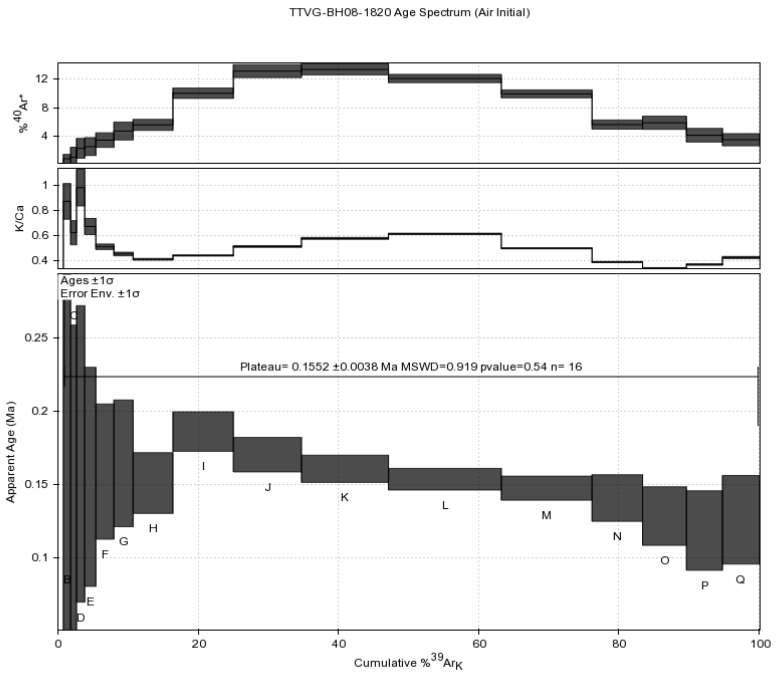

Figure 66: TTVG-BH08-1820 groundmass age spectrum (initial air).

doi:10.6342/NTU202503882

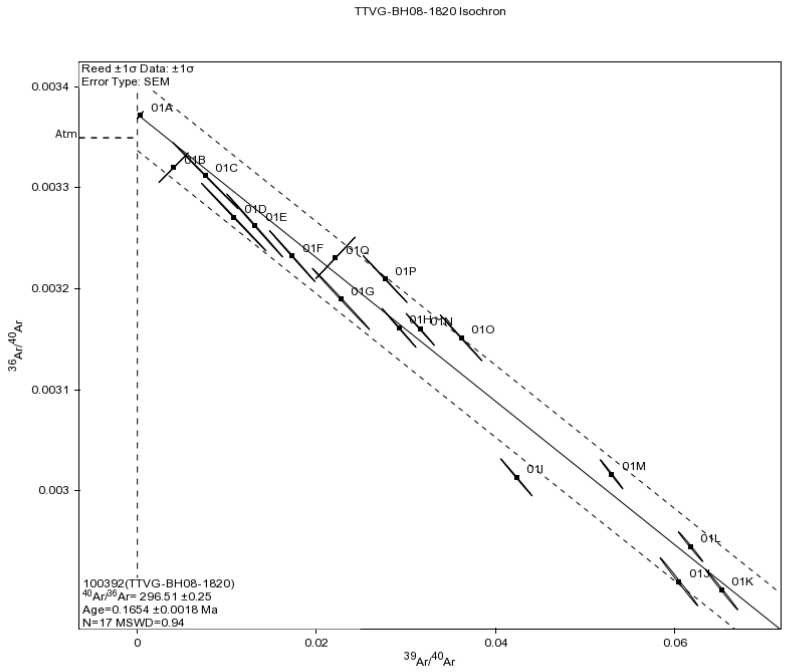

Figure 67: TTVG-BH08-1820 groundmass isochron.

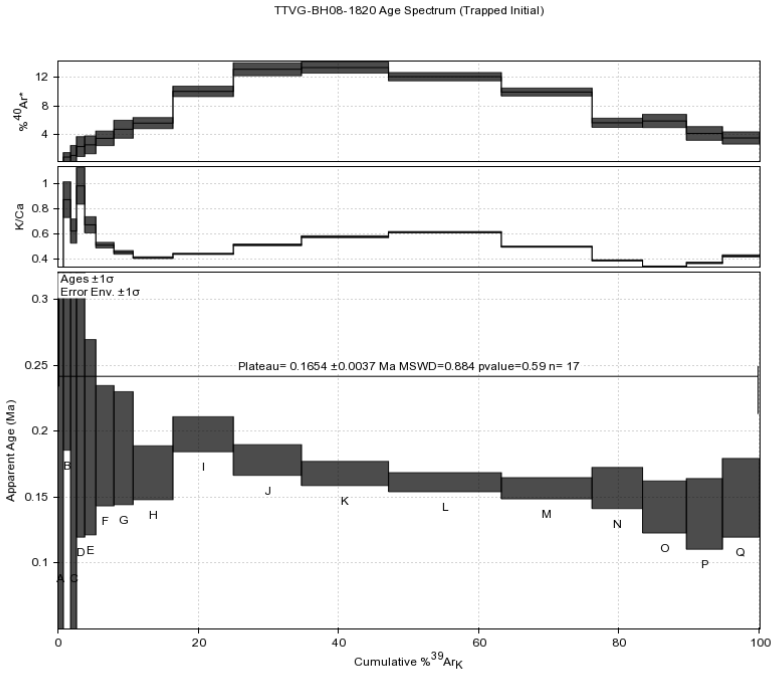

Figure 68: TTVG-BH08-1820 groundmass age spectrum (trapped air).

doi:10.6342/NTU202503882

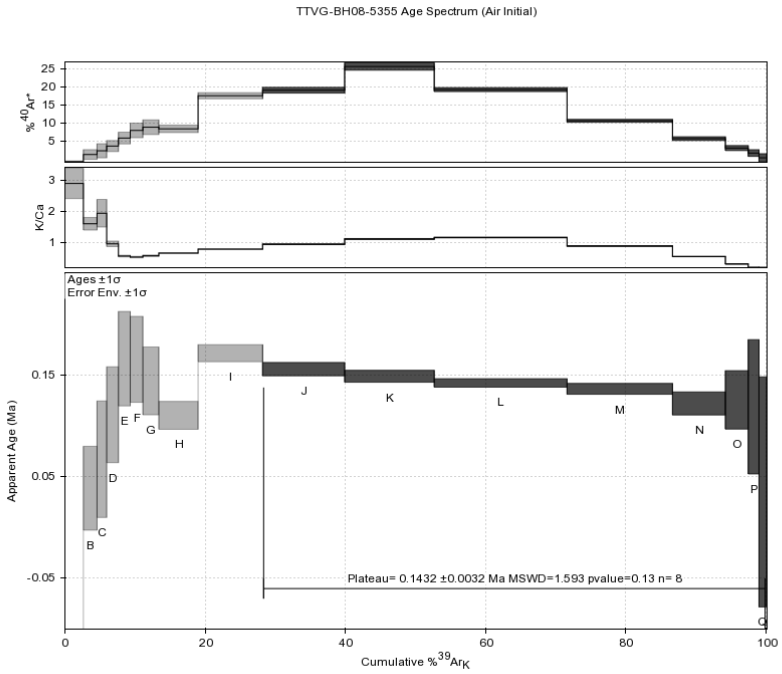

Figure 69: TTVG-BH08-5355 groundmass age spectrum (initial air).

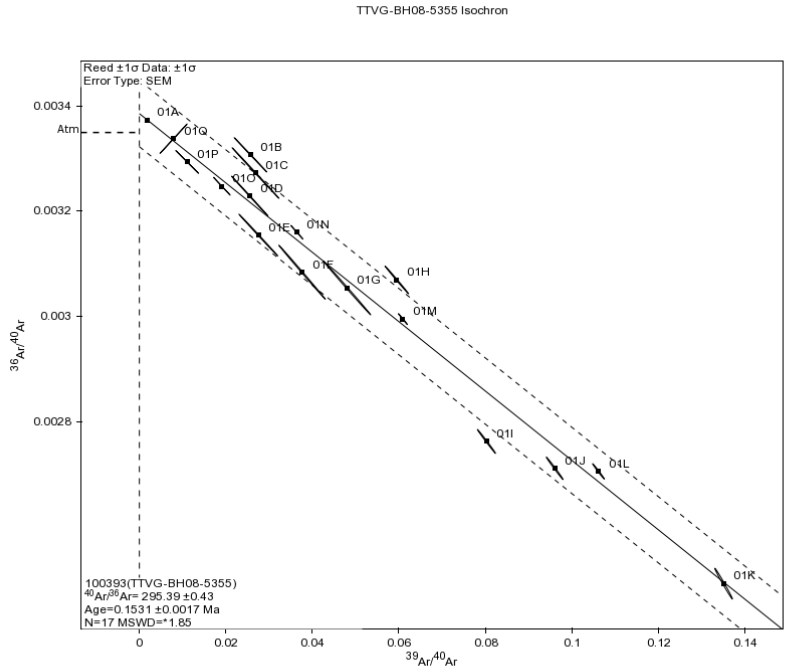

Figure 70: TTVG-BH08-5355 groundmass isochron.

doi:10.6342/NTU202503882

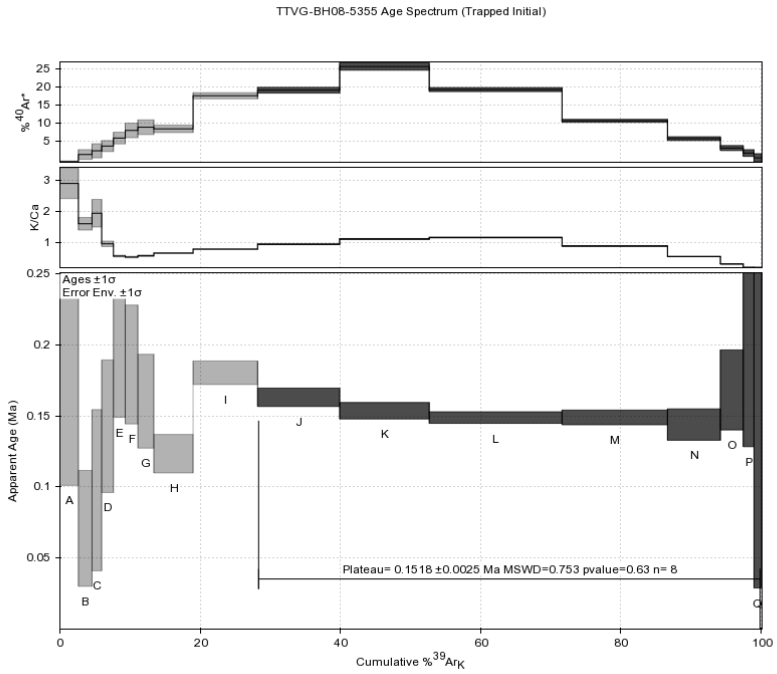

Figure 71: TTVG-BH08-5355 groundmass age spectrum (trapped air).

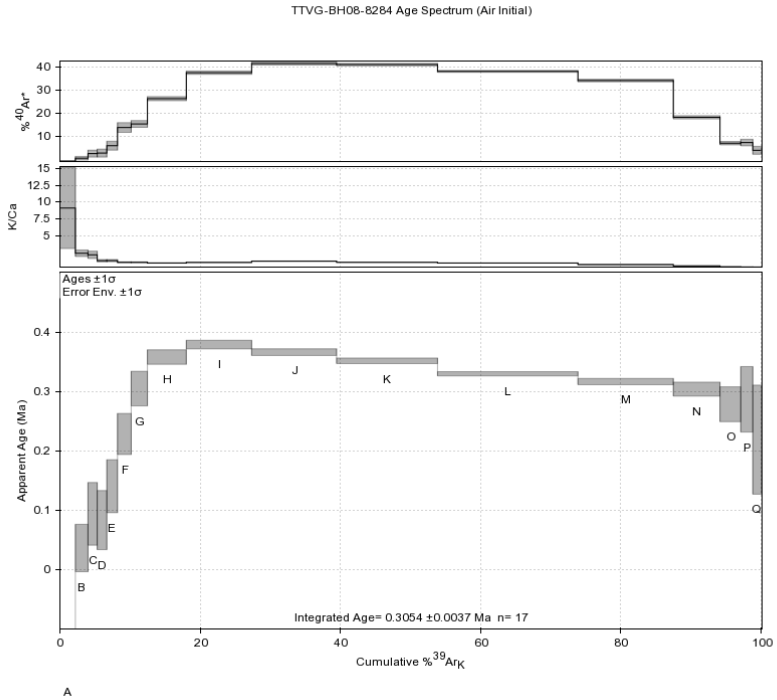

Figure 72: TTVG-BH08-8284 groundmass age spectrum (initial air).

doi:10.6342/NTU202503882

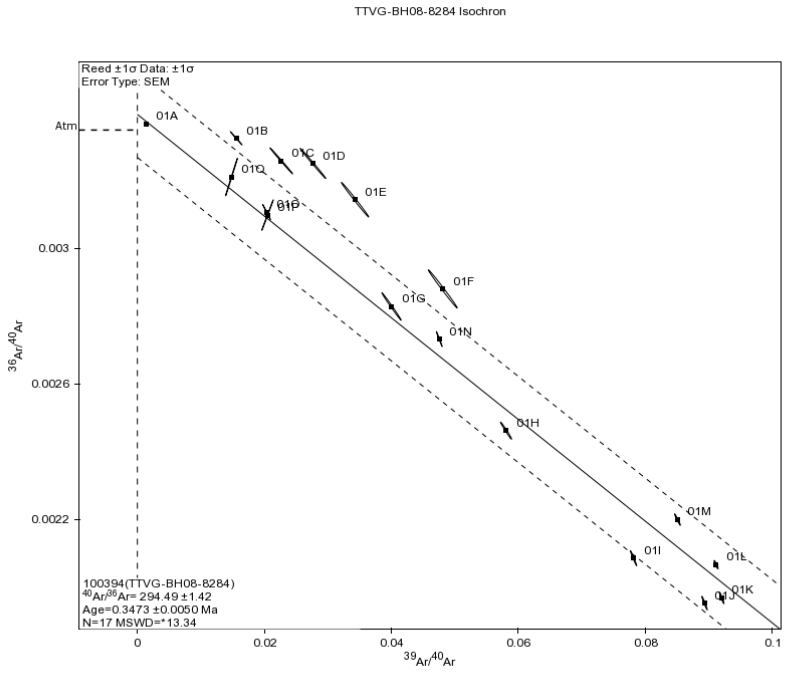

Figure 73: TTVG-BH08-8284 groundmass isochron.

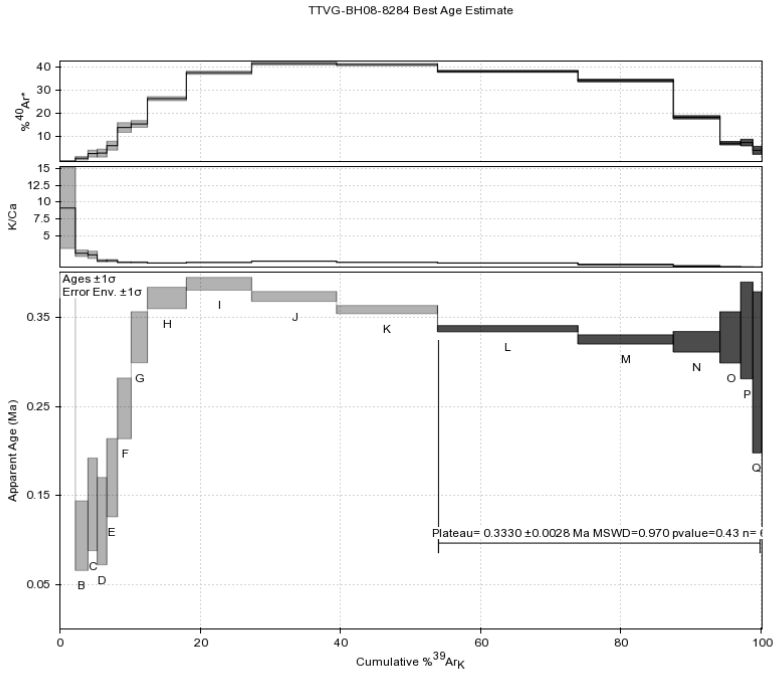

Figure 74: TTVG-BH08-8284 groundmass age spectrum (best estimated age).

e. TTVG-BH01 Results

The TTVG-BH01 groundmass samples also showed large uncertainties at low-

doi:10.6342/NTU202503882

temperature steps that correlate with elevated $^{39}Ar_K/^{37}Ar_{Ca}$ ratios linked to minor alterations. Excluding one sample with multiple components, isochrons were generally well-behaved and aligned with plateau ages corrected for trapped initial values, most of which were close to atmospheric or indicated slight excess argon.

TTVG- BH01-7071 groundmass showed large uncertainties at low-temperature steps with varying $^{39}Ar_K/^{37}Ar_{Ca}$ ratios attributed to alterations, but yielded an isochron age of 289.7 ± 11.6 ka and an initial value of 295.4 ± 3.8. Its plateau age of 308.3 ± 5.8 ka is in agreement with the isochron age and preferred.

TTVG-BH01-9697 groundmass incorporates all steps into its plateau, despite large uncertainties in beginning steps. It yielded a robust isochron age of 305.9 ± 2.5 ka and an initial value of 302.2 ± 0.2. Its plateau age of 305.9 ± 4.2 ka is in agreement with the isochron age and is the preferred estimate.

The TTVG-BH01-134135 groundmass sample showed mixed age and composition components, and its isochron was based on fewer than 50% of the gas release. The calculated initial value of 299.7 ± 0.7 is derived from an isochron composed of the last few steps (less than 50% of the total gas) that produced a plateau, leading to an estimated plateau age of 291 -10/+30 ka from those same few steps.

TTVG-BH01-153154 groundmass showed large uncertainties and variable $^{39}Ar_K/^{37}Ar_{Ca}$ ratios in the beginning steps but a robust isochron yielded an age of 342.3 ±

doi:10.6342/NTU202503882

2.7 ka and an initial value of 297.9 ± 0.5. The plateau age of 328.2 ± 4.4 ka is slightly younger than the isochron age and is the preferred estimate.

These results suggest that TTVG- BH01-7071 and TTVG-BH01-9697 represent two lava flows emplaced around 0.3 Ma. TTVG-BH01-1134135 and TTVG-BH01-153154 belong to an older unit, with TTVG-BH01-153154 age suggesting it formed approximately 20 ka earlier than the overlying flows (Figure 87).

Table 11: TTVG-BH01 Ar–Ar Results

Sample	**Best Age (ka)**	+/- 1σ	**Initial$^{40/36}$Ar**	+/- 1σ	**Age Type**
TTVG-BH01-7071	308.3	5.8	295.4	3.8	plateau age (trapped initial)
TTVG-BH01-9697	305.9	4.2	302.2	0.2	plateau age (trapped initial)
TTVG-BH01-134135	*291.0*	*-10/+30*	*299.7*	*0.7*	
TTVG-BH01-153154	328.2	4.4	297.9	0.5	plateau age (trapped initial)

doi:10.6342/NTU202503882

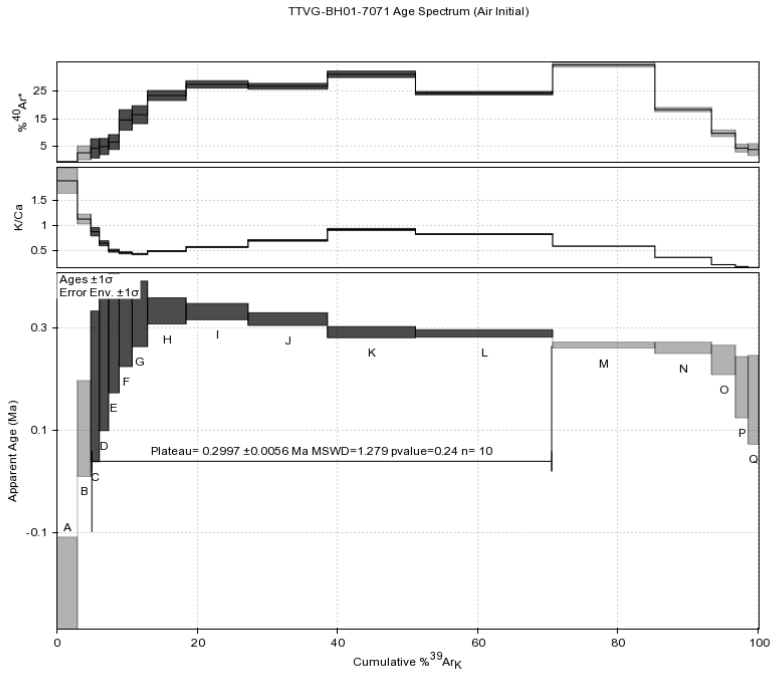

Figure 75: TTVG-BH01-7071 groundmass age spectrum (initial air).

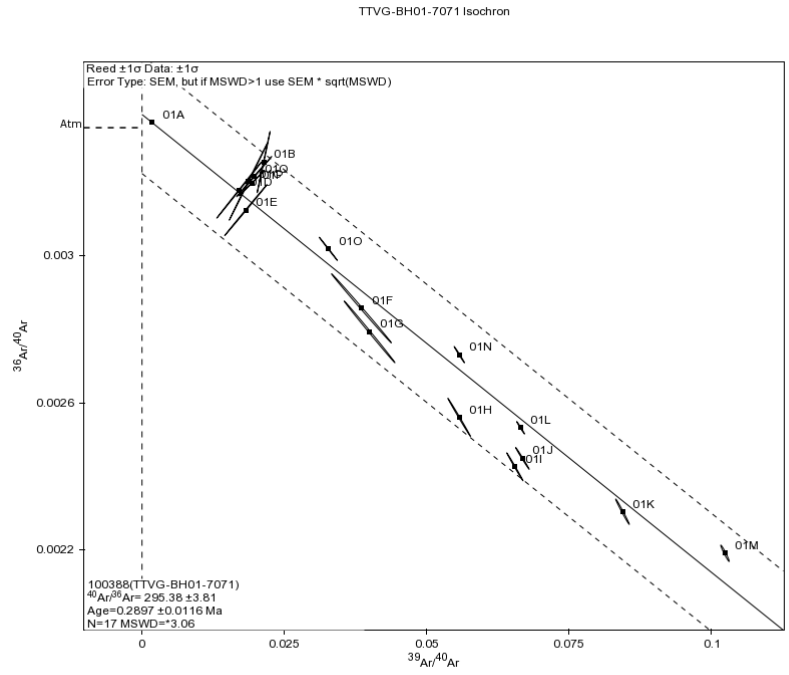

Figure 76: TTVG-BH01-7071 groundmass isochron.

doi:10.6342/NTU202503882

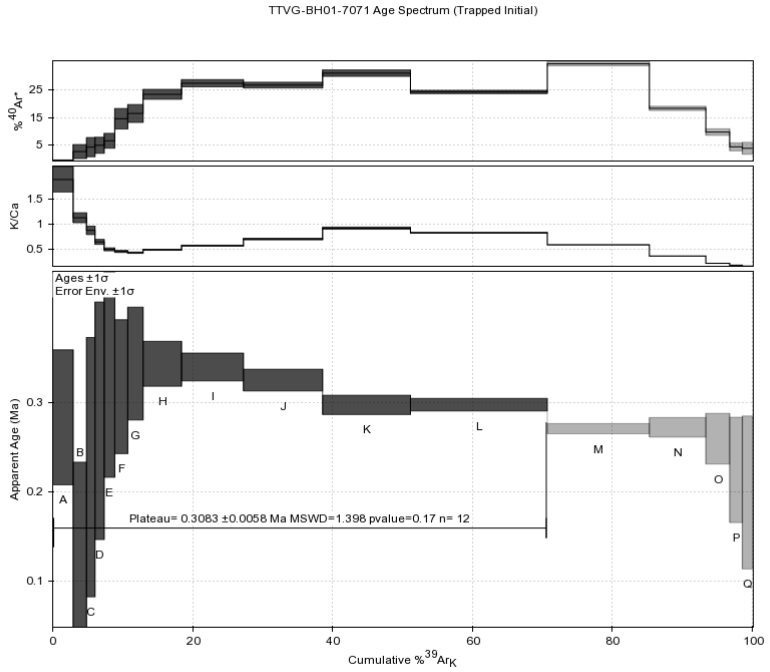

Figure 77: TTVG-BH01-7071 groundmass age spectrum (trapped air).

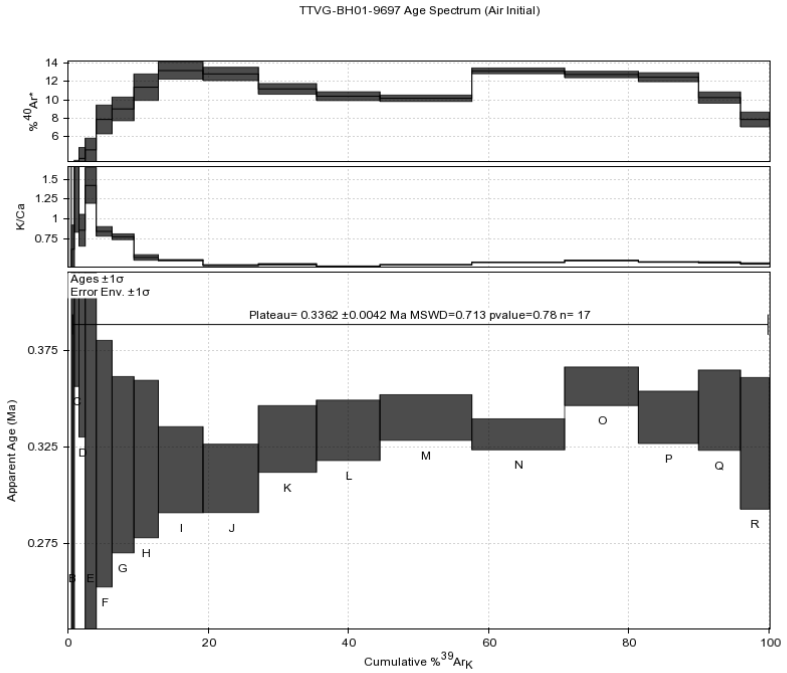

Figure 78: TTVG-BH01-9697 groundmass age spectrum (initial air).

doi:10.6342/NTU202503882

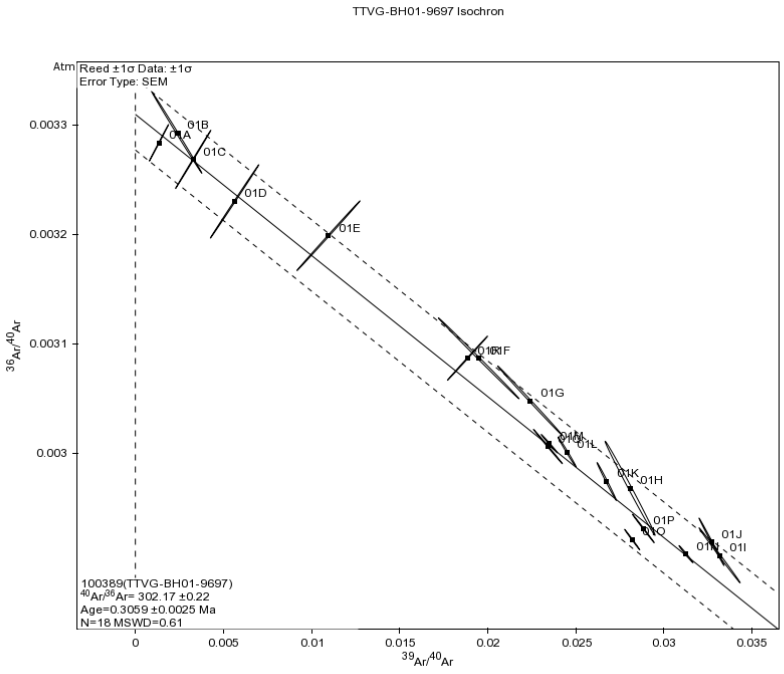

Figure 79: TTVG-BH01-9697 groundmass isochron.

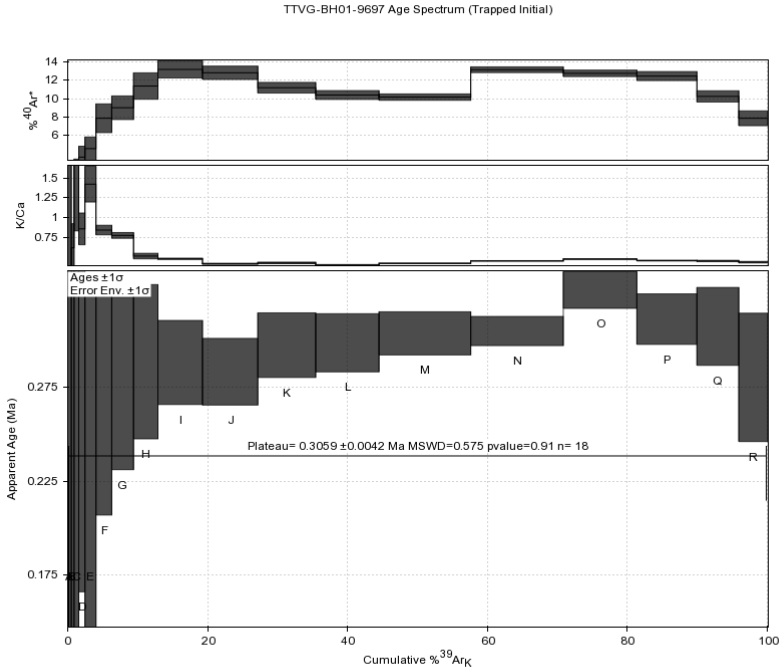

Figure 80: TTVG-BH01-9697 groundmass age spectrum (trapped air).

doi:10.6342/NTU202503882

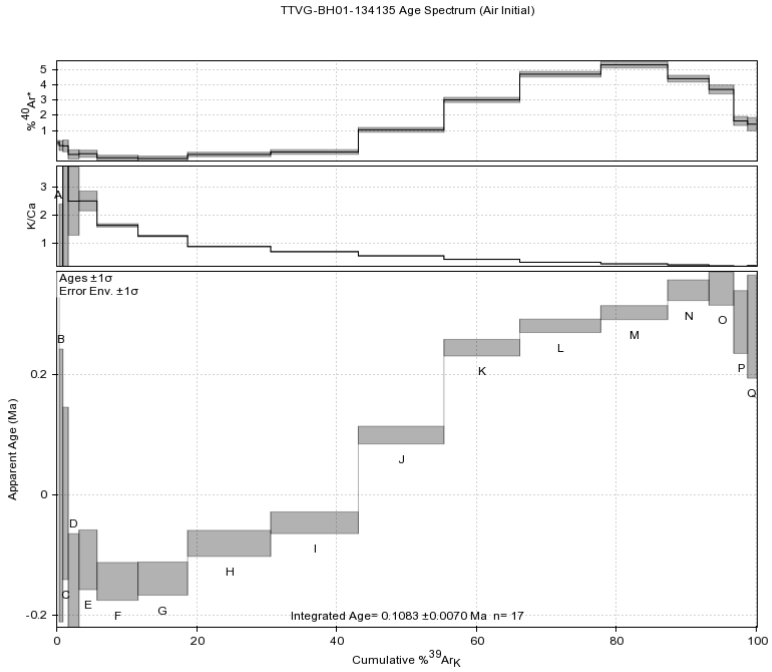

Figure 81: TTVG-BH01-134135 groundmass age spectrum (initial air).

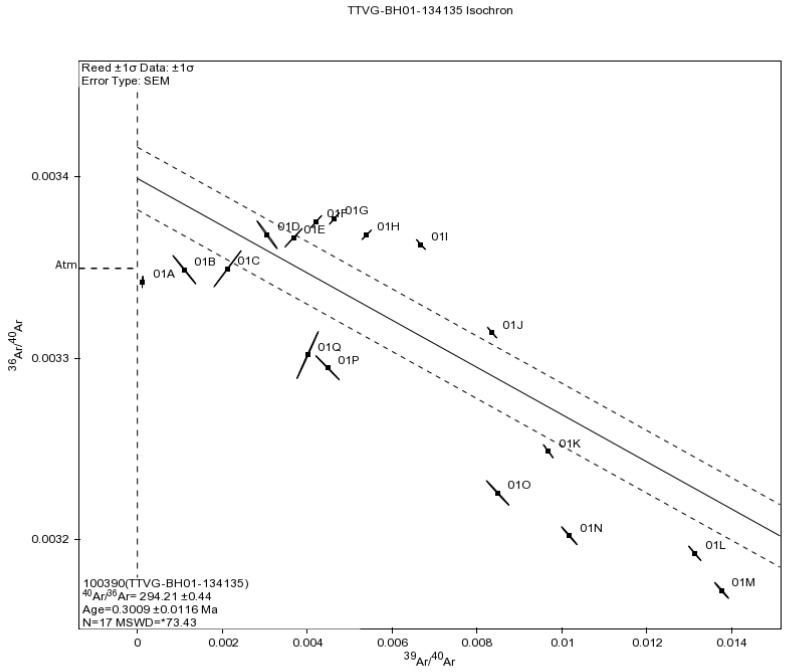

Figure 82: TTVG-BH01-134135 groundmass isochron.

doi:10.6342/NTU202503882

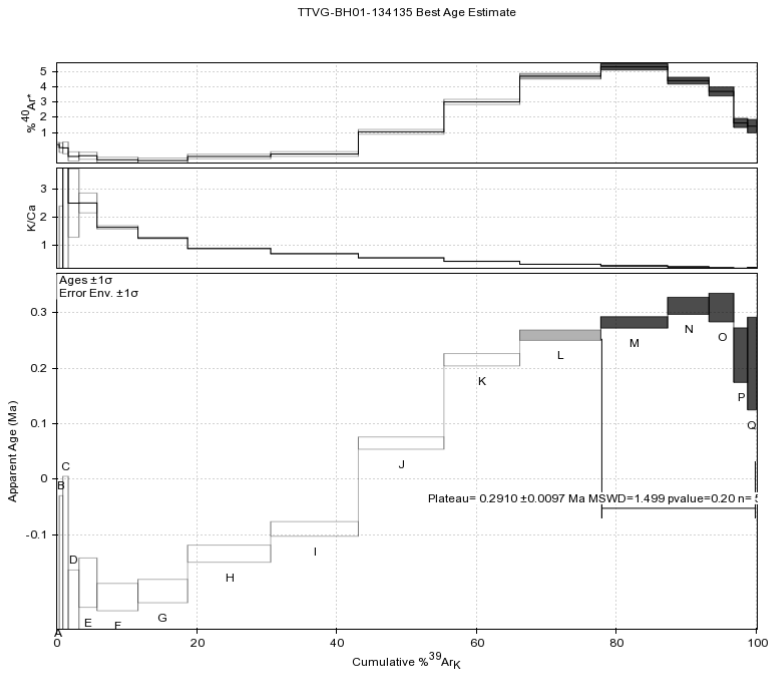

Figure 83: TTVG-BH01-134135 groundmass age spectrum (best estimated age).

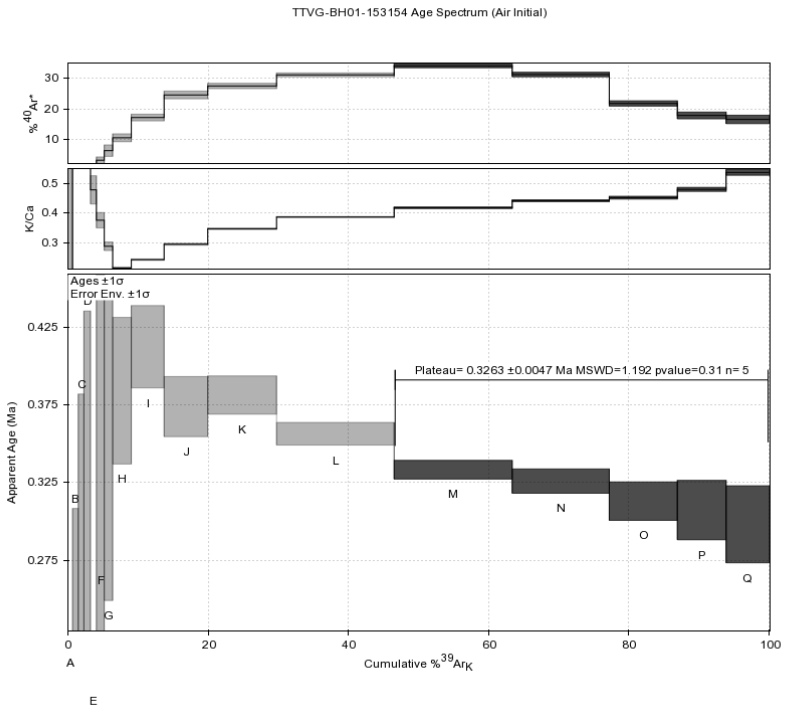

Figure 84: TTVG-BH01-153154 groundmass age spectrum (initial air).

doi:10.6342/NTU202503882

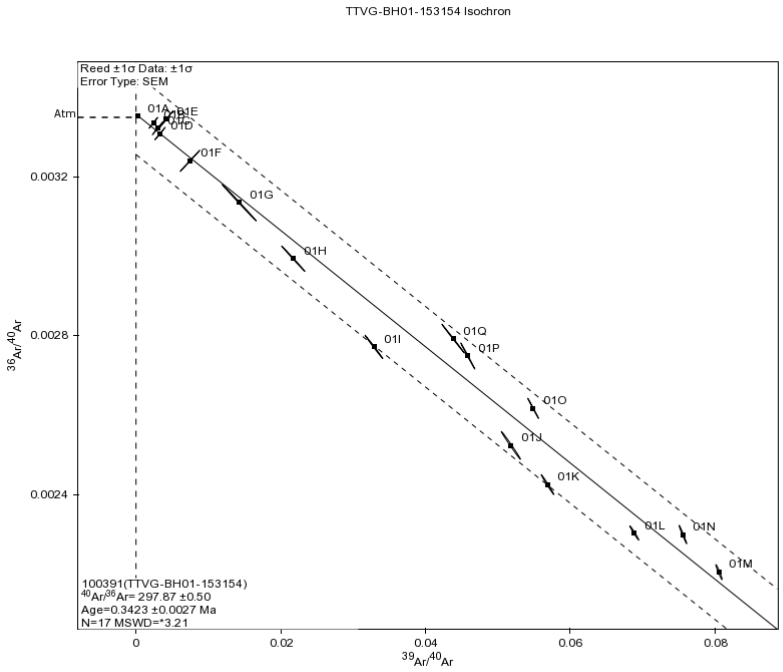

Figure 85: TTVG-BH01-153154 groundmass isochron.

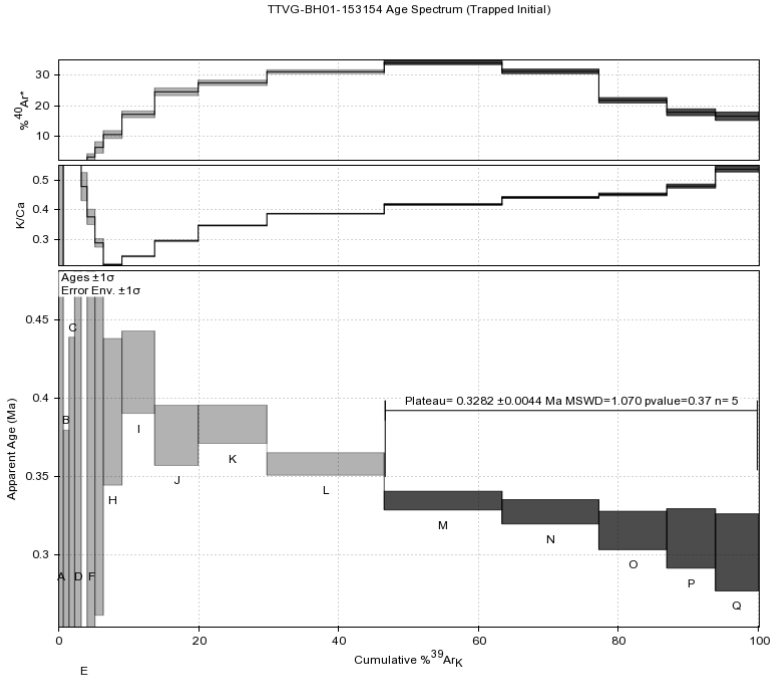

Figure 86: TTVG-BH01-153154 groundmass age spectrum (trapped air).

doi:10.6342/NTU202503882

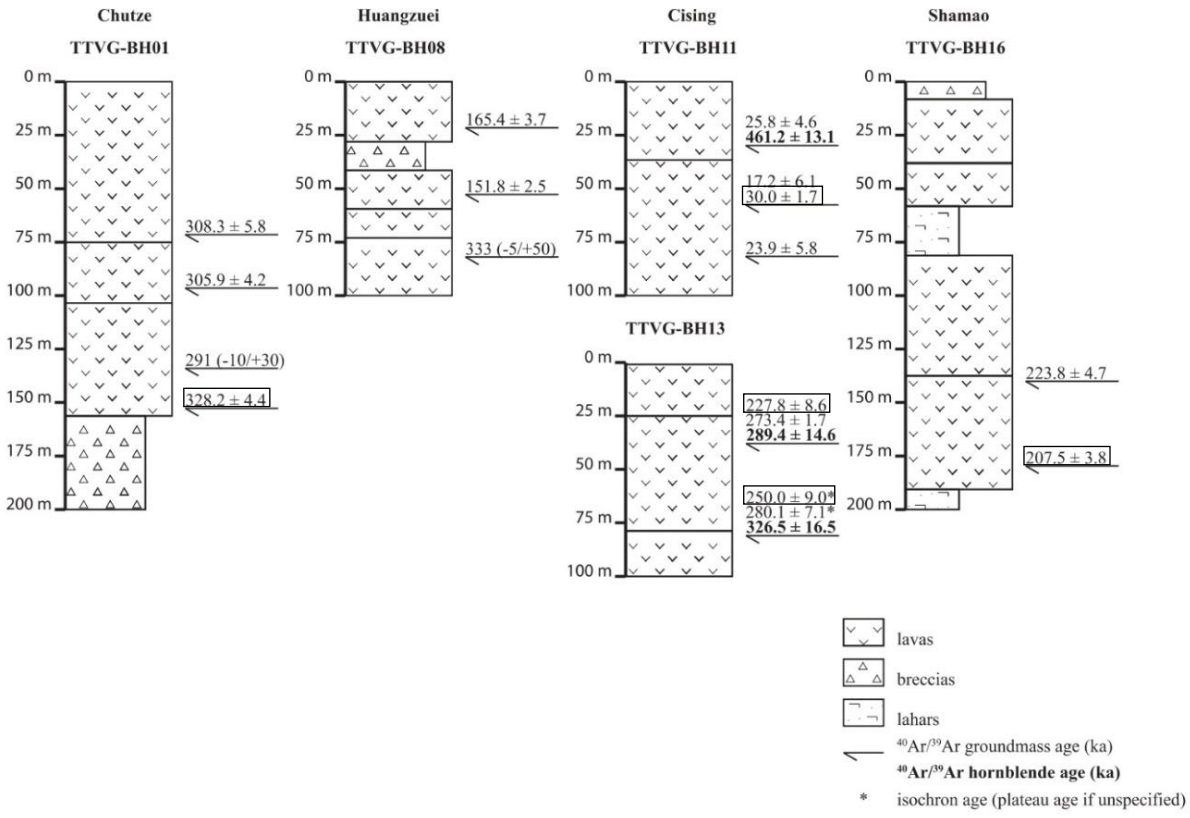

Figure 87: Stratigraphic columns of the boreholes, including sampling sites and their Ar–Ar ages. Boxed ages are the preferred age for that lava flow.

VII. Discussion

A. U–Th Analysis Comparison with Zellmer et al. (2015)

This study's U–Th analyses on Shamao samples reveal significant heterogeneity among duplicates and between our results and those of Zellmer et al. (2015) (Table 12 and Figure 88). Although Shamao 2 and Zellmer's Shamao #166 derive from the same outcrop, our plagioclase and pyroxene duplicates yield different ID and IC values. Moreover, most U and Th concentrations in our groundmass and mineral separates fall

doi:10.6342/NTU202503882

well below those in Zellmer et al. (2015). Shamao 2's groundmass and magnetite isotopic ratios closely match their data, while the plagioclase and pyroxene separates differ isotopically from their counterparts.

Unaltered amphiboles in Shamao 2 contain lower U concentrations than those in Zellmer et al., whereas altered amphiboles exhibit roughly double the amount. Th concentrations in altered and unaltered amphiboles from Shamao 2 were similar to those in Zellmer et al. (2015). While amphiboles in Zellmer et al. (2015) showed a small amount of U excess, the unaltered amphiboles in both Shamao 2 and 3 exhibited Th excess whereas the altered amphiboles record large U excess. This pattern suggests that Zellmer et al.'s amphibole results might represent a mixture of altered and unaltered amphiboles.

Neither this study nor Zellmer et al. obtained robust multi-phase internal isochrons at Shamao. In fact, no mineral phase in this study could be simultaneously paired with both groundmass and magnetite to form a robust isochron, which suggest that these mineral phases are unrelated to the magma with which it erupted with. Two-point isochrons could still be derived from mineral–mineral pairs with magnetite to garner crystallization ages, since magnetite shows the greatest U–Th disequilibrium. Our groundmass–magnetite isochron for Shamao 2 (33.7 ± 1.3 ka, 2σ) agrees with Zellmer et al.'s whole–rock–pyroxene–magnetite age (33.2 ± 1.3 ka, 2σ). However, our duplicates diverge widely: Shamao 2 pyroxene–magnetite yields 38.7 ± 1.5 ka and 29.0

doi:10.6342/NTU202503882

± 1.1 ka. During sample selection, black and opaque pyroxenes were preferred, but most pyroxenes displayed varying levels of discoloration and may have contributed to the discrepancies between duplicates. Our plagioclase–magnetite ages (31.2 ± 1.7 ka and 25.8 ± 2.1 ka) exceed Zellmer et al.'s 18.0 ± 1.3 ka. Our unaltered and altered amphibole–magnetite ages (23.6 ± 1.9 ka and 157 ± 28 ka) bracket Zellmer et al.'s 28.3 ± 1.5 ka, though their age is much closer to our unaltered amphibole–magnetite age. This means that the amphibole results in Zellmer et al. (2015) reflect a mixture of both types of amphiboles, but mostly unaltered amphiboles.

doi:10.6342/NTU202503882

Table 12: #166 Shamao U–Th–Ra compositions from Zellmer et al. (2015).

Phase	U (ng/g)	2s	Th (ng/g)	2s	Ra (fg/g)	2s	(^{234}U/^{238}U)	2s	(^{238}U/^{232}Th)	2s	(^{230}Th/^{232}Th)	2s	(^{226}Ra/^{230}Th)	2s
wr	1619	1.4	5067	6.1	522.4	3.4	1.001	0.007	0.969	0.001	0.919	0.008	1.008	0.006
plag	213	0.6	667	1.8	–	–	0.998	0.007	0.967	0.004	1.06	0.009	–	–
amph	209	0.7	609	0.7	–	–	1.003	0.007	1.044	0.004	0.978	0.008	–	–
px	209	0.2	672	0.6	–	–	1.004	0.007	0.942	0.001	0.908	0.008	–	–
mt	671	0.5	898	0.9	56	0.7	0.996	0.007	2.267	0.003	1.257	0.011	0.447	0.005

doi:10.6342/NTU202503882

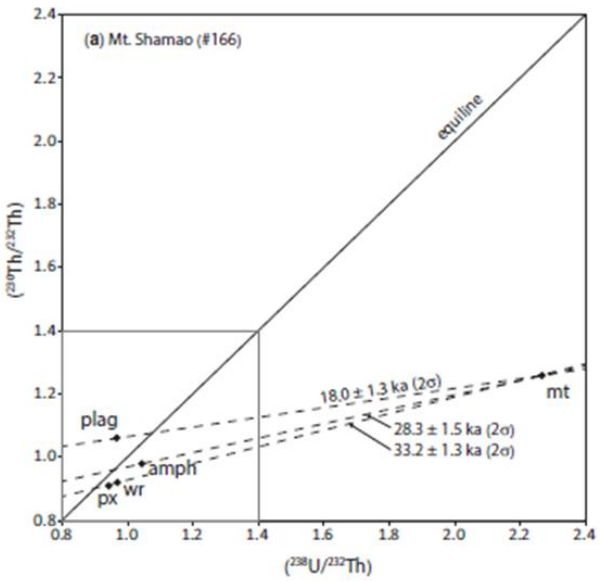

Figure 88: Shamao U–Th isochrons from Zellmer et al. (2015)

Table 13: U–Th isochron age comparison

isochron pairs	**This study**	**Zellmer et al. (2015)**
groundmass–magnetite	33.7 ± 1.3 ka (2σ)	33.2 ± 1.3 ka (2σ) (wr–px–mt)
pyroxene–magnetite	29.0 ± 1.1 ka (2σ)	
	38.7 ± 1.5 ka (2σ)	
plagioclase–magnetite	25.8 ± 2.1 ka (2σ)	18.0 ± 1.3 ka (2σ)
	31.2 ± 1.7 ka (2σ)	
amphibole–magnetite	I:23.6 ± 1.9 ka (2σ)	28.3 ± 1.5 ka (2σ)
	II:157 ± 28 ka (2σ)	

The pronounced isotopic and concentration heterogeneity across duplicates indicates that Shamao rocks incorporate mixed materials from multiple thermal events. The fact that different mineral phases in a sample do not land on the same isochron infers that they are of different ages and thus did not form at the same time. This also applies to crystals of the same mineral phase from the same rock, the duplicates, that do not share the same isotopic composition. The vast discrepancy in appearance, isotopic composition and age

doi:10.6342/NTU202503882

between altered and unaltered amphiboles is a prime example. Additionally, duplicates are of varying initial isotope composition, defined by ($^{238}U/^{232}Th$) at the equipoint, and therefore do not share the same source. Although they are the same type of mineral, they did not crystallize at the same time or from the same source. This could either be due to mixing of older crystals, e.g., sandstone xenoliths, antecrysts, xenocrysts, or due to crystal cores and rims not sharing the same evolutionary histories.

Concluding the U–Th results from this study and those of Zellmer et al. (2015): groundmass and mineral phases do not land on a singular isochron in either study, including their duplicates. This means, not only are the phases from different timelines, each phase contains crystal populations from different timelines. The best example of this are the amphiboles with their different appearances and ages. Multiple U–Th two-point isochrons could be determined to constrain a crystallization age: this study's Shamao 2 has an age range of 21–40 ka and sample #166 from Zellmer et al. (2015) has an age range of 17–35 ka. Only the Shamao 2 groundmass–magnetite age are agreement with the whole rock–pyroxene–magnetite age in #166, and they also display similar isotopic compositions. Whether this is by chance or a testament to its reproducibility requires more testing to determine, but both studies' age ranges share a large overlap between 21–35 ka, which is a demonstration of the U–Th method's ability to constrain TVG ages. Isochron dating was done under the assumption that all minerals formed at the same time (e.g.,

doi:10.6342/NTU202503882

during the eruption), but different mineral phases from the same rock sample do not form a well-behaved isochron. Additionally, bulk mineral isotopic composition analyses assume a synchronous crystallization, but here in Shamao, the same minerals from the same sample do not necessarily share the same isotopic composition or timeline. In the case of the Shamao dome, rocks are very complex and hold geochemical records of too many thermal events within the U–Th system age range for bulk analyses to be capable of differentiating between every one of them. Ra–Th dating may still be capable of singling out Holocene crystal growth ages that may represent eruption, but that requires further validation.

B. Ar–Ar Analysis Comparison with Chang et al. (2024)

Incremental-heating $^{40}Ar/^{39}Ar$ results exhibit large discrepancies between duplicates up to 50 ka, which undermine efforts to sequence closely spaced lava flows using Ar–Ar alone. Nevertheless, groundmass ages from our borehole samples generally increase with depth or cluster with neighboring flows, constraining eruption ages within a few tens of thousands of years.

Two factors drive large uncertainties: (1) low radiogenic Ar, which pushes analyses near detection limits and caused some groundmass runs to fail; and (2) multiphase groundmass, which produces mixed components and scatter in reverse-isochron plots. Scatter degrades isochron definitions and initial $^{40}Ar/^{36}Ar$ estimates. With ages this young,

doi:10.6342/NTU202503882

it is imperative to obtain a well-defined initial $^{40}Ar/^{36}Ar$ as imprecisions can drastically change plateau ages, especially because samples contain little radiogenic Ar to begin with. Assuming atmospheric initial $^{40}Ar/^{36}Ar$ further biases ages because samples contain non-radiogenic Ar—small amounts in groundmass but larger amounts in amphiboles. It is unclear whether the excess Ar is a result Ar contamination or is inherited since both groundmass and amphiboles contain excess Ar. Amphiboles have relatively high Ar retentivity (thus higher initial Ar) and, accordingly, higher closure temperatures (450–600˚C), but basaltic to andesitic eruptions tend to be hotter. It is possible that the magma was not exposed to high enough temperatures for enough time for Ar to fully diffuse out. And with the high cooling rate of a surface eruption, closure temperatures would also be relatively high, possibly freezing the K–Ar system before all Ar has escaped. This would explain why multiphases can be observed in the results: the K–Ar clock was never fully reset. Though this means there are two ways of explaining why amphibole apparent ages are older than groundmass apparent ages: amphiboles have higher Ar retentivity and closure temperatures, or amphiboles are unrelated to the magma it erupted with. The first explanation would require a slow cooling rate following the thermal event from which the amphiboles and groundmass were produced in order for there to be a 400 ky age gap between the groundmass and amphibole results in TTVG-BH11-2931 (Figure 92). This implies a lengthy residence time in the magma reservoir prior to eruption (Costa, 2008).

doi:10.6342/NTU202503882

The U–Th results agree with the second explanation better, but thermochronometry or diffusion modelling may be needed for further support since both could be true.

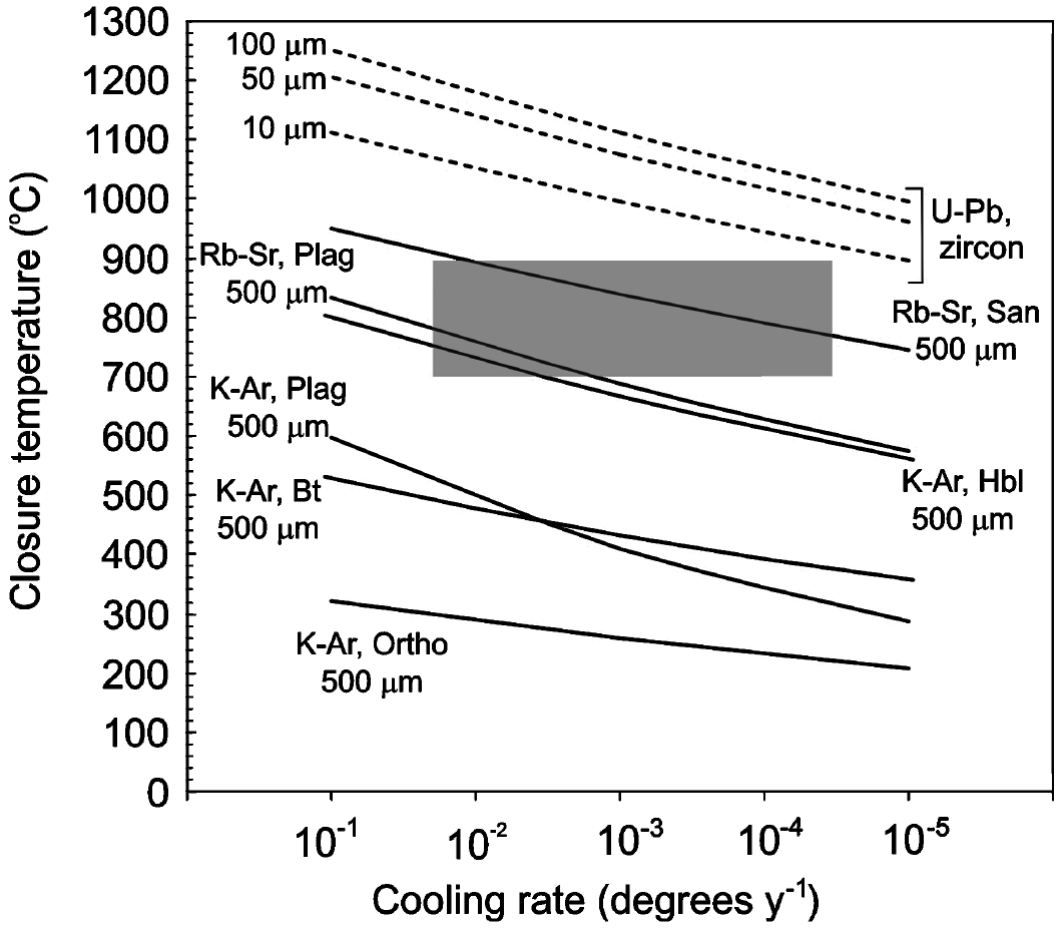

Figure 89: Cooling rates and closure temperatures of various radiometric methods. In the K–Ar system, hornblendes have a higher closure temperature compared to other minerals. (Costa, 2008)

Both this study and Chang et al. (2024) performed Ar–Ar groundmass analyses on the Honlu volcano (Figure 94). The sampling sites are about five hundred meters apart, and 20120809-10 is also from a different side of the volcano and lower down. The Honlu Ar–Ar groundmass plateau age of 0.159 ± 0.017 Ma from Chang et al. (2024) (20120809-10) is around twenty-thousand years older than the groundmass duplicates in this study

doi:10.6342/NTU202503882

(HLS-01), 122.5 ± 7.3 ka (plateau age) and 123.8 ± 10.6 (isochron age), although their isochron age, 0.14 ± 0.03 Ma, is consistent with HLS-01 aliquot 1's isochron age, 148.9 ± 18.2 ka. However, initial $^{40}Ar/^{36}Ar$ values are strikingly different. At 298 ± 2, 20120809-10's resembles atmospheric values while both of HLS-01's aliquots are around 289, making them lower than atmospheric values. This study's isochron diagrams have a lot more scatter compared to the ones in Chang et al. (2024), although, isochron diagrams from both studies capture mixed components and contain various degrees of scatter. This may be a result of different sample preparation methods. In this study, groundmass samples were collected from the leftovers of mineral separation which requires a large amount of rock sample. Whereas, Chang et al. (2024) hand-picked crystal-free grains from a smaller crushed rock sample. If the rock is heterogeneous, using a larger rock sample runs a larger risk of incorporating heterogeneous material and that may be the cause of larger dispersion in the results in this study.

doi:10.6342/NTU202503882

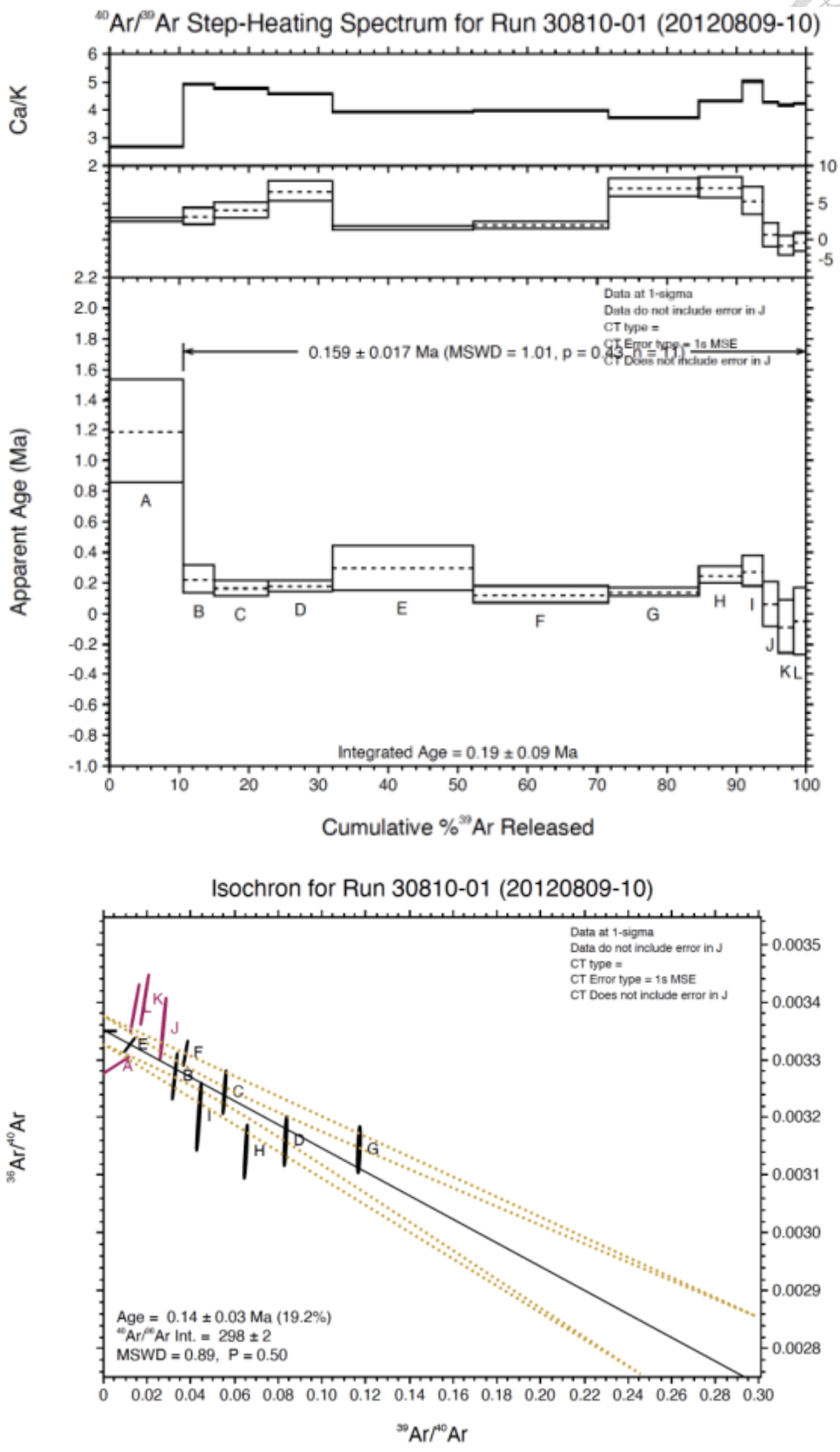

Figure 90: Honlu Ar–Ar age spectrum and reverse isochron from Chang et al. (2024)

doi:10.6342/NTU202503882

Overall, TVG volcanic rocks contain minimal radiogenic Ar, mixed components, and non-radiogenic Ar, all of which inflate uncertainties in young-age Ar–Ar dating. With inconsistencies up to a few tens of thousands of years, using solely Ar–Ar groundmass analysis to reconstruct lava flow sequences that formed in quick succession would be challenging. Mixed components suggest that some components existed before the eruption and the magma was not exposed to high enough temperatures for a long enough duration of time to fully reset the K–Ar clock. Amphibole ages being older than their groundmass counterparts suggests that their clocks were not reset upon eruption and is an example of that. These issues mirror our U–Th findings: discrepancies between amphibole and groundmass ages mean that amphiboles did not crystallize from the magma it erupted with.

C. Shamao U–Th and Ar–Ar Results Comparison

Shamao 2 and Shamao 3 groundmass-related ages diverge between U–Th and Ar–Ar systems. U–Th groundmass–magnetite ages are younger than the Ar–Ar ages. U–Th ages cluster at 15–35 ka (12 ages), ~68 ka (1 age), and >100 ka (2 ages), while Ar–Ar groundmass ages, ~75 ka and ~120 ka, fall between those clusters, suggesting that Ar–Ar reflects weighted mean of mixed components, analogous to how the U–Th groundmass–magnetite ages fall between their associated mineral–mineral ages. Our hand-picked U–Th groundmass samples and mineral separation derived Ar–Ar groundmass produce

doi:10.6342/NTU202503882

consistent relative ages: Shamao 2 dates younger than Shamao 3 by both methods, in agreement with stratigraphic position. However, the absolute age offsets between U–Th and Ar–Ar highlight that mixed mineral populations and partial isotopic retention complicate efforts to pinpoint eruption timing in the Shamao dome.

D. Age Dating Comparison with Previous Studies in the TVG Area

In the past, studies used geochronometric data to reconstruct the eruption sequence of flows in TVG (e.g. Juang and Bellon, 1984; Juang and Chen, 1989; Juang, 1993; Wang and Chen, 1990; Lee, 1996). But large analytical uncertainties on Pleistocene rocks undermine precise sequencing. Stratigraphic best practice instead emphasizes field-based relative ages, using radiometric dates only to support ambiguous cases (Anderson et al., 1998). Accordingly, this study adopts the volcanic stratigraphy in Song et al. (2012) (Figures 91,93, 95, and 97), in which sequences are classified by occurrence, distribution, the results of terrain analysis, superposition, and rock type, to compare published age data from Juang et al. (1984, 1989, 1993), Tsao (1994), Lee (1996), Wang and Chen (1990), Zellmer et al. (2015), Chu et al. (2018), Song et al. (2011), Chang et al. (2024) alongside our new results (Table 14~31 and Figures 92,94, 96, and 98). Ages with large errors were discarded. To avoid comparing rocks from lava flows of unrelated eruptions, data is grouped by volcanic subgroups, then further split into stratigraphic sequences as

doi:10.6342/NTU202503882

classified in Song et al. (2012). Within each sequence, results are compared in an attempt to constrain an eruption age. In general, if isotopic systems remained closed after eruption, then multiphase samples would measure older than crystallization or cooling age, and eruption age is most likely to be younger than the results. That is why ages will be constrained to within the youngest ages that have also been reproduced in a separate analysis.

The TVG subgroups in this comparison are Cising (C), Huangzuei (H), Chutze (Z), and Tatun (T). We exclude Dinghuoshou, whose older age is well established. Sequences in each subgroup are numbered from oldest to youngest. Example: Cising's bottommost sequence would be numbered C1, the sequence on top of that would be C2, and etc.

doi:10.6342/NTU202503882

1. *Cising Subgroup*

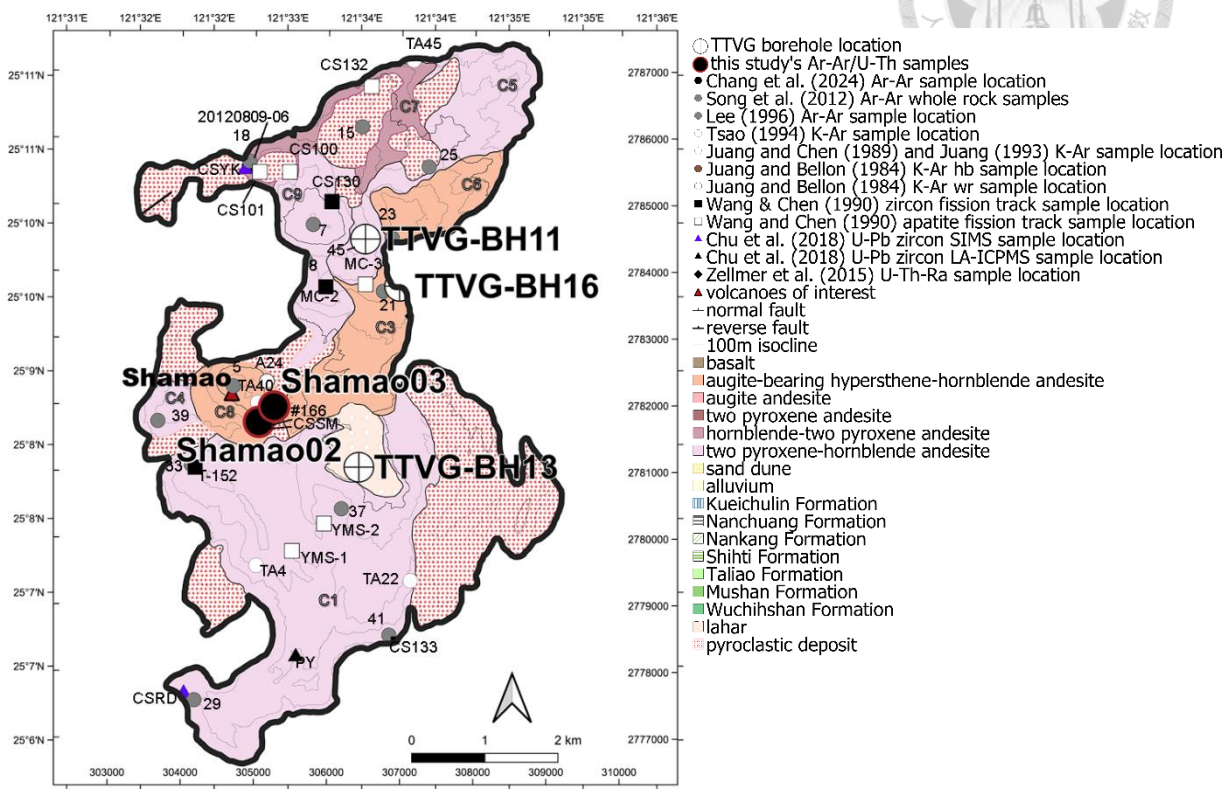

Figure 91: Map of the Cising subgroup volcanic sequence as proposed in Song et. al （2012）and sampling sites of compiled age data.

doi:10.6342/NTU202503882

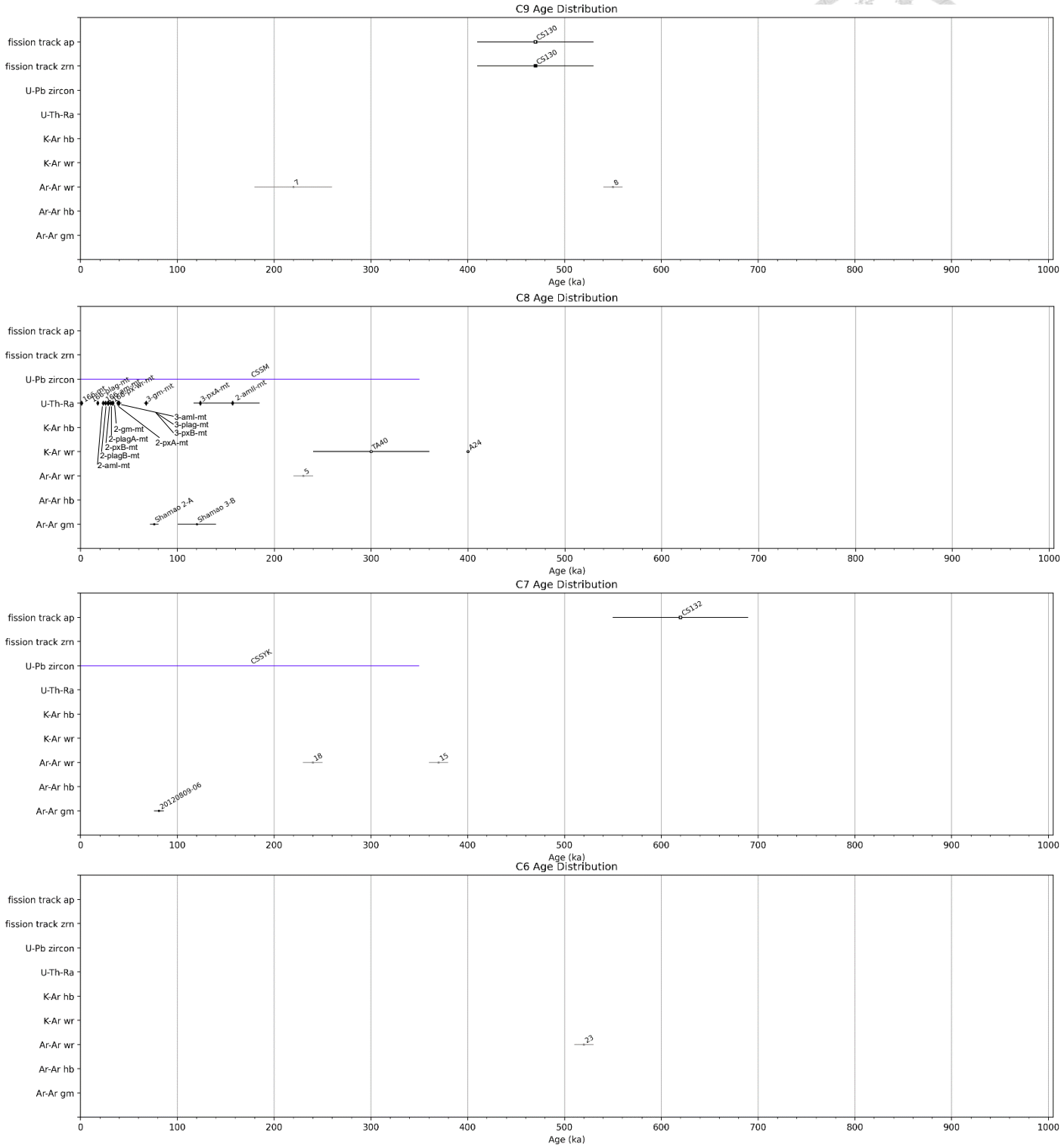

Figure 92: Cising Subgroup sequence C1~C9 ages.

doi:10.6342/NTU202503882

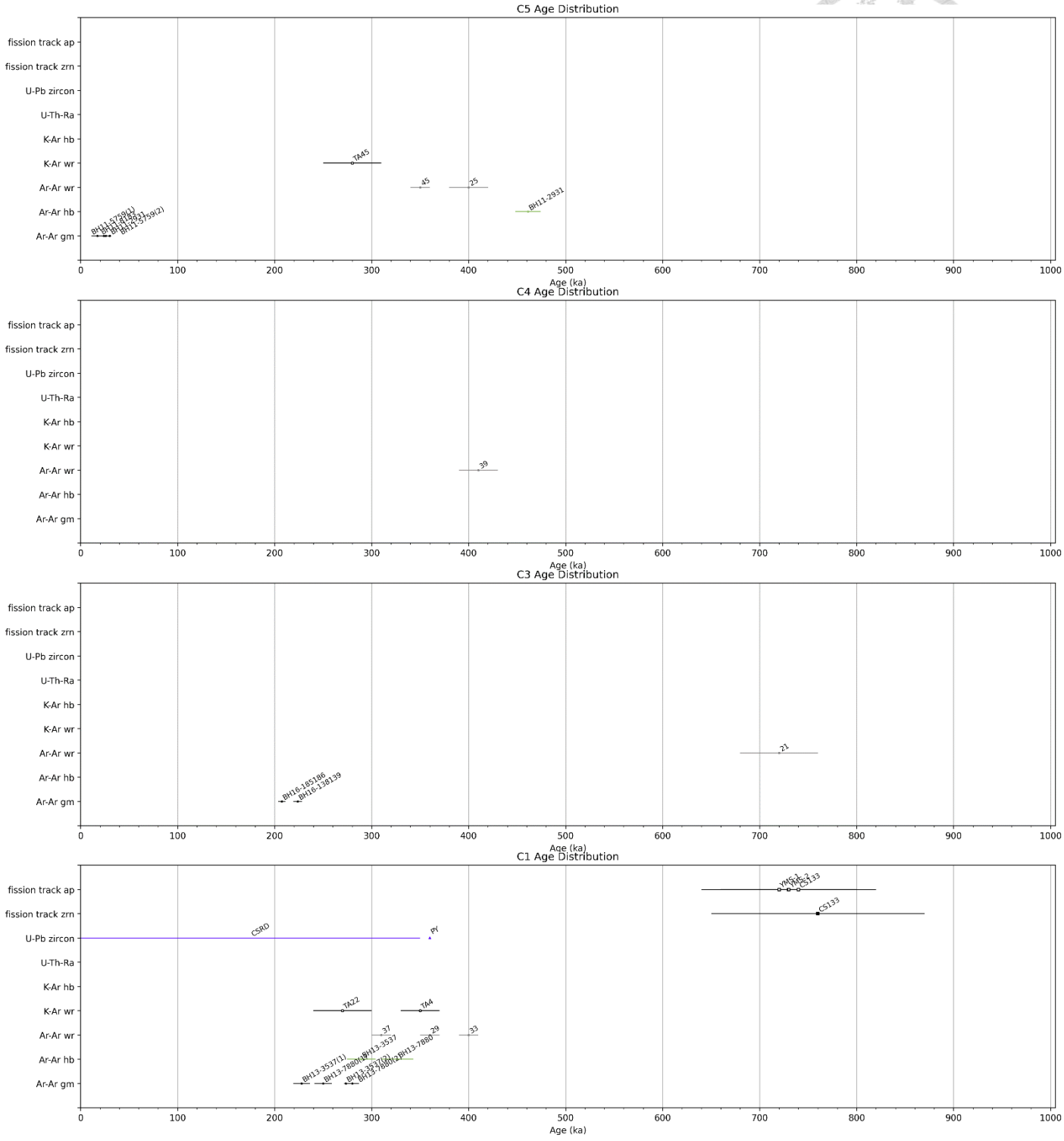

Figure 92: (continued)

doi:10.6342/NTU202503882

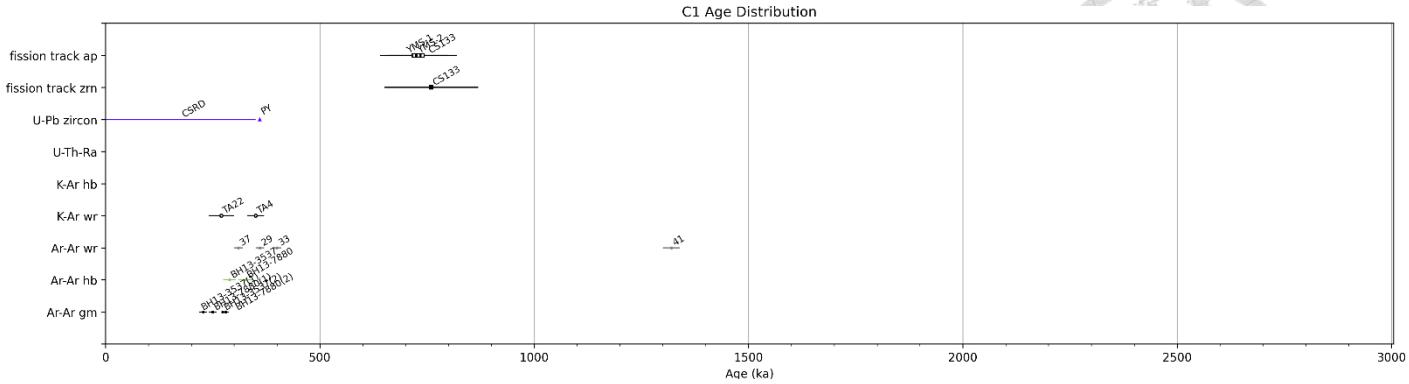

Figure 92: (continued)

C1: This sequence consists of four Ar–Ar groundmass ages, two Ar–Ar hornblende ages, four Ar–Ar whole rock ages, two K–Ar whole rock ages, two U–Pb zircon ages, one fission track zircon age, and three fission track apatite ages. Although samples CS133 & 41 are almost from the same location but have very different values, with sample 41 being much older than any other samples in this sequence at ~1.3 Ma. CS133 & YMS-1, YMS-2 have similar values even though they are sourced from different locations. Other than 41, all other samples are clustered into two groups despite coming from different locations. Fission track ages range from 640 to 880 ka, and everything else can be found between 220 and 420 ka. With Ar–Ar hornblende ages in this dataset, it can be observed that the second aliquots of the Ar–Ar groundmass analyses, in which multiphases were present, appear to be similar to the hornblende ages, possibly an indication that the older results of the second aliquots is a result of the presence of phases of similar origin to the hornblendes. Thus, it can be inferred that the whole rock ages have also been affected in a similar matter. Going by the results of the first aliquots of the Ar–Ar groundmass analyses, the eruption of this sequence occurred within ~235 ka.

doi:10.6342/NTU202503882

Table 14: C1 age data compilation listed by age from youngest to oldest.

Sample	Method	Material	Age (ka)	± (1σ)	Source
TTVG-BH13-3537 (Aliquot 1)	Ar–Ar (plateau)	groundmass	227.8	8.6	this study
TTVG-BH13-7880 (Aliquot 1)	Ar–Ar (isochron)	groundmass	250	9	this study
TA22	K–Ar	whole rock	270	30	Tsao (1994)
TTVG-BH13-3537 (Aliquot 2)	Ar–Ar (plateau)	groundmass	273.4	1.7	this study
TTVG-BH13-7880 (Aliquot 2)	Ar–Ar (plateau)	groundmass	280.1	7.1	this study
TTVG-BH13-3537	Ar–Ar (plateau)	hornblende	289.4	14.6	this study
37	Ar–Ar (plateau)	whole rock	310	10	Lee (1996)
TTVG-BH13-7880	Ar–Ar (plateau)	hornblende	326.5	16.5	this study
TA4	K–Ar	whole rock	350	20	Tsao (1994)
CSRD	U–Pb	zircon	<350		Chu et al. (2018)
29	Ar–Ar (plateau)	whole rock	360	10	Lee (1996)
PY	U–Pb zircon	zircon	360		Chu et al. (2018)
33	Ar–Ar (plateau)	whole rock	400	10	Lee (1996)
YMS-1	fission track	apatite	720	80	Wang and Chen (1990)
YMS-2	fission track	apatite	730	70	Wang and Chen (1990)
CS133	fission track	apatite	740	80	Wang and Chen (1990)
CS133	fission track	zircon	760	110	Wang and Chen (1990)
41	Ar–Ar (plateau)	whole rock	1320	20	Lee (1996)

doi:10.6342/NTU202503882

C3: This sequence consists of two Ar–Ar groundmass ages and one Ar–Ar whole rock age. Sampling sites are also quite far from each other amongst different methods. Borehole Ar–Ar groundmass results are similar to each other, between 200 and 230 ka. borehole results. It can be concluded that the eruption of this sequence occurred within ~210 ka.

Table 15: C3 age data compilation listed by age from youngest to oldest.

Sample	Method	Material	Age (ka)	± (1σ)	Source
TTVG-BH16-185186	Ar–Ar (plateau)	groundmass	207.5	3.8	this study
TTVG-BH16-138139	Ar–Ar (plateau)	groundmass	223.8	4.7	this study
21	Ar–Ar (total gas)	whole rock	720	40	Lee (1996)

C4 has only one Ar–Ar whole rock age of ~410 from sample 39. More samples are needed for comparison.

Table 16: C4 age data compilation listed by age.

Sample	Method	Material	Age (ka)	± (1σ)	Source
39	Ar–Ar (plateau)	whole rock	410	20	Lee (1996)

C5: This sequence consists of four Ar–Ar groundmass ages, one Ar–Ar hornblende age, two Ar–Ar whole rock ages, and one K–Ar whole rock age. Aside from the borehole samples, sampling sites are spread across the area. Ar–Ar groundmass borehole ages range between 15 and 30 ka, while the TTVG-BH11-2931 Ar–Ar hornblende age is around 460 ka. Much like the C1 sequence, the hornblende age is much older than its

doi:10.6342/NTU202503882

groundmass counterpart. All whole rock results fall between Ar–Ar groundmass and hornblende ages and are likely a reflection of weighted mean averages of multiple components. The Ar–Ar groundmass ages constrain the eruption age of this sequence to within ~30 ka.

Table 17: C5 age data compilation listed by age from youngest to oldest.

Sample	Method	Material	Age (ka)	± (1σ)	Source
TTVG-BH11-5759 (Aliquot 1)	Ar–Ar (plateau)	groundmass	17.2	6.1	this study
TTVG-BH11-8183	Ar–Ar (plateau)	groundmass	23.9	5.8	this study
TTVG-BH11-2931	Ar–Ar (plateau)	groundmass	25.8	4.6	this study
TTVG-BH11-5759 (Aliquot 2)	Ar–Ar (plateau)	groundmass	30.0	1.7	this study
TA45	K–Ar	whole rock	280	30	Tsao (1994)
45	Ar–Ar (plateau)	whole rock	350	10	Lee (1996)
25	Ar–Ar (plateau)	whole rock	400	20	Lee (1996)
TTVG-BH11-2931	Ar–Ar (plateau)	hornblende	461.2	13.1	this study

C6: There is only one Ar–Ar whole rock age of ~520 ka in this sequence. More samples are needed for comparison.

Table 18: C6 age data compilation listed by age.

Sample	Method	Material	Age (ka)	± (1σ)	Source
23	Ar–Ar (plateau)	whole rock	520	10	Lee (1996)

C7: This sequence consists of one Ar–Ar groundmass age, two Ar–Ar whole rock

doi:10.6342/NTU202503882

ages, one U–Pb zircon age, and one fission track apatite age. The CSYK U–Pb zircon sample, 18 Ar–Ar whole rock sample, and 20120908-06 Ar–Ar groundmass sample are all from similar locations. CYSK U–Pb zircon constraints encompass two Ar–Ar ages, even though the groundmass age and whole rock age are quite different, and another Ar–Ar whole rock age is just outside of range. Such as the cases in C1, C3, and C5, the whole rock ages are much older than the groundmass age, possibly due to multiphases skewing the results. The fission track age is much older than all other results. As there is not much data and not much overlap between existing data, it is difficult to constrain the age of this sequence with what is currently available.

Table 19: C7 age data compilation listed by age from youngest to oldest.

Sample	**Method**	**Material**	**Age (ka)**	**± (1σ)**	**Source**
20120809-06	Ar–Ar (plateau)	groundmass	81	5	Chang et al. (2024)
18	Ar–Ar (plateau)	whole rock	240	10	Lee (1996)
CSSYK	U–Pb zircon	zircon	<350		Chu et al. (2018)
15	Ar–Ar (plateau)	whole rock	370	10	Lee (1996)
CS132	fission track	apatite	620	70	Wang and Chen (1990)

C8: This sequence consists of two Ar–Ar groundmass ages, one Ar–Ar whole rock age, two K–Ar whole rock ages, one U–Pb zircon age, and sixteen U–Th–Ra ages. Other than Shamao 2 and #166, all other samples come from different parts of the Shamao dome.

doi:10.6342/NTU202503882

The CSSM U–Pb zircon age constraints encompass all but the A24 K–Ar whole rock age. The Ar–Ar groundmass ages are about 20 ka apart, at around 80 ka and 100 to 140 ka, but both are much younger the whole rock ages, which are between 220 and 400 ka, much like what has been observed in C1, C3, C5, and C7. On a <1Ma scale, U–Th results appear to agree well, with most isochrons ages clustered between 15 and 35 ka and two fall in the >100 ka range. As mentioned in the previous section, Ar–Ar groundmass ages land between the U–Th ages. The Ra–Th magnetite age of 1367 ± 0.011 (2σ) years-old has yet to be verified, thus, the eruption age of this sequence is currently constrained U–Th plagioclase–magnetite ages to within ~25 ka.

Table 20: C8 age data compilation listed by age from youngest to oldest.

Sample	**Method**	**Material**	**Age (ka)**	**± (1σ)**	**Source**
166-mt	Ra–Th	magnetite	1.367	0.011 (2σ)	Zellmer et al. (2015)
166-plag-mt	U–Th	plagioclase, magnetite	18.0	1.3 (2σ)	Zellmer et al. (2015)
Shamao 2-amI-mt	U–Th	amphibole, magnetite	23.6	1.9 (2σ)	this study
Shamao 2-plagB-mt	U–Th	plagioclase, magnetite	25.8	2.1 (2σ)	this study
166-am-mt	U–Th	amphibole, magnetite	28.3	1.5 (2σ)	Zellmer et al. (2015)
Shamao 2-pxB-mt	U–Th	pyroxene, magnetite	29.0	1.1 (2σ)	this study
Shamao 2-plagA-mt	U–Th	plagioclase, magnetite	31.2	1.7 (2σ)	this study
166-px-wr-mt	U–Th	groundmass, pyroxene, magnetite	33.2	1.3 (2σ)	Zellmer et al. (2015)

doi:10.6342/NTU202503882

Shamao 2-gm-mt	U–Th	groundmass, magnetite	33.7	1.3 (2σ)	this study
Shamao 2-pxA-mt	U–Th	pyroxene, magnetite	38.7	1.5 (2σ)	this study
Shamao 3-pxB-mt	U–Th	pyroxene, magnetite	39.6	1.2 (2σ)	this study
Shamao 3-plag-mt	U–Th	plagioclase, magnetite	39.8	1.9 (2σ)	this study
Shamao 3-amI-mt	U–Th	amphibole, magnetite	39.9	2.6 (2σ)	this study
Shamao 3-gm-mt	U–Th	groundmass, magnetite	67.9	2.3 (2σ)	this study
Shamao 2-A	Ar–Ar (plateau)	groundmass	76.1	4.4	this study
Shamao 3-B	Ar–Ar (plateau)	groundmass	120.1	19.9	this study
Shamao 3-pxA-mt	U–Th	pyroxene, magnetite	123.8	7.1 (2σ)	this study
Shamao 2-amII-mt	U–Th	amphibole, magnetite	157	28 (2σ)	this study
5	Ar–Ar (plateau)	whole rock	230	10	Lee (1996)
TA40	K–Ar	whole rock	300	60	Tsao (1994)
CSSM	U–Pb zircon	zircon	<350		Chu et al. (2018)
A24	K–Ar	whole rock	400		Juang and Bellon (1984)
CSSM	U–Pb zircon	zircon	<350		Chu et al. (2018)

C9: This sequence consists of two Ar–Ar whole rock ages, one fission track zircon age, and one fission track apatite age. The few existing data points come from different parts of C9. The CS130 fission track zircon and apatite samples and an Ar–Ar whole rock

doi:10.6342/NTU202503882

sample are similar in age, mostly due to fission track ages having a large error bar, but could also reflect an event that occurred between 400 and 560 ka. The remaining Ar–Ar whole rock sample resulted in a much younger age than the others. Due to little overlap between the sparse amount of data, it is difficult to come to any conclusions, and more data is needed.

Table 21: C9 age data compilation listed by age from youngest to oldest.

Sample	Method	Material	Age (ka)	± (1σ)	Source
7	Ar–Ar (plateau)	whole rock	220	40	Lee (1996)
CS130	fission track	zircon	470	60	Wang and Chen (1990)
CS130	fission track	apatite	470	60	Wang and Chen (1990)
8	Ar–Ar (plateau)	whole rock	550	10	Lee (1996)

doi:10.6342/NTU202503882

2. *Huangzuei Subgroup*

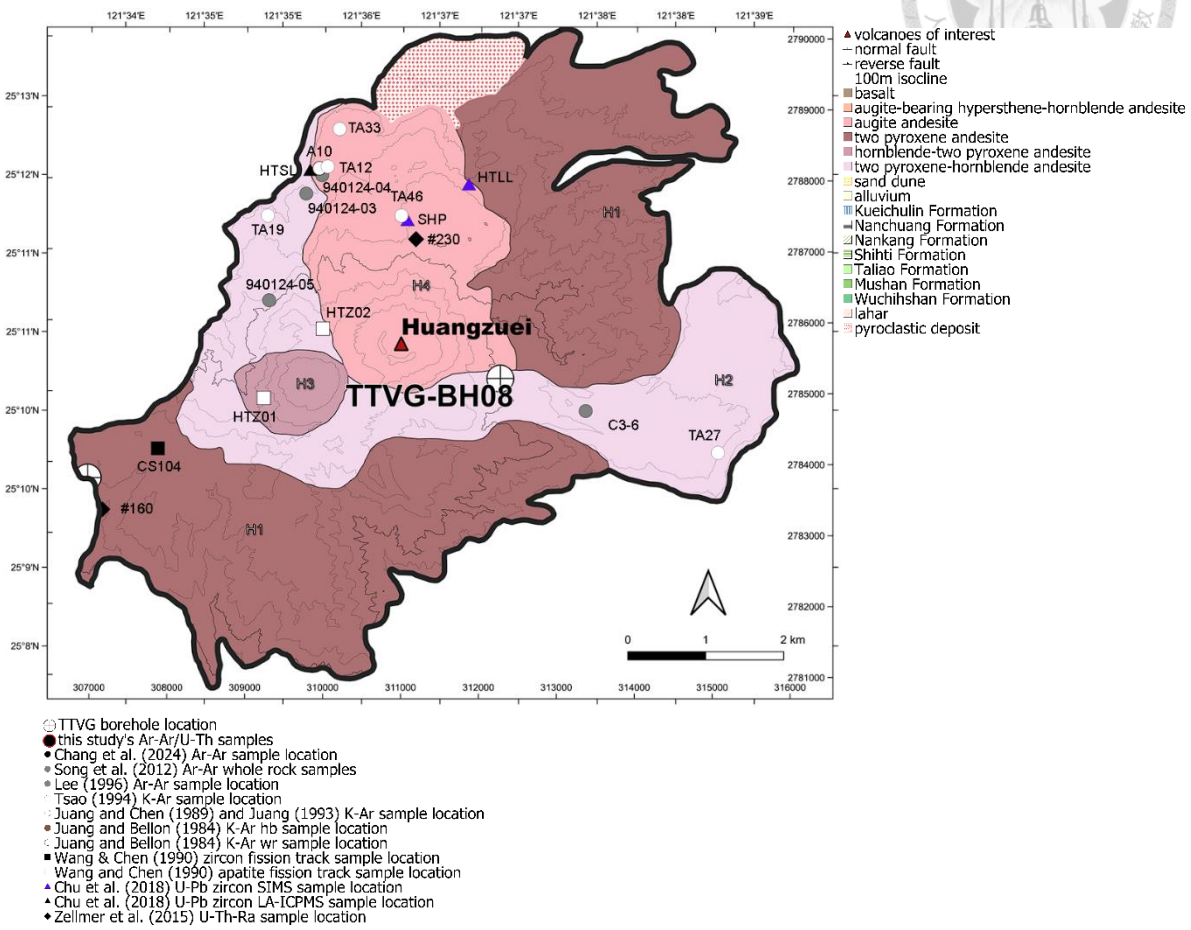

Figure 93: Map of the Huangzuei subgroup volcanic sequence as proposed in Song et. al（2012）and sampling sites of compiled age data.

doi:10.6342/NTU202503882

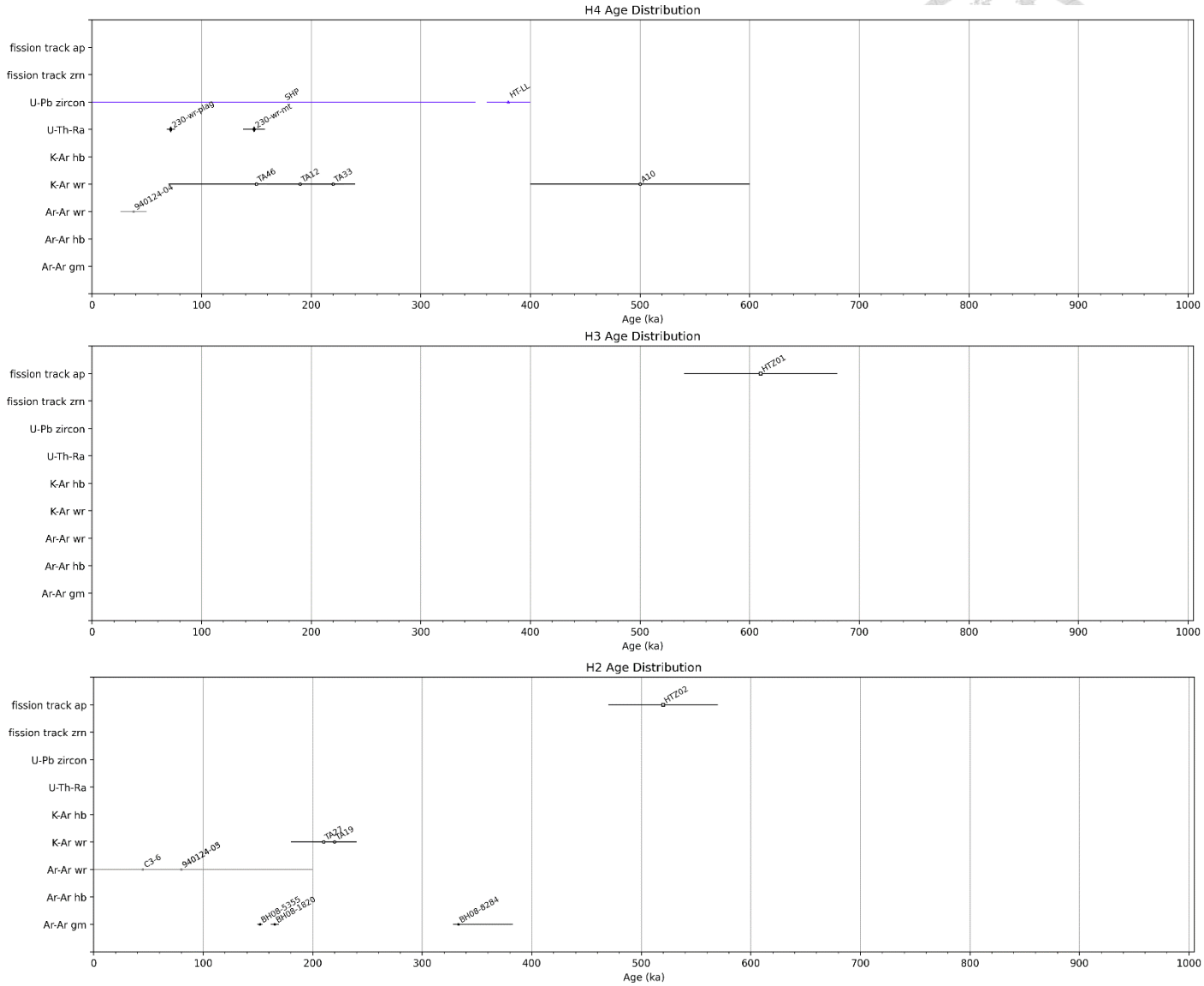

Figure 94: Huangzuei subgroup sequence H2~H4 ages.

H1 has no data.

H2: This sequence consists of three Ar–Ar groundmass ages, two Ar–Ar whole rock ages, two K–Ar whole rock ages, and one fission track apatite age. Aside from HTZ02 fission track sample and an Ar–Ar groundmass sample from the bottom of borehole BH08, all other age results lie within 240 ka years, despite being sourced from all across the area.

doi:10.6342/NTU202503882

At 151.8 ± 2.5 ka and 165.4 ± 3.7 ka, the TTVG-BH08-5355 and TTVG-BH08-1820 Ar–Ar groundmass ages are extremely close, just missing each other by almost eight thousand years. Due to its large error bar, the 910124-09 Ar–Ar whole rock age range fully encompasses both the TTVG-BH08-5355 and TTVG-BH08-1820 Ar–Ar groundmass ages and the C3-6 Ar–Ar whole rock age. It also overlaps the lower end of the Ar–Ar whole rock samples' age ranges. While there is no overlap between TA27 and TTVG-BH08-1820, the lower end of the TA27 age range misses the upper end of TTVG-BH08-1820 just by a little over ten thousand years and the upper end of TTVG-BH08-5355 by a little over twenty-five thousand years. Additionally, considering the conclusion made in C1, C3, C5, C7, and C8 that whole rock results are skewed due to the presence of multiphases within the samples, Ar–Ar groundmass results are the most representative of the age of this sequence, which constrains the eruption age to within ~170 ka.

doi:10.6342/NTU202503882

Table 22: H2 age data compilation listed by age from youngest to oldest.

Sample	Method	Material	Age (ka)	± (1σ)	Source
C3-6	Ar–Ar (isochron)	whole rock	45	13	Song et al. (2011)
940124-03	Ar–Ar (isochron)	whole rock	80	20	Song et al. (2011)
940124-05	Ar–Ar (isochron)	whole rock	80	120	Song et al. (2011)
TTVG-BH08-5355	Ar–Ar (plateau)	groundmass	151.8	2.5	this study
TTVG-BH08-1820	Ar–Ar (plateau)	groundmass	165.4	3.7	this study
TA27	K–Ar	whole rock	210	30	Tsao (1994)
TA19	K–Ar	whole rock	220	20	Tsao (1994)
TTVG-BH08-8284	Ar–Ar (plateau)	groundmass	333	(-5/+50)	this study
HTZ02	fission track	apatite	520	50	Wang and Chen (1990)

H3 only has one fission track apatite age of ~610 ka from HTZ01.

Table 23: H3 age data compilation listed by age.

Sample	Method	Material	Age (ka)	± (1σ)	Source
HTZ01	fission track	apatite	610	70	Wang and Chen (1990)

H4: This sequence consists of one Ar–Ar whole rock age, four K–Ar whole rock ages, two U–Th ages, and two U–Pb zircon ages. Samples A10, TA12, and 940124-04 are from the same area, yet, A10 is much older than the other two by circa one-hundred sixty years. TA46, SHP, and #230 are from around the same location, and both the TA46 K–Ar whole rock age and the #230 U–Th ages, 72 ± 4 ka and 148 ± 10 ka, fall within the SHP U–Pb zircon age constraints. The TA46 age range also encompasses both of the #230 U–

doi:10.6342/NTU202503882

Th ages. The youngest age is an Ar–Ar whole rock age, 38 ± 12 ka, from sample 940124-04 that misses the lower end of the #230 U–Th whole rock–plagioclase age range by just eighteen thousand years. The 940124-04 Ar–Ar whole rock age range does not overlap with any other sample, therefore, with the current data, the eruption age of this sequence can be constrained to within ~80 ka.

Table 24: H4 age data compilation listed by age from youngest to oldest.

Sample	**Method**	**Material**	**Age (ka)**	**± (1σ)**	**Source**
940124-04	Ar–Ar (isochron)	whole rock	38	12	Song et al. (2011)
230-wr-plag	U–Th	groundmass, plagioclase	72	4 (2σ)	Zellmer et al. (2015)
230-wr-mt	U–Th	groundmass, magnetite	148	10 (2σ)	Zellmer et al. (2015)
TA46	K–Ar	whole rock	150	80	Tsao (1994)
TA12	K–Ar	whole rock	190	30	Tsao (1994)
TA33	K–Ar	whole rock	220	20	Tsao (1994)
SHP	U–Pb zircon	zircon	<350		Chu et al. (2018)
HT-LL	U–Pb zircon	zircon	380	20	Chu et al. (2018)
A10	K–Ar	whole rock	500	100	Juang and Bellon (1984)

doi:10.6342/NTU202503882

3. *Tatun Subgroup*

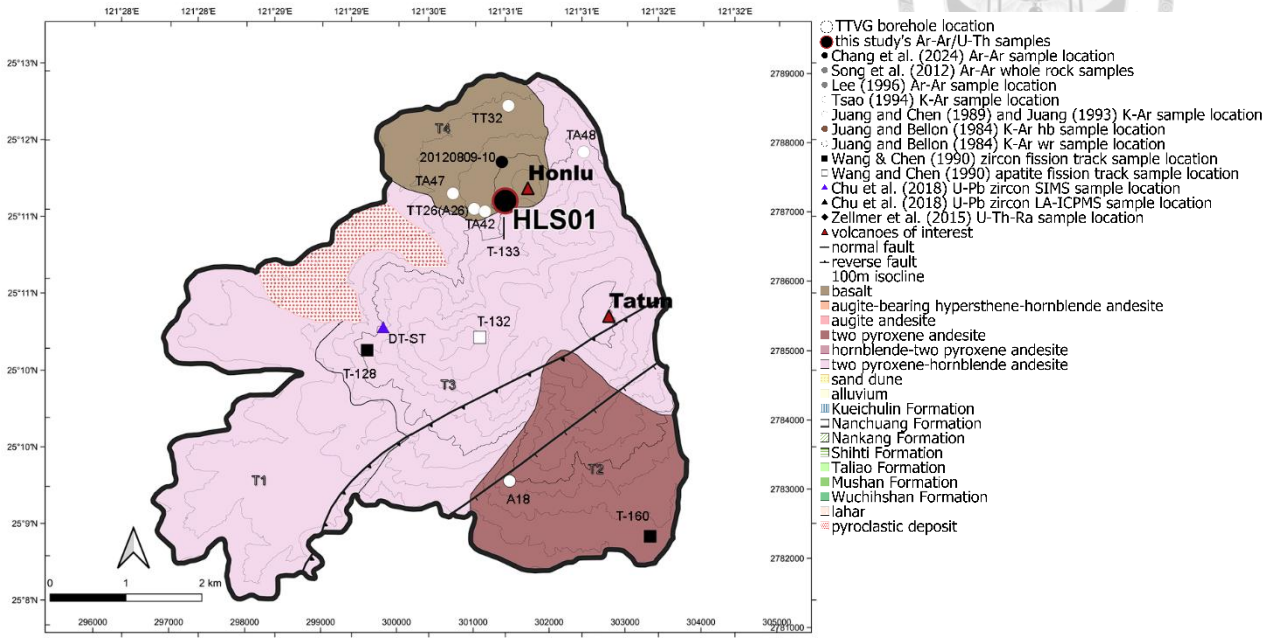

Figure 95: Map of the Tatun subgroup volcanic sequence as proposed in Song et. al （2012）and sampling sites of compiled age data.

doi:10.6342/NTU202503882

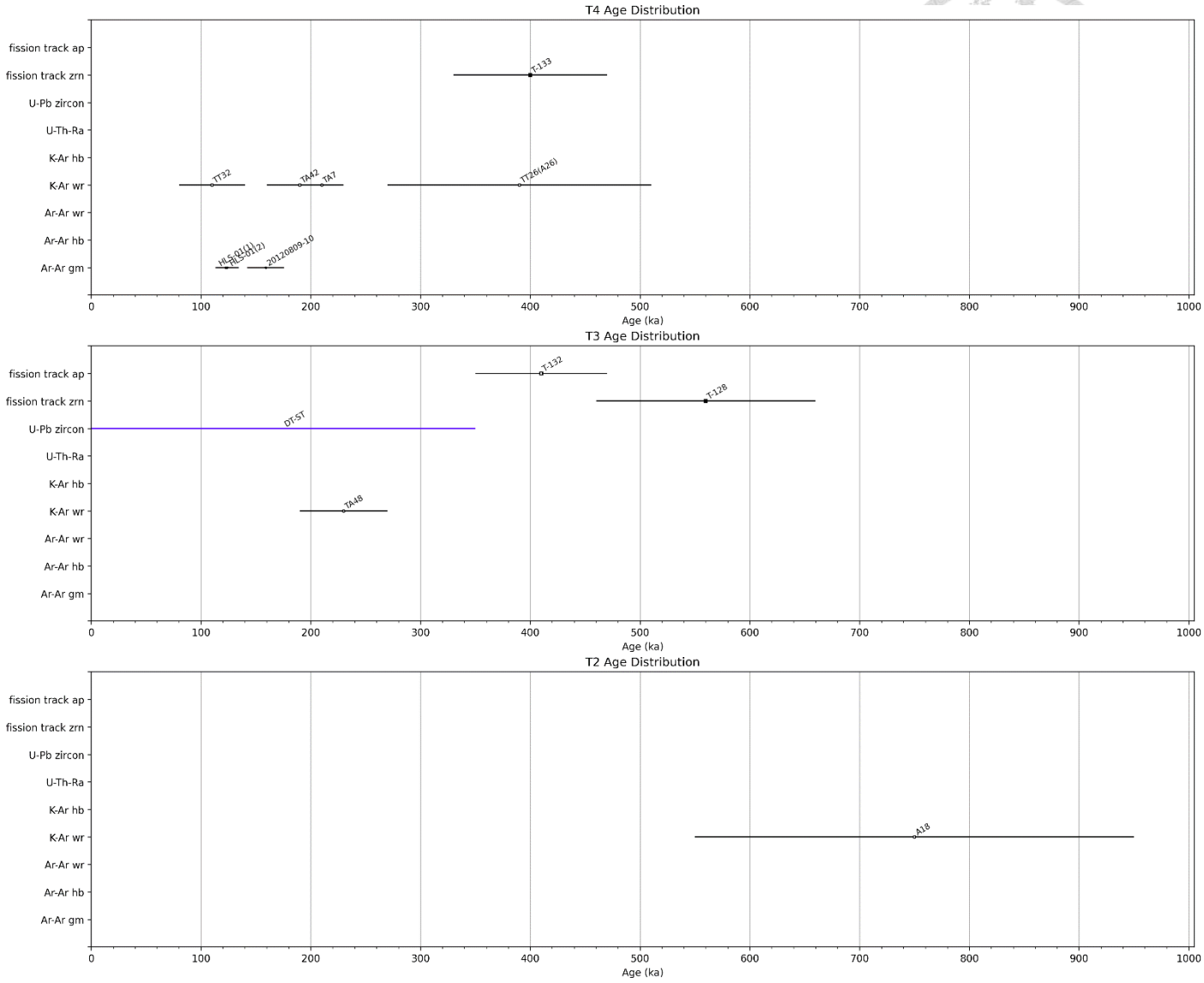

Figure 96: Tatun subgroup sequence T2~T4 ages.

+

T1 has no data.

T2 has only a K–Ar whole rock age of 750 ka from A18.

Table 25: T2 age data compilation listed by age.

Sample	Method	Material	Age (ka)	± (1σ)	Source
A18	K–Ar	whole rock	750	200	Juang and Bellon (1984)

T3: This sequence consists of one K–Ar whole rock age, one U–Pb zircon age, one fission track zircon age, and one fission track apatite age. The TA48 sample site is very

doi:10.6342/NTU202503882

far from all the others. DT-ST, T-132, and T-128 are relatively close, especially, DT-ST and T-132. However, only the TA48 K–Ar whole rock age range, 180 to 270 ka, falls within the constraints of the DT-ST U–Pb zircon results, while the T-132 apatite fission track age falls just outside, and the T-128 zircon fission track age is even older. There is a small amount of overlap between T-132 and T-128 at around 470 ka, though it is unclear what if this is of any significance. With the current data, the eruption age of this sequence can be constrained by the TA48 K–Ar whole rock result to within ~270 ka.

Table 26: T3 age data compilation listed by age from youngest to oldest.

Sample	Method	Material	Age (ka)	± (1σ)	Source
TA48	K–Ar	whole rock	230	40	Tsao (1994)
DT-ST	U–Pb zircon	zircon	<350		Chu et al. (2018)
T-132	fission track	apatite	410	60	Wang and Chen (1990)
T-128	fission track	zircon	560	100	Wang and Chen (1990)

T4: This sequence consists of three Ar–Ar groundmass ages, four K–Ar whole rock ages, and one fission track zircon age. T-133 and HLS-01 come from roughly the same site. Other than TT32, most samples in this area are in close vicinity of each other. The K–Ar whole rock ages cover a broad range of ages, somehow with very little overlap despite having four data points. The TT26 K–Ar whole rock age range encompasses the T-133 fission track zircon age, suggesting that an event may have occurred at ~400 ka, although it is unclear what. The TT32 K–Ar whole rock sample age range encompasses the HLS-01 Ar–Ar groundmass ages, which constrains the eruption age in this sequence

doi:10.6342/NTU202503882

to within ~120 ka.

Table 27: T4 age data compilation listed by age from youngest to oldest.

Sample	**Method**	**Material**	**Age (ka)**	**± (1σ)**	**Source**
TT32	K–Ar	whole rock	110	30	Juang (1993)
HLS-01 (Aliquot 1)	Ar–Ar (plateau)	groundmass	122.5	7.3	this study
HLS-01 (Aliquot 2)	Ar–Ar (isochron)	groundmass	123.8	10.5	this study
20120809-10	Ar–Ar (plateau)	groundmass	159	17	Chang et al. (2024)
TA42	K–Ar	whole rock	190	30	Tsao (1994)
TA7	K–Ar	whole rock	210	20	Tsao (1994)
TT26 (A26)	K–Ar	whole rock	390	120	Juang (1993); Juang and Chen (1989)
T-133	fission track	zircon	400	70	Wang and Chen (1990)

doi:10.6342/NTU202503882

4. *Chutze Subgroup*

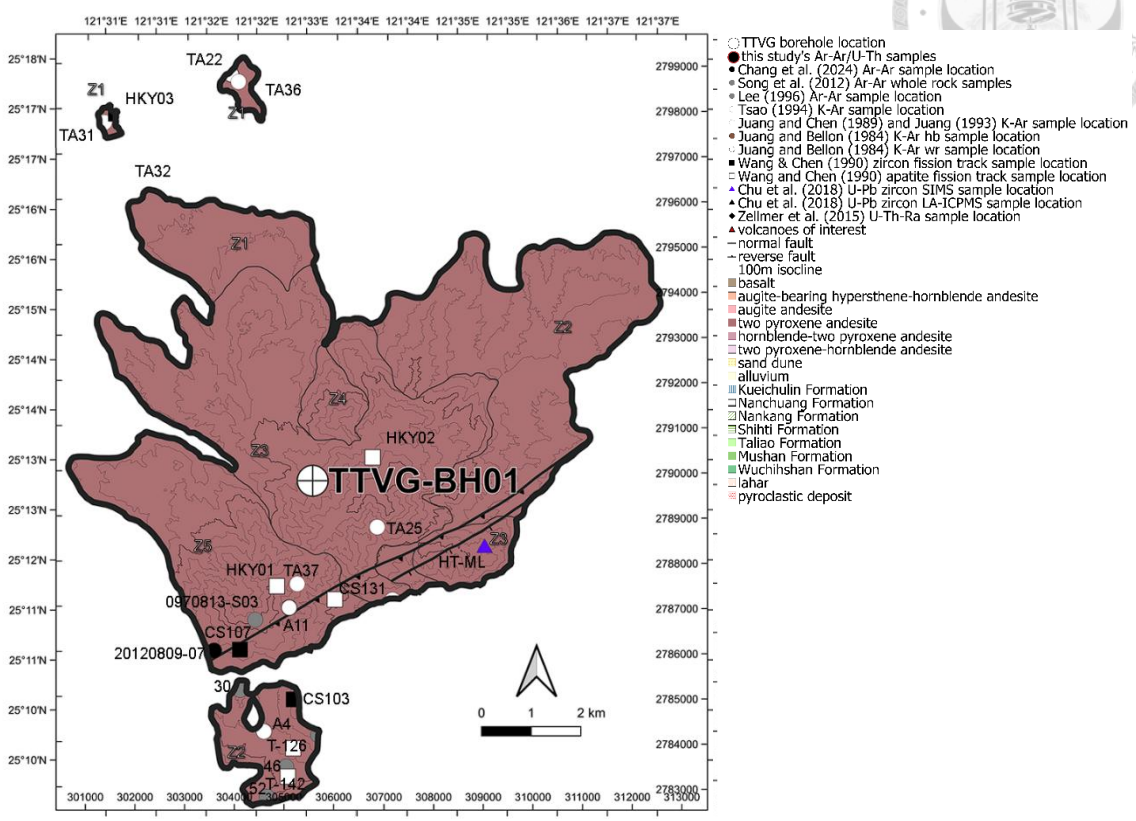

Figure 97: Map of the Chutze subgroup volcanic sequence as proposed in Song et. al（2012）and sampling sites of compiled age data.

doi:10.6342/NTU202503882

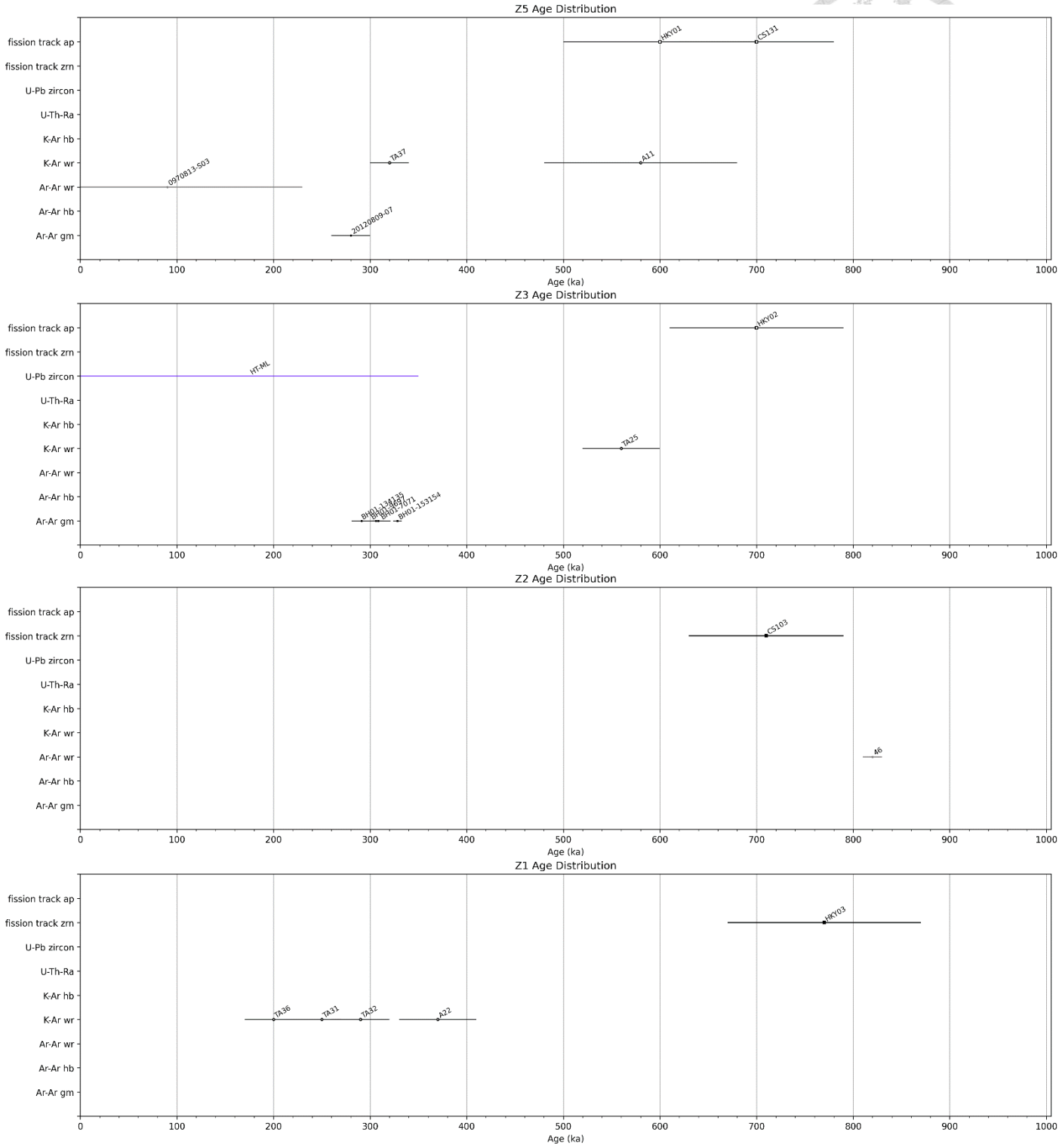

Figure 98: Chutze subgroup sequence Z1~Z5 ages.

doi:10.6342/NTU202503882

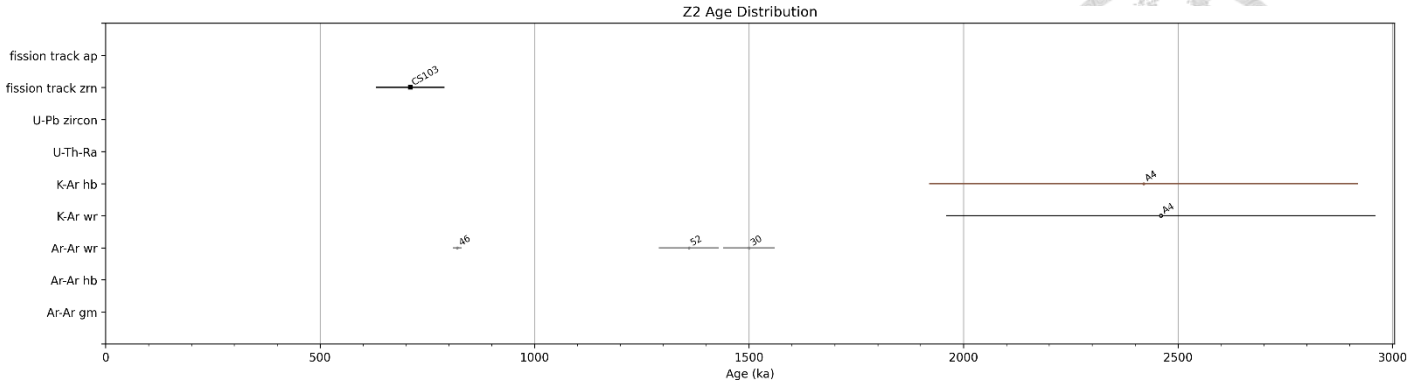

Figure 98: (continued)

Z1: This sequence consists of only four K–Ar whole rock ages and one fission track zircon age. The K–Ar whole rock ages all lie within 160 to 420 ka, but have very little overlap. Samples A22 and TA36, in particular, have very different ages even though they originate from the same location. The HKY03 fission track zircon sample is nearly twice the age of the TA31 K–Ar whole rock sample even though they are both from the same site. The lack of overlapping ages, especially for samples from the same locations, makes it difficult to discern much information or validate different dating methods from this sequence.

Table 28: Z1 age data compilation listed by age from youngest to oldest.

Sample	Method	Material	Age (ka)	± (1σ)	Source
TA36	K–Ar	whole rock	200	30	Tsao (1994)
TA31	K–Ar	whole rock	250	20	Tsao (1994)
TA32	K–Ar	whole rock	290	30	Tsao (1994)
A22	K–Ar	whole rock	370	40	Juang and Bellon (1984)
HKY03	fission track	zircon	770	100	Wang and Chen (1990)

Z2: This sequence consists of one K–Ar whole rock age, one K–Ar hornblende age, three Ar–Ar whole rock ages, and one fission track zircon age, all from very different

doi:10.6342/NTU202503882

locations and have zero overlap between different methods, making it difficult to come to any conclusions with the data at hand. This is one of the few areas in which a fission track age is not the oldest when fission track analyses have been done and is, in fact, the youngest.

Table 29: Z2 age data compilation listed by age from youngest to oldest.

Sample	**Method**	**Material**	**Age (ka)**	**± (1σ)**	**Source**
CS103	fission track	zircon	710	80	Wang and Chen (1990)
46	Ar–Ar (total gas)	whole rock	820	10	Lee (1996)
52	Ar–Ar (total gas)	whole rock	1360	70	Lee (1996)
A4	K–Ar	hornblende	2420	500	Juang and Bellon (1984)
A4	K–Ar	whole rock	2460	500	Juang and Bellon (1984)
30	Ar–Ar (plateau)	whole rock	1500	60	Lee (1996)

Z3: This sequence consists of four Ar–Ar groundmass ages, one K–Ar whole rock age, one U–Pb zircon age, and one fission track apatite age. Other than the borehole samples, all other samples are from very different locations. The HKY02 fission track apatite age is the oldest, and just below its age range is the TA25 K–Ar whole rock age. Both of which are much older than all the other results. All Ar–Ar groundmass ages lie within the <350 ka constraints of the HT-ML U–Pb zircon result between 280 to 340 ka. Thus, the age of this sequence likely lies within this range.

doi:10.6342/NTU202503882

Table 30: Z3 age data compilation listed by age from youngest to oldest.

Sample	Method	Material	Age (ka)	± (1σ)	Source
TTVG-BH01-134135	Ar–Ar (plateau)	groundmass	291	(-10/+30)	this study
TTVG-BH01-9697	Ar–Ar (plateau)	groundmass	305.9	4.2	this study
TTVG-BH01-7071	Ar–Ar (plateau)	groundmass	308.3	5.8	this study
TTVG-BH01-153154	Ar–Ar (plateau)	groundmass	328.2	4.4	this study
TA25	K–Ar	whole rock	560	40	Tsao (1994)
HKY02	fission track	apatite	700	90	Wang and Chen (1990)
HT-ML	U–Pb zircon	zircon	<350		Chu et al. (2018)

Z4 has no data.

Z5: This sequence consists of one Ar–Ar groundmass age, one Ar–Ar whole rock age, two K–Ar whole rock ages, and two fission track apatite ages. The sampling sites are a little spread out but are mostly from the bottom quadrant of the area. There's a huge overlap between the fission track apatite samples and the A11 K–Ar whole rock sample between 500 to 690 ka, although it is unclear what sort of event took place. At around 300 ka, a small amount of overlap between the 20120809-07 Ar–Ar groundmass age. This constrains the eruption of this sequence to within ~300 ka.

doi:10.6342/NTU202503882

Table 31: Z5 age data compilation listed by age from youngest to oldest.

Sample	Method	Material	Age (ka)	± (1σ)	Source
0970813-S03	Ar–Ar (plateau)	whole rock	90	140	Song et al. (2011)
20120809-07	Ar–Ar (plateau)	groundmass	280	20	Chang et al. (2024)
TA37	K–Ar	whole rock	320	20	Tsao (1994)
A11	K–Ar	whole rock	580	100	Juang and Bellon (1984)
HKY01	fission track	apatite	600	100	Wang and Chen (1990)
CS131	fission track	apatite	700	80	Wang and Chen (1990)

E. Suitable Dating Methods for Recent Eruption Ages at TVG

Across all subgroups and sequences, fission-track ages cluster at 400–800 ka, whereas other methods seldom exceed 400 ka (aside from some K–Ar/Ar–Ar whole-rock and hornblende ages). This contradicts the expectation that fission tracks record cooling (eruption) ages. Wang & Chen (1990) warned that incomplete annealing of zircons and apatites at eruption may overestimate fission-track ages. Moreover, those late-1990s analyses relied heavily on the analyst's vision and manual skill and may benefit from modern, automated methods.

Most U–Pb zircon analyses on TVG eruptions constrain ages to <350 ka; beyond that, ^{230}Th measurements become necessary. As an individual crystal analysis method, U–

doi:10.6342/NTU202503882

Pb zircon dating is a very promising dating method for its ability to discern the age of each singular crystal. The main issues are the limitations of the U–Pb system and the unreliability zircon saturation occurring in basaltic to andesitic lavas. Unfortunately, all Ar–Ar groundmass ages fall within <0.35 Ma and are beyond the limits of accurate U–Pb analysis. In conclusion, U–Pb zircon dating alone, while great for dating thermal events in which zircon saturation takes place, is unable to obtain recent eruption ages in the TVG volcanoes, and requires additional ^{230}Th analysis.

K–Ar and Ar–Ar whole-rock results span wide age ranges within each sequence and typically lie between amphibole and groundmass ages, reflecting mixed components (antecrysts, xenocrysts) in the rock. By contrast, Ar–Ar groundmass ages show greater internal consistency, agree between independent studies (e.g., Honlu flows in this study vs. Chang et al., 2024), and generally decrease up-hole and up-sequence. Groundmass ages rank among the youngest, second only to U–Th–Ra ages, but mixed phases can skew apparent ages upward by tens of thousands of years. In C1, groundmass results that contained more identifiable mixed components yielded apparent ages closer to the amphibole age, much like many of the whole rock ages, implying that many of these are also weighted mean averages of all mixed components present within the groundmass. Ultimately, Ar–Ar groundmass apparent ages in the TVG area likely overestimate true

doi:10.6342/NTU202503882

cooling or eruption ages. A few additional problems with the Ar–Ar dating in the TVG area were brought to light in this study. Low radiogenic argon content in young lavas pose a problem for a proper analysis as demonstrated in the number of failed analyses in younger samples. Despite this, Ar–Ar remains a practical tool to constrain eruptions to within a few $\times 10^4$ years, even in high-crystallinity TVG rocks.

The U–Th isochron results had a similar problem: most duplicates did not yield consistent results. Only groundmass–magnetite pairs yielded consistent isochrons. However, in comparison to all other methods, with most inconsistencies between duplicated limited to within a few thousand years they performed the best. Unexpectedly, groundmass–magnetite ages exceeded most mineral–mineral ages in Shamao 2 and 3 when groundmass is considered to be representative of erupted lava. This likely due to containing mixed components, much like what has been observed in the Ar–Ar results. In fact, the large discordance between the two visually, and isotopically, different amphibole phases in Shamao 2 and 3 is the greatest evidence that multiple components likely exist within the groundmass and mineral phases, even if they are not as easily differentiable by eye. For the same reasons as Ar–Ar analyses, the U–Th ages are likely older than the eruption age. Bulk analysis methods like Ar–Ar and U–Th internal isochron dating struggle to isolate a single eruption age when multiple crystal populations coexist, but

doi:10.6342/NTU202503882

these methods can contribute by constraining the eruption age to within a couple tens of thousands of years. For better constraints, analyzing for ^{226}Ra disequilibrium could help determine eruption ages that occurred within the Holocene. If not for its complex sample preparation process, the U–Th–Ra dating method, in theory, is ideal for dating TVG recent eruption ages due to its ability to constrain ages to within 10 ka.

Among available techniques, U–Th internal isochrons and Ar–Ar groundmass ages yield the youngest, most reproducible results in the TVG. Both methods analyze bulk separates and thus inherit uncertainties from mixed crystal populations in highly crystalline TVG lavas. These complexities explain age discrepancies among duplicates and prevent pinpointing exact eruption dates. Nonetheless, U–Th–Ra and Ar–Ar groundmass perform best at constraining recent eruptions.

F. Constraining TVG Recent Eruption Ages

TVG lavas carry antecrysts, xenocrysts, and mixed groundmass components, so no single “true” eruption age exists. Integrating new U–Th–Ra, Ar–Ar, and published data, we constrain the youngest eruptions in each subgroup using the age of the youngest sequence determined in a previous section (D) as follows:

Cising: within ≈25 ka (sequence C8)

Huangzuei: within ≈80 ka (sequence H4)

doi:10.6342/NTU202503882

Tatun: within ≈120 ka (sequence T4)

Chutze: within ≈300 ka (sequence Z5)

G. Multiphase Amphiboles

The most notable instance of multiphase in TVG can be observed in the amphiboles. Ar–Ar hornblende ages exceed co-existing groundmass ages, U–Th analyses distinguish two visually and isotopically distinct amphibole populations. These likely correspond to cognate inclusions formed during fractional crystallization at the reservoir base. Accurately dating each phase would reveal residence times, the interval between crystallization and eruption, and illuminate TVG magmatic processes. For example, in C5, the ≈430 ka gap between groundmass and hornblende Ar–Ar ages implies prolonged storage before eruption.

VIII. Conclusion

Several factors may explain age discrepancies in TVG: (i) contamination from older crystals during magma ascent, e.g., Miocene sandstone xenoliths that were incorporated into ascending magma can be found in TVG igneous rocks; (ii) crystals formed during earlier thermal events that remained in the reservoir and were later remobilized, e.g., TVG amphiboles often have opacite rims, which form during magma ascent, indicating that these amphiboles existed prior to eruption and may be antecrysts or xenocrysts; (iii) isotopic systems disturbed by subsequent processes, e.g., fumeroles can be found in TVG

doi:10.6342/NTU202503882

and can reopen isotopic systems.; and (iv) differences in methods and materials dating unrelated geological events, e.g., groundmass and mineral separates yield different U–Th and Ar–Ar ages. These potential sources of inconsistency must be considered when selecting geochronological techniques.

This study demonstrates that careful sample selection is essential for obtaining meaningful radiometric ages from TVG rocks, since TVG rocks are composed of mixed components. Antecrysts, xenocrysts, and xenoliths bias bulk-analysis ages toward weighted-mean values, a problem most evident in whole-rock dates that fall between groundmass and amphibole ages. Groundmass and mineral-separate analyses also suffer from issues with mixed components, yielding poor reproducibility for both U–Th internal isochrons and Ar–Ar groundmass methods.

Amphiboles provide the clearest example of multiphase complexity: two visually and geochemically distinct amphibole populations produced widely divergent U–Th ages. The older amphiboles may be linked to the amphibole-rich nodules discovered in previous studies. These are said to be basal cumulates that formed during fractional crystallization of basaltic magma in the magma reservoir, and the residence time of these crystals could contribute to the construction of the timeline of reservoir processes if paired with other chronometry methods, such as diffusion modelling. This would require reliable dates for both eruption age, by means of groundmass, and crystallization age, by means of mineral

doi:10.6342/NTU202503882

crystals, of which none have been produced thus far.

Despite these challenges, U–Th internal isochron and Ar–Ar groundmass analyses outperform other techniques in consistency and in constraining eruption ages within ±20 ka. For future work on recent TVG eruptions, researchers should consider:

1. Ra–Th dating alongside U–Th to resolve Holocene events
2. Modern fission-track methods to revisit overestimated Pleistocene ages
3. U–Pb zircon analysis for individual crystals younger than ~350 ka, with ^{230}Th corrections

Though it should be noted that any bulk-analysis age in the TVG area likely overestimates the true eruption date.

doi:10.6342/NTU202503882

IX. References

1. English References

Anderson, S. W., Stofan, E. R., Plaut, J. J., & Crown, D. A. (1998). Block size distributions on silicic lava flow surfaces: Implications for emplacement conditions. *GSA Bulletin*, *110*(10), 1258–1267. https://doi.org/10.1130/0016-7606(1998)110<1258:BSDOSL>2.3.CO;2

Bea, F., Bortnikov, N., Cambeses, A., Chakraborty, S., Molina, J. F., Montero, P., Morales, I., Silantiev, S., & Zinger, T. (2022). Zircon crystallization in low-Zr mafic magmas: Possible or impossible? *Chemical Geology*, *602*, 120898. https://doi.org/10.1016/J.CHEMGEO.2022.120898

Belluso, E., Ruffini, R., Schaller, M., & Villa, I. M. (2000). Electron-microscope and Ar isotope characterization of chemically heterogeneous amphiboles from the Palala Shear Zone, Limpopo Belt, South Africa. *European Journal of Mineralogy*, *12*(1), 45–62. https://doi.org/10.1127/0935-1221/2000/0012-0045

Belousov, A., Belousova, M., Chen, C. H., & Zellmer, G. F. (2010). Deposits, character and timing of recent eruptions and gravitational collapses in Tatun Volcanic Group, Northern Taiwan: Hazard-related issues. *Journal of Volcanology and Geothermal Research*, *191*(3–4), 205–221. https://doi.org/10.1016/j.jvolgeores.2010.02.001

Blundy, J., & Wood, B. (2003). Mineral-Melt Partitioning of Uranium, Thorium and

doi:10.6342/NTU202503882

Their Daughters. *Reviews in Mineralogy and Geochemistry*, *52*(1), 59–123. https://doi.org/10.2113/0520059

Boehnke, P., Watson, E. B., Trail, D., Harrison, T. M., & Schmitt, A. K. (2013). Zircon saturation re-revisited. *Chemical Geology*, *351*, 324–334. https://doi.org/10.1016/J.CHEMGEO.2013.05.028

Borisov, A., & Aranovich, L. (2019). Zircon solubility in silicate melts: New experiments and probability of zircon crystallization in deeply evolved basic melts. *Chemical Geology*, *510*, 103–112. https://doi.org/10.1016/J.CHEMGEO.2019.02.019

Boven, A., Pasteels, P., Kelley, S. P., Punzalan, L., Bingen, B., & Demaiffe, D. (2001). 40Ar/39Ar study of plagioclases from the Rogaland anorthosite complex (SW Norway); an attempt to understand argon ages in plutonic plagioclase. *Chemical Geology*, *176*(1), 105–135. https://doi.org/https://doi.org/10.1016/S0009-2541(00)00372-7

Buddington, A. F., & Lindsley, D. H. (1964). Iron-Titanium Oxide Minerals and Synthetic Equivalents. *Journal of Petrology*, *5*(2), 310–357. https://doi.org/10.1093/petrology/5.2.310

Chang, S. C., Zhang, H., Hemming, S. R., Mesko, G. T., & Fang, Y. (2012). Chronological evidence for extension of the Jehol Biota into Southern China.

doi:10.6342/NTU202503882

Palaeogeography, Palaeoclimatology, Palaeoecology, 344, 1-5. https://doi.org/10.1016/j.palaeo.2012.05.014

Chang, S. C., Hemming, S. R., Gao, K. Q., & Zhou, C. F. (2014). 40Ar/39Ar age constraints on Cretaceous fossil-bearing formations near the China–North Korea border. *Palaeogeography, Palaeoclimatology, Palaeoecology, 396*, 93-98. https://doi.org/10.1016/j.palaeo.2014.01.004

Chang, S.-C., Chu, M.-F., Wang, J.-P., Lai, Y.-M., Song, S.-R., Hemming, S. R., Ng, S. W.-P., & Chow, T. D. (2024). Volcanic activity around Taipei, Taiwan: new data and perspectives on the Tatun Volcano Group. *Geoscience Letters*, *11*(1), 42. https://doi.org/10.1186/s40562-024-00358-2

Chen, C. H. (1975). Petrological and chemical study of volcanic rocks from Tatun Volcano Group. *Proceedings of the Geological Society of China*, *18*, 59–72. https://cir.nii.ac.jp/crid/1573105974317344512

Chen, C. H. (1978). Significance of ultrabasic inclusions in Tatun Volcano Group, northern Taiwan. *Proceedings of the Geological Society of China*, *21*, 80–91.

Chen, C. H., & Wu, Y. J. (1971). Volcanic geology of the Tatun geothermal area, northern Taiwan. *Proceedings of the Geological Society of China*, *14*, 5–20.

Chu, C. J., Lee, C. T., & Teng, L. S. (1998). Structural features and Quaternary tectonics of Chinshan fault, northern Taiwan. *Journal of the Geological Society of China*, *41*,

doi:10.6342/NTU202503882

25–42.

Chu, M. F., Lai, Y. M., Li, Q., Chen, W. S., Song, S. R., Lee, H. Y., & Lin, T. H. (2018). Magmatic pulses of the Tatun Volcano Group, northern Taiwan, revisited: Constraints from zircon U-Pb ages and Hf isotopes. *Journal of Asian Earth Sciences*, *167*, 209–217. https://doi.org/10.1016/j.jseaes.2018.05.028

Chung, S.-L., Frank Yang, T., Lee, C., & Chen, C.-H. (1995). The igneous provinciality in Taiwan: Consequence of continental rifting superimposed by Luzon and Ryukyu subduction systems. *Journal of Southeast Asian Earth Sciences*, *11*(2), 73–80. https://doi.org/https://doi.org/10.1016/0743-9547(94)00040-L

Chung, S.-L., Wang, K.-L., Crawford, A. J., Kamenetsky, V. S., Chen, C.-H., Lan, C.-Y., & Chen, C.-H. (2001). High-Mg potassic rocks from Taiwan: implications for the genesis of orogenic potassic lavas. *Lithos*, *59*(4), 153–170.

Costa, F. (2008). Chapter 1 Residence Times of Silicic Magmas Associated with Calderas. *Developments in Volcanology*, *10*, 1–55. https://doi.org/https://doi.org/10.1016/S1871-644X(07)00001-0

Dickinson, J. E., & Hess, P. C. (1982). Zircon saturation in lunar basalts and granites. *Earth and Planetary Science Letters*, *57*(2), 336–344. https://doi.org/10.1016/0012-821X(82)90154-6

Dodson, M. H. (1973). Closure temperature in cooling geochronological and

doi:10.6342/NTU202503882

petrological systems. *Contributions to Mineralogy and Petrology*, *40*(3), 259–274. https://doi.org/10.1007/BF00373790

Esser, R. P., McIntosh, W. C., Heizler, M. T., & Kyle, P. R. (1997). Excess argon in melt inclusions in zero-age anorthoclase feldspar from Mt. Erebus, Antarctica, as revealed by the 40Ar39Ar method. *Geochimica et Cosmochimica Acta*, *61*(18), 3789–3801. https://doi.org/https://doi.org/10.1016/S0016-7037(97)00287-1

Fleck, R. J., Sutter, J. F., & Elliot, D. H. (1977). Interpretation of discordant 40Ar/39Ar age-spectra of mesozoic tholeiites from antarctica. *Geochimica et Cosmochimica Acta*, *41*(1), 15–32. https://doi.org/https://doi.org/10.1016/0016-7037(77)90184-3

Gervasoni, F., Klemme, S., Rocha-Júnior, E. R. V, & Berndt, J. (2016). Zircon saturation in silicate melts: a new and improved model for aluminous and alkaline melts. *Contributions to Mineralogy and Petrology*, *171*(3), 1–12. https://doi.org/10.1007/s00410-016-1227-y

Haack, U. (1977). The closing temperature for fission track retention in minerals. *American Journal of Science*, *277*(4), 459–464. https://doi.org/10.2475/ajs.277.4.459

Harrison, T. M., Duncan, I., & McDougall, I. (1985). Diffusion of 40Ar in biotite: Temperature, pressure and compositional effects. *Geochimica et Cosmochimica Acta*, *49*(11), 2461–2468. https://doi.org/https://doi.org/10.1016/0016-

doi:10.6342/NTU202503882

7037(85)90246-7

Hong, G. T., Benet, D., Wang, K. L., Costa, F., & Wang, L. C. (2025). Decrypting the sediment record of very late stage volcanic activities in Tatun volcano group, Northern Taiwan: evidence from ashy deposits. *Terrestrial, Atmospheric and Oceanic Sciences, 36(1),* 20.

Huang, C. K. (1954). Basaltic hornblende from Tatun Volcanoes, Taiwan. *Acta Geol. Taiwanica*, *6*, 1–12.

Juang, W. S. (1993). Diversity and origin of Quaternary basaltic magma series in northern Taiwan. *Bulletin of the National Museum of Natural Science*, *4*, 125–166.

Juang, W. S., & Bellon, H. (1984). The potassium–argon dating of andesites from Taiwan. *Proceedings of the Geological Society of China*, *27*, 86–100.

Kelley, S. (2002). Excess argon in K–Ar and Ar–Ar geochronology. *Chemical Geology*, *188*(1), 1–22. https://doi.org/https://doi.org/10.1016/S0009-2541(02)00064-5

Lee, J.-Y., Marti, K., Severinghaus, J. P., Kawamura, K., Yoo, H.-S., Lee, J. B., & Kim, J. S. (2006). A redetermination of the isotopic abundances of atmospheric Ar. *Geochimica et Cosmochimica Acta*, *70*(17), 4507–4512. https://doi.org/https://doi.org/10.1016/j.gca.2006.06.1563

Liu, J.-K., Shih, T.-Y., Chan, Y.-C., & Hsieh, Y.-C. (2007). Lidar DEM for characterizing the volcanic landforms of Tatun volcanoes in metropolitan Taipei.

doi:10.6342/NTU202503882

2007 IEEE International Geoscience and Remote Sensing Symposium, 3752–3755.

McLean, N. M., Bowring, J. F., & Bowring, S. A. (2011). An algorithm for U-Pb isotope dilution data reduction and uncertainty propagation. *Geochemistry, Geophysics, Geosystems*, *12*(6). https://doi.org/https://doi.org/10.1029/2010GC003478

Reiners, P. W., Carlson, R. W., Renne, P. R., Cooper, K. M., Granger, D. E., McLean, N. M., & Schoene, B. (2017). *Geochronology and Thermochronology*. John Wiley & Sons.

Rubin, K. H., van der Zander, I., Smith, M. C., & Bergmanis, E. C. (2005). Minimum speed limit for ocean ridge magmatism from 210Pb–226Ra–230Th disequilibria. *Nature*, *437*(7058), 534–538. https://doi.org/10.1038/nature03993

Rubin, K. H., & Zellmer, G. F. (2009). Reply to Comment on "On the recent bimodal magmatic processes and their rates in the Torfajökull–Veidivötn area, Iceland" by K.M. Cooper. *Earth and Planetary Science Letters*, *281*(1), 115–123. https://doi.org/https://doi.org/10.1016/j.epsl.2009.02.008

Shao, T., Xia, Y., Ding, X., Cai, Y., & Song, M. (2019). Zircon saturation in terrestrial basaltic melts and its geological implications. *Solid Earth Sciences*, *4*(1), 27–42. https://doi.org/10.1016/J.SESCI.2018.08.001

Sharma, Y. P., Lal, N., Bal, K. D., Parshad, R., & Nagpaul, K. K. (1980). Closing temperatures of different fission track clocks. *Contributions to Mineralogy and*

doi:10.6342/NTU202503882

Petrology, *72*, 335–336.

Song, S.-R., Chen, T.-M., Tsao, S., Chen, H.-F., & Liu, H.-C. (2007). Lahars in and around the Taipei basin: Implications for the activity of the Shanchiao fault. *Journal of Asian Earth Sciences*, *31*(3), 277–286. https://doi.org/https://doi.org/10.1016/j.jseaes.2006.07.017

Song, S.-R., Tsao, S., & Lo, H.-J. (2000b). Characteristics of the Tatun volcanic eruptions, North Taiwan: Implications for a cauldron formation and volcanic evolution. *Journal of the Geological Society of China*, *43*(2), 361–378.

Song, S.-R., Yang, T. F., Yeh, Y.-H., Tsao, S.-J., & Lo, H.-J. (2000a). The Tatun volcano group is active or extinct? *Journal of the Geological Society of China*, *43*(3), 521–534.

Szakács, A. (1994). Redefining active volcanoes: a discussion. *Bulletin of volcanology, 56(5)*, 321-325.

Teng, L. S. (1996). Extensional collapse of the northern Taiwan mountain belt. *Geology*, *24*(10), 949–952. https://doi.org/10.1130/0091-7613(1996)024<0949:ECOTNT>2.3.CO;2

Turner, S., George, R., Jerram, D. A., Carpenter, N., & Hawkesworth, C. (2003). Case studies of plagioclase growth and residence times in island arc lavas from Tonga and the Lesser Antilles, and a model to reconcile discordant age information. *Earth*

doi:10.6342/NTU202503882

and Planetary Science Letters, *214*(1), 279–294. https://doi.org/https://doi.org/10.1016/S0012-821X(03)00376-5

Vermeesch, P. (2018). IsoplotR: A free and open toolbox for geochronology. *Geoscience Frontiers*, *9*(5), 1479–1493. https://doi.org/https://doi.org/10.1016/j.gsf.2018.04.001

Wagner, G. A. (1972). Fission track length reductions in minerals and the thermal history of rocks. *Trans. Am. Nucl. Soc.*, *15*, 127–128.

Wagner, G. A. (1979). Correction and interpretation of fission track ages. *Lectures in Isotope Geology*, 170–177.

Wang, K. L., Chung, S. L., Chen, C. H., Shinjo, R., Yang, T. F., & Chen, C. H. (1999). Post-collisional magmatism around northern Taiwan and its relation with opening of the Okinawa Trough. *Tectonophysics*, *308*(3), 363–376. https://doi.org/10.1016/S0040-1951(99)00111-0

Wang, K. L., Chung, S. L., O'Reilly, S. Y., Sun, S. S., Shinjo, R., & Chen, C. H. (2004). Geochemical constraints for the Genesis of post-collisional magmatism and the geodynamic evolution of the northern Taiwan region. *Journal of Petrology*, *45*(5), 975–1011. https://doi.org/10.1093/petrology/egh001

Wang, W. H., & Chen, C. H. (1990). The volcanology and fission track age dating of pyroclastic deposits in Tatun Volcano Group. *Acta Geoligica Taiwanica*, *28*, 1–30.

doi:10.6342/NTU202503882

Watson, E. B., & Harrison, T. M. (1983). Zircon saturation revisited' temperature and composition effects in a variety of crustal magma types. *Earth and Planetary Science Letters*, *64*, 295–304. https://doi.org/10.1016/0012-821X(83)90211-X

Yang, C. C., Liu, J. K., Huank, M. T., & Chen, W. S. (2004). DTM for mapping the volcanic landforms of Tatun Volcano Group in Northern Taiwan. *Journal of Photogrammetry and Remote Sensing*, *9*(2), 1–8.

Yang, T. F., Sano, Y., & Song, S. R. (1999). $^{3}He/^{4}He$ ratios of fumaroles and bubbling gases of hot springs in Tatun Volcano Group, North Taiwan. *Nuovo Cimento Della Societa Italiana Di Fisica C*, *22*(3–4), 281–286.

Zellmer, G. F., Rubin, K. H., Miller, C. A., Shellnutt, J. G., Belousov, A., & Belousova, M. (2015). Resolving discordant U-Th-Ra ages: Constraints on petrogenetic processes of recent effusive eruptions at Tatun Volcano Group, northern Taiwan. In *Geological Society Special Publication, 422*(1), 175–188. https://doi.org/10.1144/SP422.3

2. Chinese References

王執明、鄭穎敏、王源（1978）。臺北盆地之地質及沉積物研究，臺灣礦業，第30期，第4卷，第350-380頁。

宋聖榮、楊燦堯、徐春田、蔡裕偉（2011）。大台北地區特殊地質災害調查與監測(二)-火山地質和地球化學調查與監測-四年總結報告。經濟部中央地質調查所。

doi:10.6342/NTU202503882

宋聖榮、楊燦堯、徐春田、蔡裕偉（2012）。火山地質與火山活動調查與監測，大台北地區特殊地質災害調查與監測第二期，計畫編號100-5226904000-01-01。經濟部中央地質調查所委託報告。

李淑芬（1996）。大屯火山群七星火山亞群熔岩層序之研究。國立臺灣大學地質學研究所碩士論文，共136頁。

曹恕中（1994）。大屯火山群火山岩的鉀氬年代分析。經濟部中央地質調查所彙刊，第九號，第137-154頁。

莊文星、陳汝勤（1989）。臺灣北部火山岩之定年與地球化學研究。經濟部中央地質調查所彙刊，第5號，第31-66頁。

陳正宏（1990）。台灣地質之一，台灣之火成岩。經濟部中央地質調查所，共137頁。

黃鑑水（1988）。五萬分之一台灣地質圖及說明書-台北圖幅。經濟部中央地質調查所，共46頁。

doi:10.6342/NTU202503882